Maxim Honea, BSc

# Feasibility of manufacturing biodegradable metal-polymer hybrid components by applying the add joining process

**MASTER'S THESIS**

to achieve the university degree of

Diplom-Ingenieur

Individual master's degree programme:

Advanced Materials Science and Management

submitted to

**Graz University of Technology**

**Supervisor**

Univ.-Prof. Dipl.-Ing. Dr.techn. Christof Sommitsch

**Co-Supervisor**

Dr.techn. Fernando Gustavo Warchomicka

Institute of Materials Science, Joining and Forming

Graz, February 2021

# AFFIDAVIT

I declare that I have authored this thesis independently, that I have not used other than the declared sources/resources, and that I have explicitly indicated all material which has been quoted either literally or by content from the sources used. The text document uploaded to TUGRAZonline is identical to the present master's thesis.

---

Date, Signature

# Acknowledgment

# Abstract

Some groundbreaking progress with different sorts of biocompatible materials (e.g. metals, polymers, ceramics) for medical applications (e.g. dental technology, prosthetics) made the therapy easier, fostered the healing process, and, more importantly, increased the quality of living for the patients drastically. Besides corrosion-resistant materials for permanent and temporary implants (e.g. stainless steel or Ti-alloy screws, PA-sutures), the interest in bioresorbable materials, which constrain the post-surgery interventions of temporary implants, is increasing in the last decades. Today, there are several bioresorbable substitute products (e.g. Mg-alloy screws, PGA-, or PCL-sutures) available on the clinical market.

This project aimed to establish an add joining procedure to manufacture metal-polymer hybrid components. The idea was to exploit a metal's and a polymer's specific properties by forming a hybrid structure. Thereby, the polymer temporarily prevents the metal from degrading in an early phase to maintain its mechanical integrity for a specific time.

The experiments were conducted with a magnesium alloy and polylactic acid (PLA). The Mg-alloy's surface was thermally processed on an electron beam welding (EBW) machine to generate a groove-shaped topography, which should increase the bond surface adhesion. Three different groove heights were generated and characterized. The add joining was performed with PLA on the surface-modified Mg-samples by applying the fused deposition modeling (FDM) process. Single lap shear investigations of the metal-polymer hybrids indicated that the ultimate lap shear stress (ULSS) increases with increasing topography heights and showed a maximum of $12.0 \pm 1.1$ MPa. The 3-point bending tests indicated that the polymer significantly increases the resistance to flexural stress. Further, an immersion corrosion test setup with $CO_2$–buffering was developed to measure the hydrogen evolution over time. The experiments were carried out in Hanks' Balanced Salt solution (HBSS) for one week with different material states (as-cast, surface-modified, and hybrid samples).

Add joining of metal-polymer hybrids might be beneficial in the development of biomedical applications. The results showed that FDM is a suitable technique to manufacture such hybrids. The corrosion experiments require more detailed investigations to make a clear statement on the hybrids' applicability.

# Kurzfassung

Bahnbrechende Fortschritte im medizinischen Bereich (z.B. Zahntechnik, Prothetik) mit verschiedensten biokompatiblen Werkstoffen (z.B. Metalle, Polymere, Keramiken) erleichterten in den letzten Jahrzehnten zahlreiche Behandlungen, förderten die Heilungsprozesse und erhöhten die Lebensqualität der PatientInnen signifikant. Neben korrosionsbeständigen Materialien für permanente und temporäre Implantate (z.B. Edelstahl- oder Ti-Legierung-Schrauben, PA-Nahtmaterial), hat das Interesse an bioresorbierbaren Materialien, welche die Notwendigkeit postoperativer Eingriffe reduzieren, zugenommen. Heutzutage sind bereits etliche bioresorbierbare Ersatzprodukte (z.B. Schrauben aus Mg-Legierungen, PGA- oder PCL-Nahtmaterial) auf dem medizinischen Markt erhältlich.

Ziel dieses Projektes war es, eine auf additiven Fertigungsverfahren (AM) basierende Fügetechnik zur Herstellung von Metall-Polymer-Hybriden zu etablieren. Diese Hybride sollen die spezifischen Eigenschaften von Metall und Polymer vereinen. Das Polymer verhinder unter anderem temporär, dass das Metall abgebaut wird und dadurch seine Festigkeit zu früh verliert.

Die Versuche wurden mit einer Mg-Legierung und Polymilchsäure (PLA) durchgeführt. Die Oberfläche der Mg-Legierung wurde mit einem Elektronenstrahlschweißgerät (EBW) thermisch behandelt. Die dadurch entstandene Rillenstruktur erhöht die Haftung des Polymers. Es wurden Proben mit verschiedenen Rillenhöhen angefertigt und charakterisiert. Mittels Schmelzschichtung (FDM) wurde das PLA mit den oberflächenmodifizierten Mg-Proben verbunden. Zugscherversuche dieser Metall-Polymer-Hybride verdeutlichten, dass die Zugscherfestigkeit (ULSS) mit zunehmender Rillenhöhe ansteigt und ein Maximum von $12.0 \pm 1.1$ MPa erreicht. Die 3-Punkt-Biegeversuche zeigten, dass das Polymer die Biegesteifigkeit signifikant erhöht. Des Weiteren wurde ein Korrosionsversuchsstand mit $CO_2$-Pufferung entwickelt, um die Wasserstoffbildung über die Zeit zu messen. Dafür wurden verschiedene Materialvarianten – nämlich Mg-Gusslegierung (unbehandelt und oberflächenmodifiziert) und Hybride – über eine Dauer von sieben Tagen einer Salzlösung nach Hanks (HBSS) ausgesetzt.

Metall-Polymer-Hybride könnten einen wertvollen Beitrag in der Entwicklung biomedizinischer Produkte leisten. Die Versuche veranschaulichen die Eignung des Schmelzschichtungsverfahrens zur Herstellung solcher Hybride. Weitere Korrosionsversuche sind jedoch erforderlich, um eine fundiertere Aussage über die medizinische Anwendbarkeit dieser treffen zu können.

# Abbreviations

| | |
|---|---|
| ABS | acrylonitrile butadiene styrene |
| AM | additive manufacturing |
| CAD | computer-aided design |
| CNC | computer numerical control |
| $CO_2$ | carbon dioxide |
| DiMi | digital microscopy |
| DIY | do-it-yourself |
| DOE | design of experiments |
| EB | electron beam |
| EBP | electron beam process |
| EBW | electron beam welding |
| FDM | fused deposition modeling |
| FESEM | field-emission scanning electron microscopy |
| $H_2$ | hydrogen gas |
| HAZ | heat-affected zone |
| HBSS | Hanks' Balanced Salt solution |
| IMP | intermetallic phase |
| LOM | light optical microscopy |
| Mg L2+ | magnesium alloy |
| $OH^-$ | hydroxide |
| PA | polyamide |
| PCL | polycaprolacton-co-lactid |
| PGA | polyglycolic acid |
| PLA | polylactic acid |
| PLLA | poly-L-lactide |
| PDLA | poly-D-lactide |
| PDLLA | poly-DL-lactide |
| PLGA | poly lactic-co-glycolic acid |
| PP | polypropylene |
| ULSS | ultimate lap shear strength |
| UTS | ultimate tensile strength |
| SBF | simulated body fluid |
| SEM | scanning electron microscopy |
| SiC | silicon carbide |
| SLM | selective laser melting |
| YS | yield strength |

# Content

# 1. Introduction

Bioresorbable materials for medical applications are auspicious for clinical purposes. Some resorbable products are already used in surgeries. During this project, the feasibility of add joined metal-polymer hybrids and their suitability for medical applications was tested. Thereto, an AM procedure based on the FDM process was developed to create metal-polymer hybrid joints. The Mg-alloy's interface surface was heat-treated and the topography was changed at a macroscopic scale. The hybrid components were characterized mechanically by single lap shear and 3-point bending tests. The materials and hybrids were immersed for one week in Hanks' Balanced Salt solution (HBSS) to observe the corrosion behavior under physiological conditions.

The following section will cover the state of the art of materials for biomedical applications and two specific types of materials in more detail. Subsequently, composites and hybrid structures, in general, will be outlined. Then FDM and the EBW process will be discussed. Finally, some fundamental corrosion mechanisms in metals and polymers will be elaborated, followed by a review of the drivers for this project's initiation.

The experimental part will deal with the used materials, their sample preparation, and their characterization. Then the procedure, structuring patterns, and parameters of the electron beam process (EBP) will be illustrated. Next, a description of the polymer printing procedure, parameter tests, the polymer's intrusion behavior, and the actual add joining for the mechanical tests follows. Lastly, the in vitro corrosion experiments and the different test conditions are shown.

The result section will discuss the examination of the materials. Subsequently, the topographies from the surface structuring process and some observations will be elaborated. The results from the printing parameter tests and the polymer's intrusion behavior into the grooves will be elucidated. Afterward, the quantitative discussion of the mechanical tests and corresponding fracture surfaces will be in focus. Then the findings from the corrosion experiments will be illustrated.

The last two sections will summarize the most relevant results and give an outlook on the promising future measures to go further on this topic.

# 2. State of the art

For hundreds of years, various materials were used to treat different kinds of injuries. Archaeological excavations at Mayen dig sites found dental implants made from seashells, dating back to 600 AD. In Europe (France), a dental implant manufactured from iron in 200 AD was found. Both of them exhibited proper integration into the bone tissue (osseointegration). The use of sutures to treat wounds dates back even further. There is proof that the early Egyptians used sutures out of linen, while in Europe, catguts were used during the middle ages. Plenty of other well-intended attempts with different materials are documented. However, due to the lack of knowledge in biocompatibility and proper sterilization, it took until the second half of the twentieth century before the chances of a prosperous treatment increased significantly. Until today various clinical products – such as dental implants, hip and knee prosthesis, stents, bone fixation plates, heart valves, pacemakers – are developed. [1]

A fundamental requirement for biomedical devices is that the used materials – e.g. metals, polymers, ceramics, glasses, and composites of them – have to be biocompatible. One definition of biocompatibility concludes that materials should not show toxic or harming effects when it gets in contact with biological organisms [2]. A more holistic definition describes biocompatibility as the "*ability of a material to perform with an appropriate host response in a specific application*" [3]. Hence, *appropriate host response* is the "*resistance to blood clotting, resistance to bacterial colonization, and normal, uncomplicated healing*" [4]. For a lot of them, the surgical procedure and the influence of the implants in the human body are studied quite well. Depending on the implant type, a biomaterial must fulfill specific mechanical – such as modulus of elasticity, tensile strength, ductility, hardness – and surface properties – like surface roughness and surface tension or energy. The surface properties mainly determine the adhesion of tissues (e.g. bone tissue), proteins, and cells, which is vital for the healing process. [5]

In many cases, corrosion-resistant biomaterials (metals, polymer, ceramics) are used for permanent and temporary implants. For some applications, such as the treatment of fractured bones, it can be beneficial to use implants made out of materials that degrade and resorb within the human body over time. By this approach, post-surgery interventions of temporary implants – such as the implant's extraction after completing the healing process – can be constrained. Consequently, the livability of patients increases.

Figure 1 exemplifies the ideal degradation behavior for a magnesium implant in a bone fracture treatment. It is advantageous for the healing process if an implant maintains its mechanical properties in the first few weeks after implantation. A postponed degradation of the implant can help to achieve this, and hence, the bone tissue can attain its mechanical strength and carry the loads by itself again. [6]
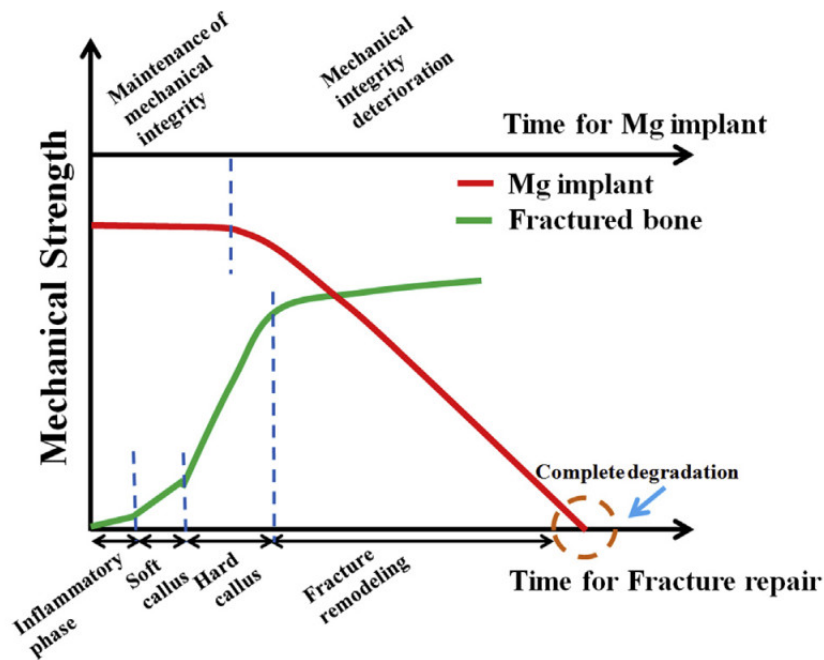


*Figure 1: Ideal degradation behavior of a magnesium implant during the healing process [6]*

## 2.1. Bioresorbable materials

Due to the potential use in medicine, bioresorbable materials – a subfield of biocompatible materials – are a much-discussed topic for temporary implants. Several terms such as *biodegradation*, *bioabsorption*, or *bioerosion* are used in the context of the dissolution of biocompatible and bioresorbable materials. Even though these terms describe different mechanisms, they are often used as synonyms in literature. *Biodegradation* refers to the chemical process of the disintegration of materials in physiological environments. *Bioresorption* or *bioabsorption* refers to removing degradation products "*by cellular activity (e.g. phagocytosis) in a biological environment*". Whereas *bioerosion* describes a change in physical properties (size, shape, or mass) during degradation processes. [7]

## 2.1.1. Bioresorbable metals

In the field of bioresorbable materials, metals are of particular interest since some of them display excellent mechanical properties and favorable corrosion behaviors. Various alloying systems (e.g. Mg-, Zn-, Fe-based) were investigated to this day, and a couple of them proved to be suitable for biomedical purposes [8]. Elements that are considered to be essential nutrients of the human body are particularly worthwhile. In Table 1, Zheng et al. summed up the pathophysiology and toxicology of commonly used alloying elements [9]. Some of them are indispensable for human metabolism.

*Table 1: Summary of pathophysiology and toxicology of commonly used alloying elements [9]*

| Element | Human amount | Pathophysiology | Toxicology | Daily allowance |
|---|---|---|---|---|
| Essential nutrients | | | | |
| Mg | 25 g | "Activator of many enzymes; co-regulator of protein synthesis and muscle contraction; stabilizer of DNA and RNA" | "Excessive Mg leads to nausea" | 700 mg |
| Ca | 1100 g | "More than 99% has a structure function in the skeleton; the solution Ca has a signal function, including muscle contraction, blood clotting, cell function, etc." | "Inhibit the intestinal absorption of other essential minerals" | 800 mg |
| Zn | 2 g | "Trace element; appears in all enzyme classes; most Zn appears in muscle" | "Neurotoxic and hinder bone development at higher concentration" | 15 mg |
| Mn | 0.012 g | "Trace element; activator of enzyme; Mn deficiency is related to osteoporosis, diabetes mellitus, atherosclerosis" | "Excessive Mn results in neurotoxicity" | 4 mg |
| Fe | 4–5 g | "Component of several metalloproteins; be crucial in vital biochemical activities, i.e. oxygen sensing and transport" | "Iron toxicity gives rise to lesions in the gastrointestinal tract, shock and liver damage" | 10–20 mg |
| Other elements | | | | |
| Li | – | "Used in the treatment of manic depressive psychoses" | "Plasma concentration of 2 mM is associated with reduced kidney function and neurotoxicity, 4 mM maybe fatal" | 100 mg |
| Al | <0.3 g | – | "Primarily accumulated in bone and nervous system; implicated Al in the pathogenesis of Alzheimer's disease" | – |
| Zr | <0.25 g | "Probably excreted in feces; low systematic toxicity to animals" | "High concentration in liver and gall bladder" | 3.5 mg |
| Y & lanthanides | – | "Substituted for Ca2+ and matters when the metal ion at the active site; compound of drugs for treatment of cancer" | "Basic lanthanides deposited in liver; more acidic and smaller cations deposited in bone" | – |

Besides the physiological aspects, it is also essential that the materials exhibit specific mechanical properties and corrosion rates. In the following section, Mg-alloys, their alloying elements, and their contribution to these properties are briefly elucidated.

## Magnesium and its alloys

The discovery of magnesium in its elemental form goes back to 1755, in which Joseph Black examined magnesia. In 1808 it was first isolated by electrolysis. From there on, different approaches were applied to obtain magnesium in its pure form. Until the late 19th-century metallic

magnesium was only produced in Germany and was mostly used for flashlights and pyrotechnics. [10]

The first documented study on magnesium in a biomedical context in humans goes back to 1878 and utilized magnesium-wires to stop bleeding vessels. From 1892–1905 an Austrian surgeon, Dr. Erwin Payr (Graz, Austria), already worked with high-purity magnesium implants (e.g. tubes for vessels, plates, nails, wires) and conducted in vivo studies in animals and humans [11]. In the last decades, magnesium and its alloys drew much attention and are rated to be a promising material for biomedical purposes. In small quantities, magnesium – as well as zinc, iron, and calcium – are considered to be nontoxic since it is an essential element within the human body and a part of the general metabolism [9]. The modulus of elasticity of magnesium (41-45 GPa), compared to iron (~211.4 GPa) or zinc (~90GPa), is closer to bone tissue (3-20 GPa) and therefore considered to be a very potential material for the treatment of bone tissue injuries [12]. If the difference in elastic modulus is too high, stress shielding of the bone might occur, which results in degeneration of the bone tissue and thus a further weakening of the bone strength [13]. Contrary, the high degradation rate of pure magnesium is critical since it exceeds the bone growth rates and the evolved hydrogen gas ($H_2$) from degradation can not be resorbed fast enough [14]. This localized $H_2$ and corresponding hydroxide ($OH^-$) gatherings can hinder the healing process due to pH variations in those regions [15]. To counteract this downside, it was tried to develop magnesium-based alloys with different alloying elements, which should increase the corrosion resistance. In Table 2 some commercial alloys which were studied in clinical trials are illustrated.

*Table 2: Commercial bioresorbable Mg-alloys for biomedical applications [16]*

| Type | Main alloying elements |
|---|---|
| AZ31 | Al, Zn, Mn |
| AZ91 | Al, Zn, Mn |
| AM50 | Al, Mn, Zn |
| WE43 | Y, rare earths (Nd, Gd), Zr |
| LAE442 | Li, Al, rare earths |

Zinc (Zn) and manganese (Mn) are much used alloying elements and are considered to be uncritical alloying elements in low concentrations. Aluminum (Al) is used to tune the mechanical properties and decreases the corrosion rates [16]. Yet, it is still controversial what the long-term effects of the presence of Al within the human body might be [17] (also see Table 1). Short-term studies indicated that aluminum negatively influences osteoblasts' behavior and neurons [18, 19]. The addition of rare earths is also seen as critical [20]. Investigations on WE43 have shown Neodymium (Nd) and Yttrium (Y) remained around the implant for some time, which led to the conclusion that those elements are difficultly absorbed by the body [14]. Due to those uncertainties, much effort was put into the study of alloys with less critical elements. The addition

of other elements enables the adjustment of the corrosion rates and mechanical properties for specific demands.

## Mg-Zn-Yb-Ca-Zr system

In the following section, the effects of alloying elements of the alloy used in this thesis will be elaborated. Additionally, some quaternary Mg-alloys will be highlighted. A study of the specific Mg-Zn-Yb-Ca-Zr-alloy was not found in the literature.

### Zinc

Zinc is an essential element within human physiology [9, 21]. Because pure zinc has a much lower corrosion rate than pure magnesium, it is a beneficial alloying element [22–25].

In binary Mg-alloys, the addition of zinc has shown to be uncritical in the in vitro cytotoxicity tests and showed sufficient biomedical application properties. The ultimate tensile strength (UTS) and elongation of Mg-xZn-alloys (x = 1 to 6%) displayed a local peak at 4 wt.% zinc, while the yield strength (YS) continued to increase. The potentiometric polarization experiments revealed that at 1 wt.% zinc, the alloy exhibited the highest corrosion resistance from the tested compositions. [22]

Further, zinc has a positive influence when it comes to antibacterial properties [26]. He et al. conducted in vivo studies on rabbits with binary Mg-5.6Zn-alloy rods and did not find any evidence of impairment in the tissue or organs [27].

### Ytterbium

Ytterbium (Yb) is a heavy rare earth and is considered a grain refinement agent in Mg-alloys [28]. Studies have shown that the addition of Yb increases the corrosion resistance of Mg-Zn-alloys [29]. They attribute this to the finely distributed $Mg_2Yb$ intermetallic phases in the magnesium matrix. Further, Li et al. found that Ytterbium (1 and 2 wt. %) in a Mg-Zn-Zr-alloy increased the microhardness and UTS, though the elongation minorly decreased [30]. They also confirmed that such alloys exhibited significantly decreased corrosion rates.

### Calcium

Observations in Mg-Zn-Mn-alloys showed decreased grain sizes with increasing Ca-content (up to 0.5 wt.%) [31]. Also, there was evidence that the mechanical properties (UTS, elongation) at 0.5 wt.% exhibit a local maximum. Mg-1Ca-alloy pins were examined by Li et al. during in vivo studies with pleasing results regarding biocompatibility [32]. The study pointed out that the as-cast material's mechanical properties decreased with an increase of Ca-content (1, 2, and 3 wt.%). An investigation by Zhang et al. have indicated that for different Ca-contents in a ternary Mg-4Zn-xCa alloy (x= 0, 0.2, 0.5, 1, 1.5 & 2) addition of 0.2 wt.% of calcium led to a maximum in

UTS and elongation, while the YS increased until 2% wt.% [22]. The same experiments also pointed out that small quantities of calcium (0.2 wt.%) resulted in a local peak in corrosion resistance.

## Zirconium

Zirconium has a significant influence on grain refinement [9, 33]. Gu et al. compared different binary cast Mg-1x-alloys (x = Al, Ag, In, Mn, Si, Sn, Y, Zn, and Zr) and have shown that an addition of 1 wt.% zirconium – over the peritectic concentration of 0.5 wt.% – results in better mechanical properties (YS, UTS & elongation) and decreased corrosion rates (~50% less hydrogen evolution) compared to the pure magnesium as-cast material [23].

## Mg-Zn-Ca-Zr and Mg-Zn-Yb-Zr systems

The solubility of calcium in magnesium (Figure 2) is approximately 1.35 wt.% and for zinc 6.2 wt.% [12]. Wang et al. found that the homogenized as-cast Mg-3Zn-xCa-0.6Zr alloy (x = 0, 0.6, 1.2, 1.8) indicated ternary $Ca_2Mg_6Zn_3$ phase and that an increasing amount of calcium led to a grain refinement [34]. They also found binary MgZn precipitates, which result from "*the low melting point of MgZn*" and the inhibited diffusion rates of zinc within Mg-alloys compared to calcium.

In as-cast homogenized ZK60 (Mg-5.4Zn-0.6Zr), $MgZn_2$ and $Zn_2Zr$ were found to be present [35]. Thereby fine $Zn_2Zr$ particles were distributed through the microstructure. The addition of 0.8 wt.% Zr in extruded Mg-6Zn-0.2Ca-alloy exhibited improved UTS but lowered the elongation [36]. They attributed this to the finer crystal structure through the dynamic recrystallization of the extruded samples. Ding et al. demonstrated the Mg-Zn-Ca alloys' biocompatibility during in vitro and in vivo tests. Only little amounts of hydrogen gas and no inflammation of the surrounding tissue were observed [37].

Li et al. studied the microstructure evolution of a Mg-Zn-Yb-Zr-alloy during heat treatment and the corresponding microhardness [38]. Yu et al. have shown that Yb has a positive influence on the precipitation strengthening in Mg-Zn-Zr-alloy (ZK60) [39].
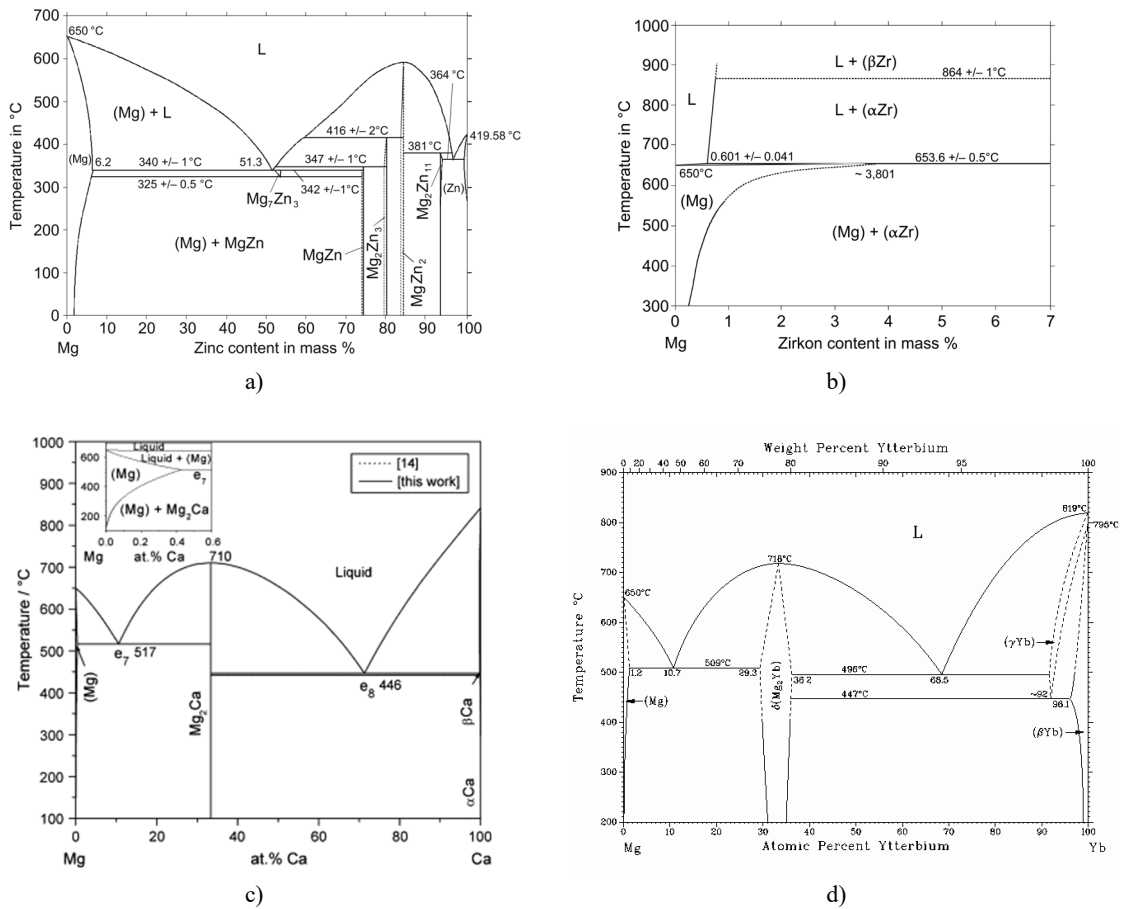
*Figure 2: Binary phase diagrams a) Mg-Zn phase diagram [10] b) Mg-Zr phase diagram [10]*
*c) Mg-Ca phase diagram [40] d) Mg-Yb phase diagram [41]*

In Table 3, the mechanical properties of different Mg-alloys and tissues are summed up and compared with some other commonly used biocompatible materials.

*Table 3: Comparison of different Mg-alloys and tissues with common biocompatible materials*

| Tissue/ material | Comp. strength [GPa] | Tensile strength [GPa] | E-mod. tensile [GPa] | Yield strength [GPa] | Elongation (A) at break [%] | Ref. |
|---|---|---|---|---|---|---|
| Cortical bone[*] | 164–240 | 35–283 | 5–23 | | 1.07–2.10 | |
| Cancellous bone[*] | | 1.5–38 | 0.01–1.57 | | | [15] |
| Arterial wall | | 0.50–1.72 | 0.001 | | | |
| | | | | | | |
| Cartilages | | 3.7-10.5 | 0.001-0.015 | | | |
| Ligament | | 13-46 | 0.07-0.54 | | | [42] |
| Tendon | | 24-112 | 0.14-2.3 | | | |
| | | | | | | |
| TiAl6V4, cast | | 830–1025 | 114 | 760–880 | 12 | |
| TiAl6V4, wrought | | 896–1172 | 114 | 827–1103 | 10–15 | |
| Stainless steel 316L | | 480–620 | 193 | 170–310 | 30–40 | |
| Synthetic HA | 100–900 | 40–200 | 70–120 | | | |
| Bioactive glass | | 40–60 | 35–35 | | | |
| PDLLA | | 29–35 | 1.9–2.4 | | 5–6 | [15] |
| | | | | | | |
| AZ91E-F sand cast | 97 | 165 | 45 | 97 | 2.5 | |
| AZ31 extr. | 83–97 | 241–260 | | 165–200 | 12–16 | |
| LAE442 | | 247 | | 148 | 18 | |
| WE43 extr. | | 277 | | 198 | 17 | |
| AM50A-F | 113 | 210 | | | 10 | |
| | | | | | | |
| Mg-4Zn cast | | 216.8 ± 15 | | 58 ± 1.0 | 15.8 ± 5.5 | |
| Mg-1Zn cast | | 101.5 ± 3 | | 20 ± 2 | 6.96 ± 0.5 | [22] |
| Mg-4Zn-0.2Ca cast | | 225 ± 5 | | 58.1 ± 1.0 | 17.5 ± 1.0 | |
| | | | | | | |
| Mg cast[**] | | ~85 | | ~20 | ~13 | |
| Mg-1Zr cast[**] | | ~170 | | ~65 | ~27 | [23] |
| Mg-1Zn cast[**] | | ~135 | | ~25 | ~18 | |
| | | | | | | |
| Mg-6.6Zn-0.2Ca extr. | 135 | 275 | | 148 | 26 | [36] |
| Mg-5.7Zn-0.2Ca-0.8Zr extr. | 261 | 357 | | 310 | 18 | |

[*] "The range of values are depending on species, age of species, anatomical location and testing conditions." [15]
[**] approximate values extracted from a bar chart

## 2.1.2. Bioresorbable polymers

There are already plenty of biocompatible but permanent polymers used for various biomedical applications (e.g. tissue scaffolds, implanted drug delivery systems, catheters, or dialysis tubing). Such polymers have the advantage that they are light, easy to process into the desired shape, and quite resistant to chemicals [43]. Naturally, for bioresorbable polymers, the chemical resistant is considered to be obstructive to some degree. Depending on its application, a bioresorbable polymer should degrade over a very short or long period. The "*molecular weight, crystallinity, and hydrophilicity*" determines the degradation time and the polymer's mechanical properties [44]. During resorption or degradation, two main events occur. Firstly the long polymer chains

start to segregate due to *hydrolysis* or *enzymic attack* and subsequently, those segregations are *"dissolved in extracellular fluids by phagocytosis or via metabolism"* [44].

Since the 1960s, bioresorbable PGA-sutures are used [1]. In some surgeries, resorbable PCL-sutures replaced conventional ones, which had to be extracted from the patient after a while [45, 46]. Further, bioresorbable stents out of poly (L-lactide) acid (PLLA) showed their potential in surgical studies [47] and are already approved for medical use in some countries. Table 4 lists some selected bioresorbable polyester, their properties, and degradation times:

Table 4: Selected bioresorbable polyester [48]

| Polymer | Melting point [°C] | Glass transition temp. [°C] | Modulus[*] [Gpa] | Elongation [%] | Degradation time[**] [months] |
|---|---|---|---|---|---|
| PGA | 225–230 | 35–40 | 7 | 15–20 | 6 to 12 |
| PLLA | 173–178 | 60–65 | 2.7 | 5–10 | >24 |
| PDLLA | Amorphous | 55–60 | 1.9 | 3–10 | 12 to 16 |
| PCL | 58–63 | -65 – -60 | 0.4 | 300–500 | >24 |
| PLGA (85/15) | Amorphous | 50–55 | 2 | 3–10 | 5 to 6 |
| PLGA (75/25) | Amorphous | 50–55 | 2 | 3–10 | 4 to 5 |
| PLGA (65/35) | Amorphous | 45–50 | 2 | 3–10 | 3 to 4 |
| PLGA (50/50) | Amorphous | 45–50 | 2 | 3–10 | 1 to 2 |

[*] "tensile or flexural modulus"
[**] "time to complete resorption"

Besides the above-listed polymers, natural polymers (e.g. gelatine, collagen, cellulose, etc.) are used for various biomedical applications. Furthermore, there are other synthetic degradable polymers under investigation for biomedical applications (e.g. *polyanhydrides*, *polycyanoacrylates*, *poly(amino acid)s*). [7]

## Polylactic acid

Polylactic acid (PLA) is categorized as an aliphatic polyester and is built up by lactic acid (LA) monomers (Figure 3a). The LA monomer is chiral and is present in L-(+)-lactic acid and D-(–)-lactic acid (Figure 3b). Via polymerization, pure poly-D-lactic acid (PDLA), pure poly-L-lactic acid (PLLA), or poly-DL-lactic acid (PDLLA) can be synthesized. Commercial PLA consists of a large part of L-lactic acid. LA can be synthesized either by fermentation (e.g. from milk) or petrochemically. During the dissolution of PLA, it splits up into the LA monomers again. Hydrolysis is the primary driver of degradation [49]. Those monomers are biocompatible and resorbed by the human body. [50]
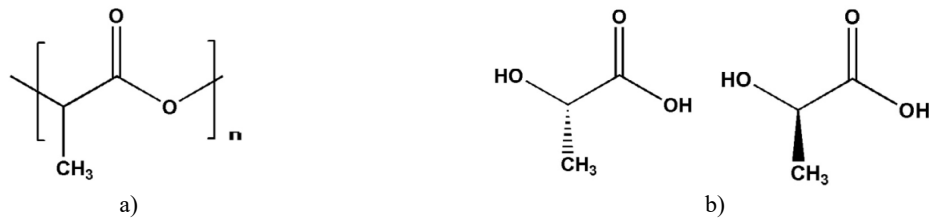
*Figure 3: a) Polylactic acid b) L-(+)-lactic acid and D-(–)-lactic acid monomer [51]*

PLA was already used in different medical applications such as sutures, drug release systems, scaffolds for tissue engineering, or braided prostheses [52]. One significant advantage of PLA is that exhibits very good mechanical properties. The degradation via hydrolysis of PLA proceeds relatively slow [53]. At the moment, a lot of research is done on the mixing PLA blends, which should result in a composite with desired properties [54]. This approach allowed to tune the degradation rate to favored values and simultaneously maintain sufficient mechanical strength.

Due to the excellent heat processability [50], PLA qualifies perfectly for additive manufacturing (AM) techniques. Besides acrylonitrile butadiene styrene (ABS), PLA is one of the most common polymers used in fused deposition modeling (FDM).

## 2.2. Hybrid structures

The idea of hybrid structures is to join similar or dissimilar materials to benefit from material-specific properties. For example, it is possible to reduce the weight of a component by substituting specific parts with a substructure made from a different material (e.g. metal or polymer). Simultaneously, the functional properties (e.g. stiffness, fatigue strength, or energy adsorption) are maintained or enhanced. Some parts manufactured from magnesium alloys take over structural tasks in the automotive industry and reduce the car's overall weight. Classically magnesium hybrids are joined by welding (e.g. friction steer welding, laser beam welding), clinching, riveting, adhesive bonding, or by combinations of different approaches. [10, 55]

The aerospace and automotive industries are particularly interested in joining metals and polymers to form hybrid structures. Out of the different joining techniques, the *direct-adhesion polymer-metal hybrid technology* should be highlighted. In this injection molding technique, no supplementary elements (e.g. rivets, edges, or adhesives) are used to form the interface connection. The aim is to achieve high adhesion strengths by utilizing mechanical, chemical, and physical adhesion mechanisms. [55]

11

## 2.2.1. Mechanisms of adhesion

Interface adhesion can be categorized into three fundamental mechanisms: mechanical, chemical, and physical adhesion. Macroscopic mechanical adhesion is based on the infilling of the surface texture (surface roughness, pores, and gaps) by a polymer, which results in hooking or interlocking. Further, interdiffusion at a microscopic scale between two materials (e.g. crosslinked polymer chains) is also part of mechanical adhesion. Chemical adhesion treats with the bonds between the surface atoms (covalent or ionic bonding). The strength of the chemically bond surface naturally depends on the bond type. Electrostatic interactions, hydrogen bonds, and van der Waals are part of the physical interaction mechanisms. Van der Waals interactions occur between molecules with fluctuating polarizations and electrostatic adhesion is based on the exchange of electrons between conducting materials. [56]

In this thesis, the focus of the discussion will be on hooking and interlocking (Figure 4). Those are assumed to be the main contributors to the adhesion of metal-polymer hybrid structures. The contribution of chemical adhesion to bond strength can be considered minor since magnesium alloys have low surface energies [10].



*Figure 4: Mechanical adhesion modes a) hooking b) interlocking*

## 2.2.2. Bioresorbable Mg-PLA hybrids

Since magnesium and its alloys tend to show high corrosion rates, much research on organic polymer and inorganic coatings and their ability to protect the implant was carried out. Besides corrosion resistance, polymer coatings can foster other functions such as biodegradability, *"biocompatibility, self-healing, drug-delivery, and osteoinduction"*. [51]

In some studies, Mg-alloys dip-coated with PLA showed increased corrosion resistance. It was noted that the coatings' surface adhesion was not high since mechanical adhesion is the driving mechanism. Also, the agglomerated hydrogen gas from magnesium's degradation (see chapter 2.4.1) beneath the coating is considered responsible for coating ruptures. In other approaches, investigations on PLA-Mg-composites were executed where either wires made out of Mg-alloy [57], pure Mg particles [58], or magnesium hydroxide [$Mg(OH)_2$] [59] were used to reinforce a PLA matrix. Butt et al. molded PLA (injection molding) around surface-treated Mg-alloy rods

and studied the mechanical properties (tensile and bending) and corrosion resistance during eight weeks of immersion in SBF [60]. They found that this direct-adhesion metal-polymer hybrid structure showed a significant increase for both of those properties. [51]

# 2.3. Methods applied

## 2.3.1. Fused deposition modelling

Fused deposition modeling (FDM) is a very sophisticated AM method that made its way – not only into scientific and industrial applications – but also in the commercial and DIY sectors. Its popularity is attributed to the possibility to net-shape a part. Furthermore, it is a swift process and the commercial materials are not expensive. Over the last years, FDM machines became more user-friendly and the variety of different polymer filaments also increased. One significant disadvantage is that the strength in print direction (z-direction) is much lower than in the x– and y-direction. Compared to other AM techniques, FDM is considered to be an easy-to-use and cheaper process. The fact that the material utilization is relatively high and that no chemical treatments have to be executed on the finished print makes this technique well-fitting for biomedical purposes. [61, 62]

The fundamental principle (Figure 5) is the extrusion of a semi-molten polymer along a programmed path directly on a build plate. One complete path at a constant height is called a layer. The polymer solidifies shortly after extrusion so that the model can be built up layer by layer. The polymer's heating slightly above the transition or melting point happens in the lower part of the print head right before the extrusion through a nozzle. An extruder guarantees a constant feeding of the polymer filament. A mounted fan, in combination with passive cooling, prevents the print head from overheating. Commonly in FDM printers, the print head is attached to an x- and y-axis, which actuates the movement. Depending on the printer model, the z-movement is either executed by the print head or the build plate itself. Elevated temperatures facilitate the polymer's adhesion on the build plate, which is crucial for a successful print. For this reason, most of the printer models are also equipped with a heated build plate. [61, 62]
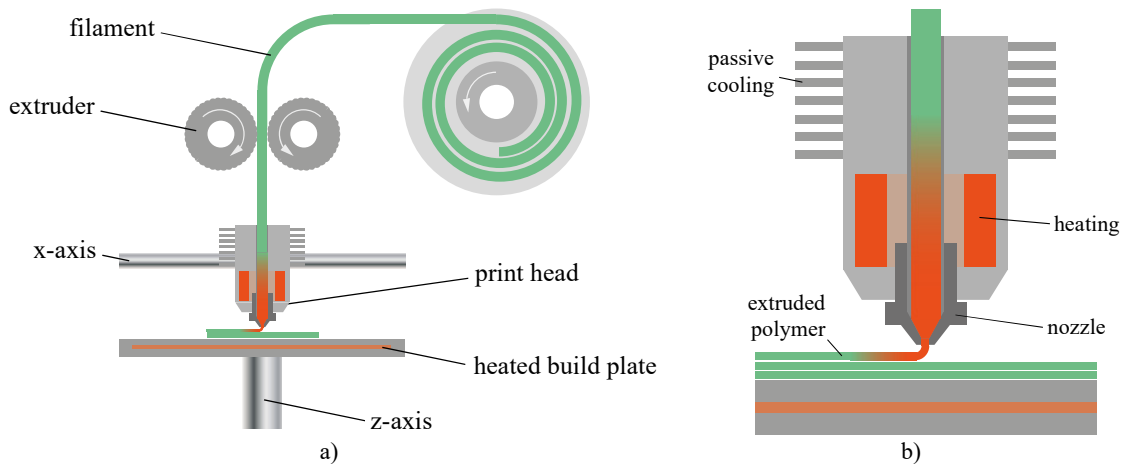
*Figure 5: Schematic illustration of a) the FDM process and b) a printhead*

## 2.3.2. Electron beam welding

Electron beam welding (EBW) is a process where energy is introduced into the weld via accelerated electrons. These electrons are generated by a beam generator consisting of a cathode connected to high voltage and an anode (Figure 6a). The beam generator and the coils are operating under a high vacuum environment. The emitted electrons at the cathode get accelerated towards the anode. After the electrons passed the anode, they go through a focusing coil and a deflection coil before they finally arrive at the substrate. The substrate is placed in an enclosed working chamber with radiation shielding and under a high vacuum. A high vacuum is required to prevent electron beam scattering at the air molecules. The EBW process does not require any additional welding material (e.g. wire) to join two different materials, extremely high energy densities are achieved, and very deep welds can be manufactured. The main machine parameters which influence the welds are the *accelerating voltage*, *beam current*, *lens current*, *focal position* (normal, under, or over-focused), *welding speed*, *beam deflection* (e.g. circular, triangular), and *beam pulsing*. Figure 6b illustrates the principle of the keyhole technique for welding two tick parts. [63]

Magnesium and zinc exhibit low melting points and high vaporization pressures. Therefore, the weldability in the EBW process, as well as with other welding techniques, is considered to be critical [10, 63]. The literature on welding recommends defocusing the electron beam while processing Mg-alloys and advises to avoid welding of Mg-alloys with more than 1% zinc [64].
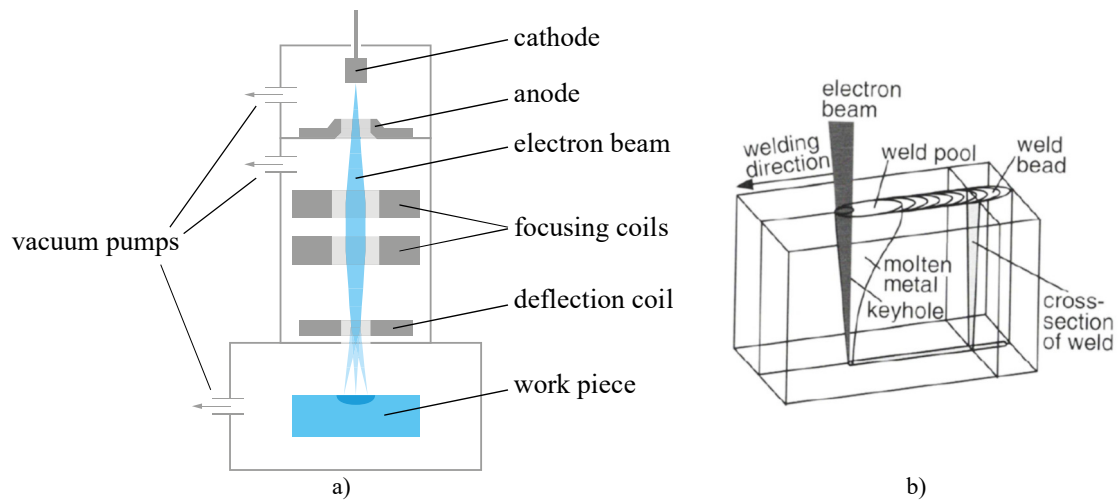
*Figure 6: EBW a) Components of an EBW machine b) keyhole technique [65]*

Besides joining different materials, the electron beam process (EBP) is used for additive manufacturing, surface modification, cladding, hardening, or alloying. During surface modifications, the beam deflection is utilized to raster larger areas on surfaces. [66]

# 2.4. Corrosion mechanisms

In corrosive environments, metals transform into more energetically favorable, respectively, more stable compounds. Dependent on the environment's chemical composition, compounds such as oxides, hydroxides, or sulfides form. [67]

## Galvanic corrosion

When two dissimilar metals or alloys are in contact and immersed in an electrolyte, a corrosion mechanism called galvanic corrosion emerges. The less electronegative metal cathode's corrosion rate decreases during this process, while the more electronegative metal anode shows increased corrosion. The difference in electrode potentials can be derived from the galvanic series and determines the degree of galvanic corrosion. [67]

## Pitting corrosion

Pitting corrosion can occur in the presents of aggressive ions, where the formation of a protective passivation layer is locally inhibited. In those regions, galvanic corrosion occurs due to an emerging potential gradient between the protected (cathode) and unprotected (anode) surface. This leads to increased corrosion and results in the local pits and holes. [67]
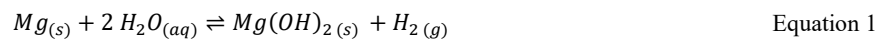
## Crevice corrosion

Crevice corrosion, like pitting corrosion, is also based on localized corrosion due to the hindered formation of a protective passivation film. However, crevice corrosion takes place at low rates in tiny crevices and typically does not lead to macroscopic corrosion artifacts (pits and holes). So that crevice corrosion can occur, these microscopic gaps have to be sufficiently big enough that the corrosive fluid can penetrate but at the same time small enough that excessive fluid exchange is prevented. Thereby two coupled and chemically different environments with a potential gradient emerge. [67]

Further, intergranular corrosion and stress-corrosion cracking also have to be considered. During intergranular corrosion, the grain boundaries exhibit a promoted corrosion rate due to a potential gradient towards the inner grains. Metals exposed to stress in a corrosive environment exhibit stress-corrosion cracking. Those can exhibit boosted crack formation, which reduces the fatigue limit. [67]

## 2.4.1. Corrosion behavior of magnesium

During the corrosion of magnesium, the dissolved magnesium ions react with the water, which results in the precipitation of a protective magnesium hydroxide [$Mg(OH)_2$] layer on the material surface and the evolution of hydrogen gas ($H_2$) (Equation 1). Equation 2–4 show the partial electrochemical reactions of this transformation. [15]

$$Mg_{(s)} + 2\,H_2O_{(aq)} \rightleftharpoons Mg(OH)_{2\,(s)} + H_{2\,(g)} \qquad \text{Equation 1}$$

$$Mg_{(s)} \rightleftharpoons Mg^{2+}_{(aq)} + 2\,e^- \qquad \text{Equation 2}$$

$$2\,H_2O_{(aq)} + 2\,e^- \rightleftharpoons H_{2\,(g)} + 2\,OH^-_{(aq)} \qquad \text{Equation 3}$$

$$Mg^{2+}_{(aq)} + 2\,OH^-_{(aq)} \rightleftharpoons Mg(OH)_{2\,(s)} \qquad \text{Equation 4}$$

In Figure 7, the fundamental corrosion reactions in magnesium and the corresponding reaction products are illustrated.
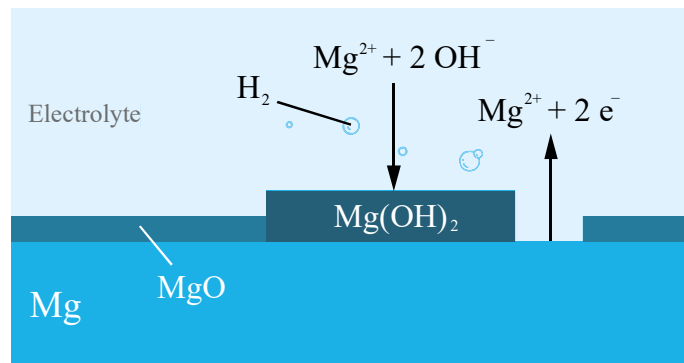
*Figure 7: Corrosion mechanism and hydrogen evolution of Mg*

## Environmental influences on the degradation behavior of magnesium

Inorganic ions (e.g. Cl⁻) facilitate the corrosion since they break up the protective passivation layer on the surface. In contrast, ions such as hydrogen phosphates, hydrogen carbonates, and $Ca^{2+}$ can inhibit corrosion due to the formation of precipitates that passivate the surface. Further, the chosen buffering system can either promote corrosion when a pH is regulated by the consumption of hydroxide ions (OH⁻) or decrease it by forming protective magnesium carbonates. Studies have indicated that the adsorption of organic molecules (e.g. proteins) on the surface of Mg-alloys led to decreased corrosion rates in the first stage of immersion corrosion. When immersion time proceeds, the protection from adsorbed proteins mitigates. Contrary to Fe-alloys, the presents of dissolved oxygen minorly influences the formation of corrosion products [$Mg(OH)_2$] in Mg-alloys. Lastly, mechanical stresses significantly increase the degradation rates of the Mg-alloys. [9]

## Influence of surface heat treatments on magnesium alloys

Some heat treatments are executed to induce a refinement of the grains and increase the corrosion resistance [68]. Iranshahi et al. showed that EBP treatments of AZ91 magnesium alloy resulted in lower corrosion rates from electrochemical corrosion tests immersed in 3.5 wt.% NaCl [69]. Other studies indicate that the laser surface treatment of Mg-alloys increased the corrosion resistance of the surface [70, 71]. Recently, Yao et al. compared the electrochemical corrosion behavior of bulk material and surface treated – performed on an SLM machine - Mg-Zn-Ca-alloy (extruded) carried out in SBF with no additional pH control measures. Initially, the surface-treated specimen showed an increased $H_2$ evolution until the extruded sample overtook after ~60h of immersion [72]. Contrary, they found that treated Mg-Ca-alloy showed lower corrosion rates before ~155h.

17

## 2.4.2. Degradation mechanisms in polymers

Hydrolytic and enzymic degradation are the most prominent degradation mechanisms present in polymers under physiological conditions. The type and degree of degradation are mainly dependent on the biological environment (e.g. pH, temperature, enzymes) and the polymer's properties (chemical, physical, and morphology properties). More crystalline polymers tend to illustrate slower degradation rates compared to polymers where amorphous structure prevails. Further, high glass transition temperatures lead to decreased degradation. Additionally, the degradation behavior changes during the degradation due to physical, chemical, or morphological alterations within the polymer. A distinction is made between surface erosion and bulk degradation (Figure 8). In surface erosion, water can not infiltrate the bulk material easily (hydrophobic) and therefore, the size or geometry of the polymer changes. During bulk degradation, chemical reactions (hydrolytic or enzymic) break up chemical bonds throughout the material so that water can diffuse into it. [73]

*Figure 8: Modes of biodegradation a) surface erosion b) bulk degradation [73]*

### Hydrolytic degradation

Increased hydrophobicity of a polymer hinders hydrolytic degradation since the chemical bonds are less likely to be dissolved by water. This results mostly in surface erosion where the degradation from bond cleavage is much stronger than from water diffusion. Such polymers are considered suitable for drug delivery applications since the surface gradually erodes to the inside. Contrary, bulk degradation occurs in more hydrophilic polymers where the bond cleavage is present in the bulk material and water can diffuse easily. This significantly changes the bulk properties (e.g. molecular weight, mechanical properties) of the polymer. [73]

### Enzymic degradation

Plenty of polymers also degrade by cleavage of bonds through an enzymic attack. Again the degree of bulk degradation or surface erosion is dependent on the enzyme's ability to penetrate the polymer structure and its chemical stability. Enzymes can be added to the polymer to control the enzymic degradation behavior (bulk degradation or surface erosion) and to form degradable polymer blends. [73]

## Degradation of PLA

PLA is categorized as a poly (α–hydroxy) ester – together with PGA and their copolymer PLGA – and is considered hydrophobic. PLA implants do not show notable erosion during the first phase after implantation. As soon as the degradation is quite advanced, erosion starts to be measurable [7]. Hydrophobic methyl groups, which protect the ester bonds from being affected by water, hinder hydrolytic degradation. Nevertheless, still, bulk degradation occurs since PLA contains amorphous regions. Those regions degrade faster than the crystalline ones, which results in decreased degradation with the progression of dissolution or consumption of the amorphous regions. The dissolution into lactic acid monomers changes the local pH and enhances degradation. When it comes to enzymic degradation, PLA is prone to proteinase K. [73]
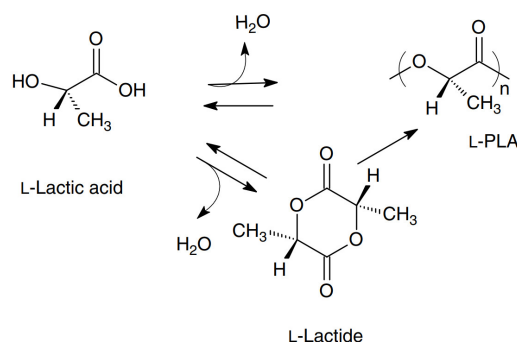


*Figure 9: Polymerization routes of PLLA [74]*

To control the degradation rates of poly (α–hydroxy) esters, the combination of hydrophobic PLA and hydrophilic PGA to form an amorphous copolymer (PLGA) has been proven successful. At a 50:50 ratio, the copolymer shows the lowest crystallinity and consequently degrades the fastest compared to other ratios. [73]

## 2.4.3. Corrosion rate determination for biomedical applications

For bioresorbable materials, it is essential to understand the corrosion behavior of materials in aqueous conditions. Ideally, the testing conditions are as close as possible to the physiological environment of the body. Besides the pH (pH range of blood plasma: 7.32 – 7.42) [75] and temperature (36.5 – 37.5°C) [76], it is also essential to mimic the chemical environment of the human body. For this purpose, different aqueous buffering solutions were developed. The most common ones are normal saline (not buffered), phosphate-buffered solution (PBS), simulated body fluid (SBF), and *Hank's Balanced Salt Solution* (HBSS). Each of them has a different chemical composition (Table 5). Consequently, the results from the corrosion experiments are very much dependent on the used electrolyte. [77, 78]

*Table 5: Chemical composition of electrolyte solutions [78]*

| Electrolyte | NaCl | KCl | KH$_2$PO$_4$ | Na$_2$HPO$_4$ + 12 H$_2$O | MgSO$_4$ + 7 H$_2$O | CaCl$_2$ | NaHCO$_3$ | MgCl$_2$ + 6 H$_2$O | C$_6$H$_{12}$O$_6$ |
|---|---|---|---|---|---|---|---|---|---|
| NS    [g/l] | 9.0 | – | – | – | – | – | – | – | – |
| PBS   [g/l] | 8.0 | 0.2 | 0.2 | 2.89 | – | – | – | – | – |
| HBSS  [g/l] | 8.0 | 0.4 | 0.06 | 0.06 | 0.06 | 0.14 | 0.35 | 0.1 | 1.0 |
| SBF   [g/l] | 8.0 | 0.4 | 0.06 | 0.12 | 0.2 | 0.14 | 0.35 | – | – |

There are different methods to examine and measure the corrosion behavior of materials in aqueous solutions. In principle, they can be categorized into polarized and unpolarized methods and each has its advantages and limitations. Unpolarized experiments would be the corrosion rate determination by mass loss or H$_2$ evolution measurement. The advantages of mass loss experiments are that the setup is simple and the costs are relatively low. A drawback is that it only delivers an absolute corrosion rate and does not show the corrosion behavior over time. The evolution measurement provides more detailed information about the time-dependent corrosion. However, the setup for H$_2$ evolution is more complicated. Polarized experiments require special equipment (e.g. potentiostat, cell). A prevalent one is the potentiometric polarization technique, based on cathode-anode-reactions and reveals information about the corrosion behavior with an applied potential. The electrochemical impedance spectroscopy is particularly suitable to characterize the corrosion of surfaces. It is a non-destructive method, which means that a single sample can be used for plenty of measurements before it has to be replaced. [79]

# 2.5. Motivation

By introducing an add joining procedure for polymer-metal hybrid structures new types of biomedical products can be developed or existing bioresorbable implants' functionality could be improved. Polymers can potentially protect the metal from corroding too fast and, therefore, maintain the mechanical integrity of the implant. This is considered a very promising benefit of such hybrids. A literature review has shown attempts of joining metals and polymers to utilize the different properties. However, when it comes to add joining of such hybrids, scientific publications are rare.

Moreover, the treatment of funnel chests (lat. pectus excavatum) of children is considered a potential practical application for such metal-polymer hybrids. A hybrid structure could unite the strength and stiffness of the metal with the polymer's elastic properties. This could mimic the properties and the functional interaction of the bones and cartilages within the thorax.

This project explores a direct-adhesion joining approach based on novel AM techniques.

# 3. Experimental

Figure 10 illustrates an overview of the used materials, applied methods, and follow-up investigations. The add joining of a metal-polymer hybrid structure was executed by FDM with PLA. To tune the corrosion behavior and to generate a topography, the Mg-alloy was surface structured by EBP. Subsequently, mechanical and in vitro corrosion tests were carried out on the resulting hybrid structure. Before and after the respective processes and testing method, the samples were characterized. A variant of a hybrid material produced from a Zn-alloy powder at an SLM machine was postponed in this thesis. In section 6 the first experiments and occurring challenges of printing zinc powder via the SLM process are briefly discussed.
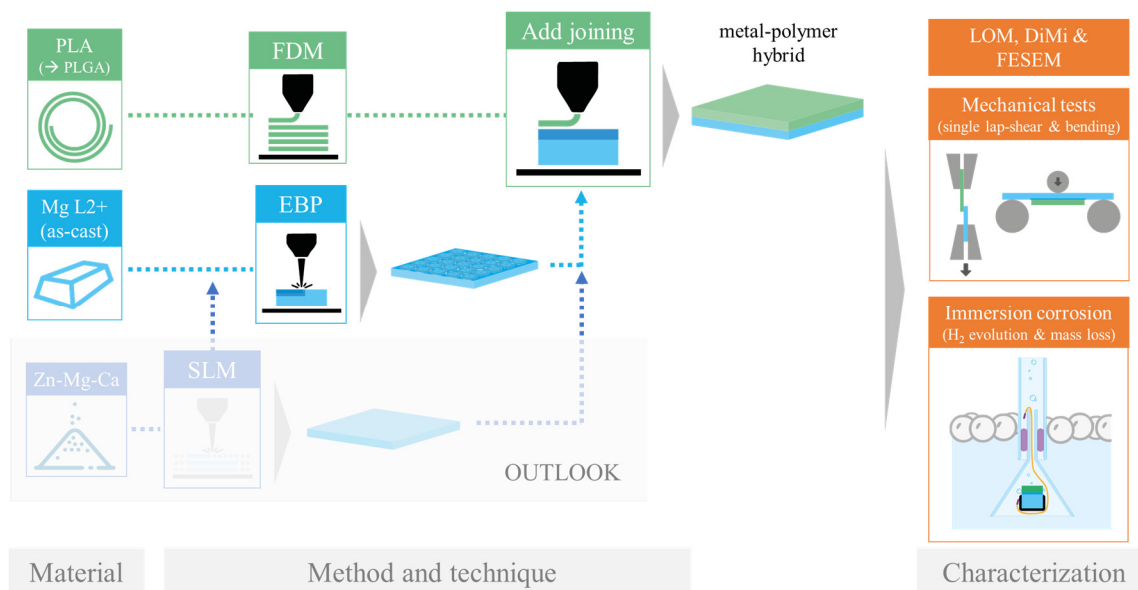


*Figure 10: Overview – Materials, methods, and investigations*

## 3.1. Materials

A brief overview of the used materials and how they were prepared for the experiments will be described in the following section.

### 3.1.1. Mg-Zn-Yb-Ca-Zr-alloy (Mg L2+)

The experiments were carried out on biocompatible as-cast Mg-Zn-Yb-Ca-Zr-alloy plates, subsequently referred to as Mg L2+. Those plates were cut off from a casted block in an earlier project and had dimensions of 100x100x6mm. Since the plates were significantly oxidized, they were ground as a whole (Figure 11) before the next processing steps at the EB machine.



a)                                                                        b)

*Figure 11: Mg L2+ plate a) oxidized b) ground as a whole*

### 3.1.2. Polylactic acid (PLA)

There are plenty of polymers already used for different biomedical applications (see chapter 2.1.2), but not all of them met this project's requirements. The polymer should display a balance between sufficiently high enough degradation rates, good mechanical properties, and the polymer's processability during the FDM process. Additionally, the accessibility on the market was also taken into account. Poly lactic-co-glycolic acid (PLGA) was found to be an excellent fit to meet those requirements. However, due to its costs, it was decided to start the first investigations with a chemically related and very sophisticated polyester, Polylactic acid (PLA). Besides that, the degradation rate of 12-24 months is considered very low, PLA exceeded the other requirements compared to PLGA [48]. For the experiments, *BASF Ultrafuse®* PLA filament (pearl white, d=2.85mm, 750g) was bought.

### 3.1.3. Sample preparation for metallography

## Embedding

Since most magnesium alloys are quite temperature-sensitive [80], and the used auxiliary polymer had a low melting range (145-160°C [see appendix]), cold embedding was the means of choice. For the embedding, *STRUERS LevoCit Powder + Liquid* was prepared according to suppliers' ratios and poured into the mold where the samples were placed beforehand. When multiple samples were put together in one mold, some instant glue was applied to prevent the samples from tip-over or from shifting to unfavorable positions. After the embedding was fully cured, the probe

was undrawn from the mold, briefly deburred, dot peened to guarantee unambiguous identification, and now ready for the upcoming grinding and polishing procedure.

## Grinding and polishing

According to the recommended procedure steps (Table 6) from previous diploma theses [81, 82], the grinding and polishing were executed on a semi-automatic STRUERS Tegramin-30 preparation system.

*Table 6: Grinding and polishing steps [81, 82]*

| Grit size | Suspension | Time [min] |
|---|---|---|
| 500 | Water | 3 |
| 800 | Water | 3 |
| 1200 | Water | 3 |
| 2000 | Water | 4 |
| 4000 | Water | 5 |
| Struers MD-Nap | 1 μm Struers DiaDuo-2 (diamond suspension) | 10 |

From the first to the last step, the force was kept at 5N, on the one hand, not to grind off too much of the soft material, but more importantly, to prevent mechanical twinning of the magnesium structure [10]. Before and after the polishing step, the sample was cleaned for three minutes in a *Bandelin SONOREX TK 52* ultrasonic bath filled with ethanol. In the last 30s of the polishing step, the polishing plate was rinsed with ethanol to remove the suspension residues and prevent the sample surface from corroding.

## Etching

For the Mg-alloy's metallography investigation, the grains, and therefore the grain boundaries had to be made distinguishable. This was achieved by grain boundary etching, which resulted in a notable increase in contrast at the grain boundaries. Again, the procedure was derived from a preceding thesis [81], but with small adjustments due to slight material composition differences. The embedded Mg L2+ specimens were immersed for only 3s in the etchant (Table 7) to prevent over-etching.

*Table 7: Ingredients of picric acid-based etchant [81]*

| Ingredient | Quantity |
|---|---|
| Ethanol | 100 ml |
| Distilled water | 10 ml |
| Acetic acid | 5 ml |
| Picric acid | 2.1 g |

The specimens were now ready for the metallographic investigations.

### 3.1.4. Characterization

The Mg-alloy and the surface modifications were characterized by light optical microscopy (LOM) *ZEISS Axio Observers z1m* and field-emission scanning electron microscopy (FESEM or SEM) *Tescan Mira 3*. Further, energy-dispersive x-ray spectroscopy (EDX, Octane Plus detector EDAX-Ametek) was used to determine the chemical composition of the alloy. The surface topographies after the EBP and the corroded samples were analyzed at a *KEYENCE VHX-6000* digital microscope (DiMi).

Since PLA, like most polymers, is not conductive, the samples had to be sputtered with a thin carbon layer to examine them in the SEM. To not melt or burn the polymer surface, the SEM was operated in low-voltage mode.

The fracture surfaces of the add joined hybrid samples were investigated at the DiMi and the SEM.

## 3.2. Surface structuring by electron beam process

A *pro-beam machine EBG 45-150 K14* (pro-beam GmbH & Co. KGaA, Germany) was used for the experiments. Besides welding, surface treatments can also be executed with an electron beam (EB) by thermal processing of a surface. In such treatment, the EB rasters small patterns (e.g. star-, line-, triangle- or hexagon-shaped) consisting of points. The beam can heat or even melt the surface region. The specific energy input is mainly controlled by the acceleration voltage, beam current, scanning speed, lens focus, focal position, beam deflection, and pulse frequency (Figure 12a) [63]. Due to the electron beam's kinetics, the melt pool on the surface is displaced as the EB moves along the scanning path. The displaced melt pool solidifies again and a ramp-shaped structure remains [83]. A repetition of the scanning cycles results in a pile-up of the displaced material (Figure 12b).
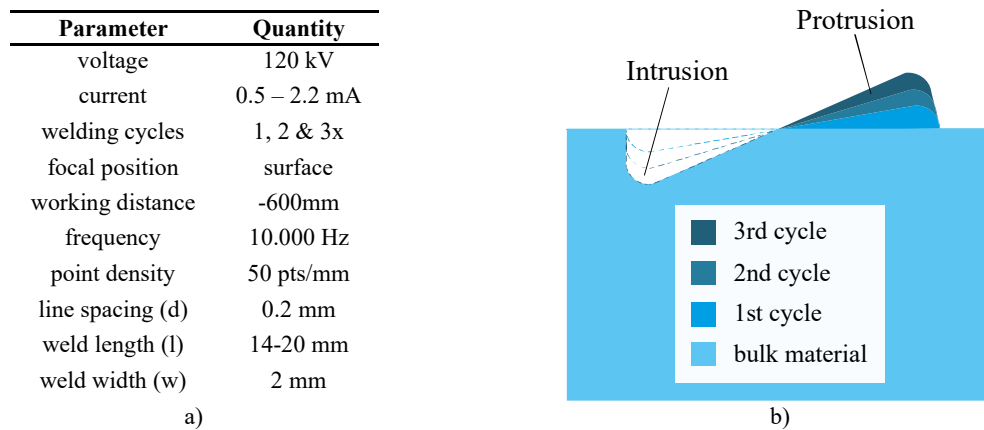
| Parameter | Quantity |
|---|---|
| voltage | 120 kV |
| current | 0.5 – 2.2 mA |
| welding cycles | 1, 2 & 3x |
| focal position | surface |
| working distance | -600mm |
| frequency | 10.000 Hz |
| point density | 50 pts/mm |
| line spacing (d) | 0.2 mm |
| weld length (l) | 14-20 mm |
| weld width (w) | 2 mm |

a)

*Figure 12: EBP a) experimental parameters b) principle of pro- and intrusion*

## 3.2.1. The setting of parameters for the surface structuring

Different scanning patterns (line-welds, star-shaped, and circular) were carried out for a qualitative parameter study of Mg L2+ during the EBP. However, in the course of this project, the line-shaped pattern was chosen to be investigated in particular. This method resulted in a grooved topography. The line pattern is built up by beam path pairs, which are shifted parallel by a constant line spacing ($d = 0.2\ mm$) (Figure 13a). The path pairs start in the center and travel in a counter direction from there. The line spacing $d$ was selected considering the energy distribution and melt pool size. To complete one line-weld cycle ($l = 20\ mm$) takes one second. Figure 13b shows the resulting groves from the experimental parameters (Figure 13c). The length ($l_b$) of one beam path is 1 mm and each path consists out of 50 points (Figure 13d).

| Parameter | Quantity |
|---|---|
| voltage | 120 kV |
| current | 0.5 – 2.2 mA (0.1mA steps) |
| welding cycles | 1, 2 & 3x |
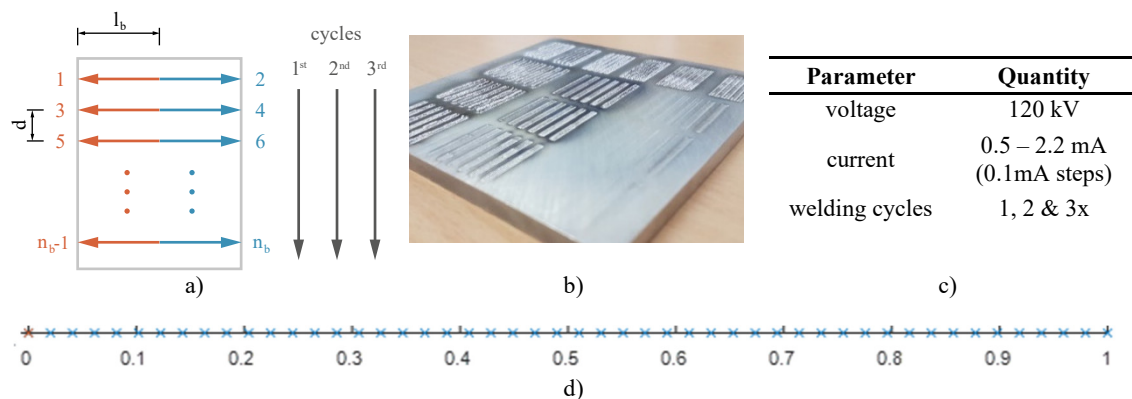
*Figure 13: EBP line-welds a) beam paths b) experimental parameters c) parameter tests on Mg L2+ d) points on the beam path*

### Slope-in and slope-out effect

An inherent property of an electron beam generator is the slope-in and slope-out effect. Slope-in occurs at each weld's starting point. It describes the gradual increase of the beam current until the beam reaches its desired intensity. Analogous, the gradual termination of the beam at the end of

a weld depicts slope-out. This results in different energy inputs at the beginning and the end of a weld cycle. [84]

To counteract the effects of slope-in / slope-out, the welding time was increased by 0.1s (3s → 3.1s) and consequently, the welding cycle also increased. This caused the initial start region, where slope-in emerged, to be scanned by the electron beam, which was already in the slope-out mode. Those two effects neutralized each other and thereby, more homogeneous grooves were created.

## 3.2.2. Sample preparation

The Mg L2+ plates were ground manually as a whole on a *STRUERS Tegramin-30* with water and at 40 rpm with moderate force (grit sizes: 80, 180 & 320). To ease handling on the grinding plate, a second Mg-plate was sellotaped with double-sided tape on top of the other. After the last grinding step, they were cleaned with ethanol. When the plate was exposed to a normal atmosphere for too long, a wire brush was used, right before it was placed into the EB machine, to break up the oxidation layer for better processability.

A line-weld was 2mm wide ($w$) and had no offset to the previous welds for all specimens. On contrary, the weld length ($l$) and the number of welds ($n$) varied for the different testing methods (Figure 14a). Figure 14b shows a plot of all the points of one line-weld. After one weld was finished 30s of idle time was coded to give the plate a chance to slightly cool down, and thereby, keep the energy input for each weld as constant as possible. This ensured a more regular weld height ($h$) (Figure 14c). In Figure 14d, the experimental parameters are shown, which should be of primary interest for the mechanical tests.



| Parameter | Quantity |
|-----------|----------|
| voltage | 120 kV |
| current | 0.8, 1.0 & 1.2 mA |
| welding cycles | 3x |
| cooling time | 30 s |
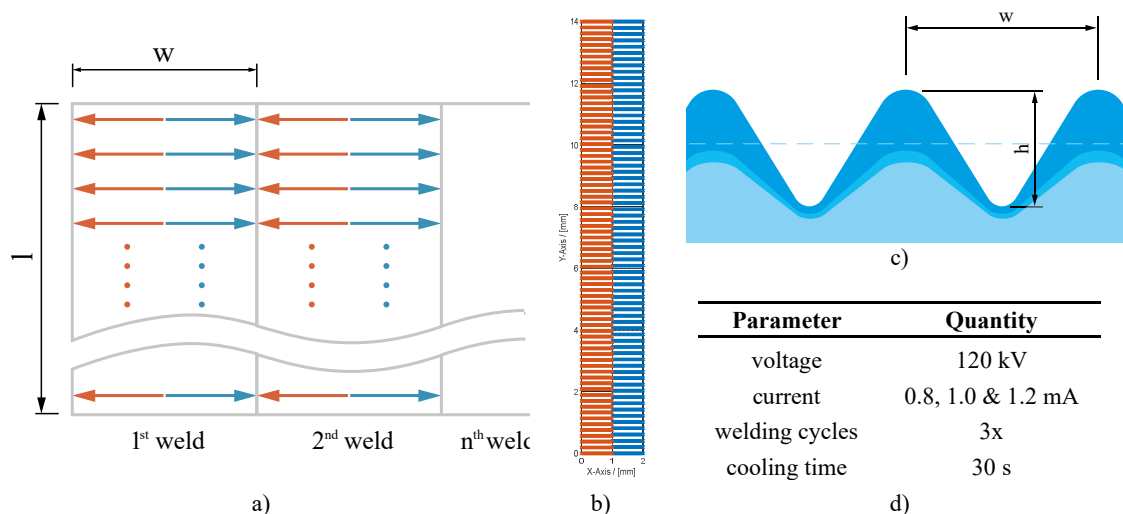
*Figure 14: Sample preparation – EBP pattern a) weld pattern geometry and arrangement b) plot of raster points c) groove geometry d) experimental parameters*

After the surface structuring, the plates were extracted from the EB chamber and put into sealed bags to prevent oxidation. The topography of each structured pattern was examined and evaluated by DiMi. Figure 15 shows topographies with the parameters given in Figure 14d. A slight beam current increase (0.2 mA steps) significantly scales the weld height ($h$) (Figure 14b).
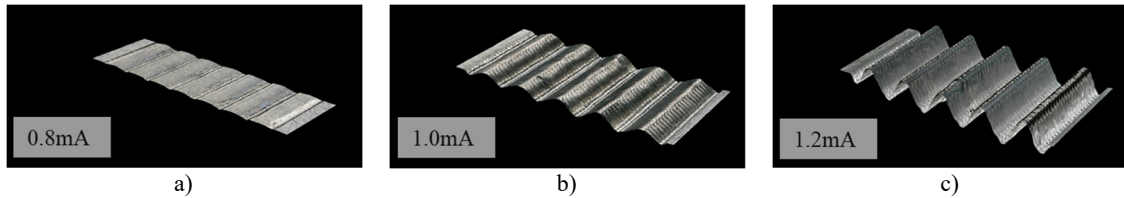


| a) | b) | c) |

*Figure 15: Topography of EB-grooves welds at different beam currents a) 0.8 mA b) 1.0 mA and c) 1.2 mA*

For the experiments, the EB-structured plates were cut into the desired sizes on a *STRUERS Accutom-10* with a *STRUERS SiC 10S15* cutting disc at 3000 rpm, low velocities (0.05 mm/s), and water-based cooling emulsion. The cut samples were immediately cleaned with ethanol, wrapped in paper towels, and put into plastic bags for safe storage to preserve the surface quality.

# 3.3. Add joining of hybrid structures

All prints were executed on an *Ultimaker S5 (firmware: 5.7.3)* with 2.85mm PLA filament combined with a 0.4 mm nozzle (*Ultimaker Print Core AA*). The computer-aided design (CAD) models were converted into a printable code with the slicer software *Cura* (version: 4.7.1). The output print file was coded in g-code (also RS-274), a commonly used programming language for computer numerical control (CNC) purposes.

Commercial FDM printers are generally made to print on the build plate ($z = 0$) and not on a substrate ($z \neq 0$). Consequently, available slicer software is not capable of processing such customizations. Therefore it was necessary to elude those constraints by implementing g-code modifications after the slicer software converted the CAD file. Due to some other software limitations – e.g. multiple bottom-layers printing and merging two different 3D models – g-code adaptions were essential. These modifications are elucidated in the appendix.

## 3.3.1. Printing parameter tests

The optimal printing parameters to achieve the polymer's ideal mechanical properties (UTS) and the polymer-metal-hybrids were determined by printing PLA tensile samples. Samples were printed according to the standard ISO 527-2 [85] (Figure 16a), with different parameter sets by varying the nozzle temperature, layer height, and printing speed (Figure 16b). The layers were

arranged orthogonally at an alternating angle (45°, 135°, 45°, …). A statistical model, according to Box-Behnken, was used to gain meaningful results.

## Box-Behnken design

This design of experiments (DOE) tool is a statistical method that delivers a response surface of the input and output variables and has a reputation for providing convincing results. Figure 16c illustrates the design model for three input variables. The red dots and the blue dot in the cubic center each represent a set of parameters. The blue dot is of special interest since the more replicants printed with these parameters, the more reliable the attained response surface will be. This, of course, also applies to the other lattice points. One advantage of the Box-Behnken design over comparable models is that fewer points in the multidimensional lattice – respectively, fewer parameter sets – have to be tested. This leads to a very efficient parameter finding. Considering all this, it was agreed to start with one sample for each of the thirteen lattice points and four replicants for the center point. In total, 17 samples were printed in a randomized order to prevent systematic errors. The model required more replicants for each point if it turned out to be not sufficiently meaningful.

The printed tensile samples were sealed in bags to hinder the absorption of moisture. Before they were tested, the cross-section at three points was measured and an arithmetical average was calculated. The tensile tests (Figure 16d) were executed on a *Zwick/Roell Z100* at 2 $mm/min$ test speed and 20$N$ preloading force.
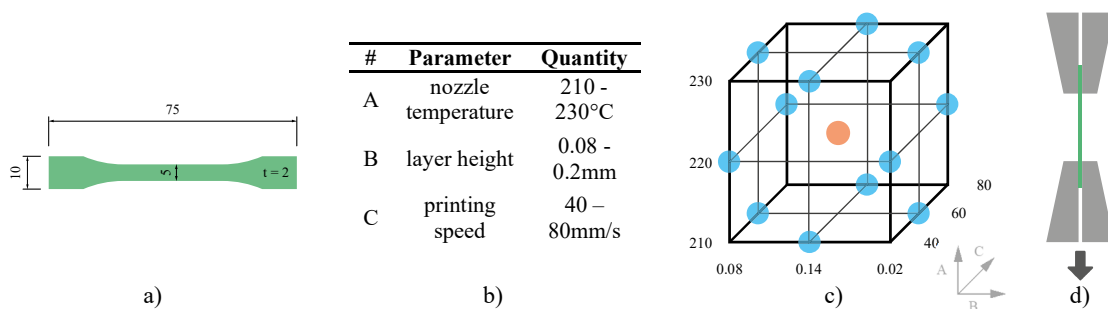


*Figure 16: Parameter tests and DOE a) tensile sample ISO 527-2 Type 1BA [85] b) printing parameters c) Box-Behnken design with three input variables d) tensile test setup*

## 3.3.2. The intrusion of PLA into EB grooves

The polymer must penetrate the gaps and surface irregularities to achieve good mechanical properties of the hybrid bond. With this infiltration, the mechanical adhesion (hooking & interlocking) increases (see chapter 2.2.1).

The degree of intrusion mainly depends on the polymer's viscosity. This viscosity is determined by the polymer type and the working temperature. Consequently, the higher the temperature, the

lower the viscosity. For this reason, the nozzle temperature was set at the upper limit (230°C) of the filament suppliers' recommendation and the building plate temperature was set at 140°C to preserve the semi-molten polymer's viscosity as long as possible.

An additional measure to utilize the infilling was to increase the number of the bottom layers printed without a movement in the z-direction ($z = 0$) before the build-up of the other layers continued. Figure 17 shows a schematic illustration of the intrusion behavior with an increasing number of bottom layers. In the case of a print with ideal intrusion, all the gaps should be filled without any cavities (Figure 17c). Except for the bottom layer, which was printed with the same orientation (0°), the follow-up layers were arranged orthogonally in an alternating raster angle (90°, 0°, 90°, …).

Another method to facilitate the degree of filling was to heat the printed specimen slightly above the polymer's melting range and subsequently apply mechanical force from above. This approach and its influence on intrusion and mechanical properties were not investigated in this thesis. Though, a more tender treatment was exerted by solely heating the printed sample 30°C above the melting range (145-160°C) for 10 minutes without any auxiliary force – except the force of gravity – applied. For this qualitative test, only one EB-parameter set (1.2mA beam current; 3s welding time) was used, which resulted in high welds ($h \sim 1.3\ mm$), and in total, seven bottom layers were printed.
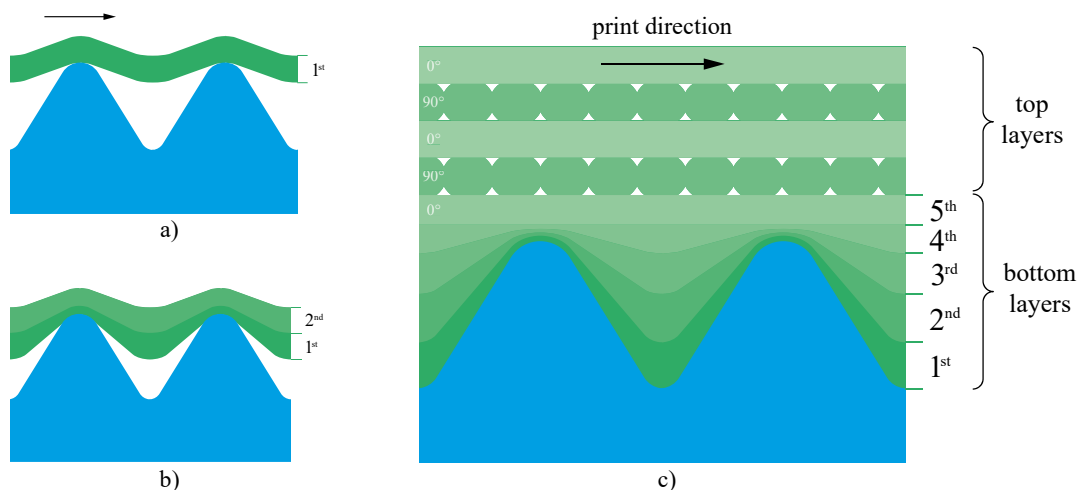


*Figure 17: Intrusion of multiple bottom layers a) one bottom layer b) two bottom layers c) ideal intrusion with five bottom layers including top layers*

### 3.3.3. Mechanical characterization

The mechanical tests were carried out on a *Zwick/Roell Z100* with different test setups, test speeds, and preloading forces.

### 3.3.3.1. Single lap shear test (derived from ASTM D1002-10)

The testing procedure and dimensions of the metal substrate, the interface region, and the printed polymer are based on the standard ASTM D1002-10 (Figure 18a-b). The specimen's length and width were scaled down due to the limited build chamber size of the initially planned selective laser melting (SLM) process. Also, the costs of the metal powder, as well as of the biomedical polymer filaments, are relatively high. The thickness was increased, which had the advantage that it guaranteed testing the stresses in the interface bonded region and not, in case of a rupture in a different point, the bulk material itself. For the lap shear tests, the clamps were shifted from the center to guarantee that the shear plane is aligned parallel to the direction of force (Figure 18c). The test speed was set at $1 \, mm/min$ and preloading force was $0 \, N$.

*Figure 18: Single lap shear standard dimensions a) ASTM D1002-10 [86] b) standard modification c) experimental setup*

As mentioned before, the Mg L2+ substrates were structured with three different beam currents (0.8, 1.0 & 1.2 mA). After inserting the plate in the EBP chamber, the patterns were structured in one run with approximately two minutes of idle time before starting a new structuring pattern. Figure 19 shows a schematic of the pattern arrangement on the plate and the final lap shear substrate, which is ready for the add joining process.
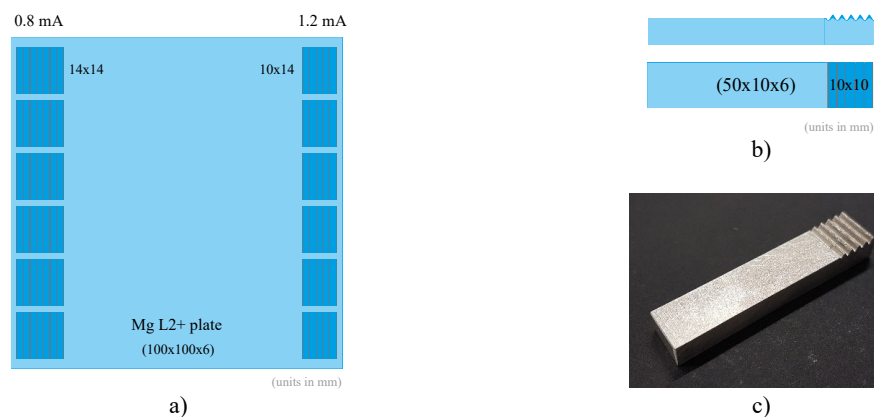
*Figure 19: EB-structuring of lap shear samples a) arrangement of 0.8 & 1.2 mA samples b)  c) finished single lap shear substrate*

Due to the difference in the height of the standard build plate and the print's actual starting point, an auxiliary build plate was required. This build plate was custom-made from stainless steel and was placed together with the metal substrate on the heated standard print plate (Figure 20). Since there were different topography heights and preparation inaccuracies, each sample had to be printed at a different height. Thereby, three grub screws were mounted to adjust each print's height. Another effect was the thermal insulation of the stilted build plate from the heated build plate below. This was considered useful since the polymer should exhibit lower viscosity in the Mg/PLA interface region. The fact that stainless steel has a comparable low heat conductivity [87], which results in a slower heat uptake, also facilitated this positive side effect of higher viscosity in the PLA/build plate interface.

Nevertheless, the auxiliary build plate requires a minimum temperature to enable the polymer adherence on the build plate. To generally increase the adhesion, a heat resistant polyimide (PI) tape was applied. Also, for the fixation of the substrate and the auxiliary plate PI-tape was used. Like in the intrusion experiment, the bottom layers were printed with the same orientation (0°). Contrary, the follow-up layers were tilted (45°,135°,45°,…) to achieve a maximum UTS. This layer orientation sequence was maintained throughout all experiments (single lap shear, 3-point bending, and corrosion experiments). For each parameter set (Figure 20c), at least three samples were manufactured.



| Parameter | Quantity |
|---|---|
| nozzle temperature | 230 °C |
| layer height | 0.2 mm |
| printing speed | 40 mm/s |
| build plate temperature | 140°C |
| number of 1st layers | 1x (0.8mA) 3x (1.0mA) 5x (1.2mA) |
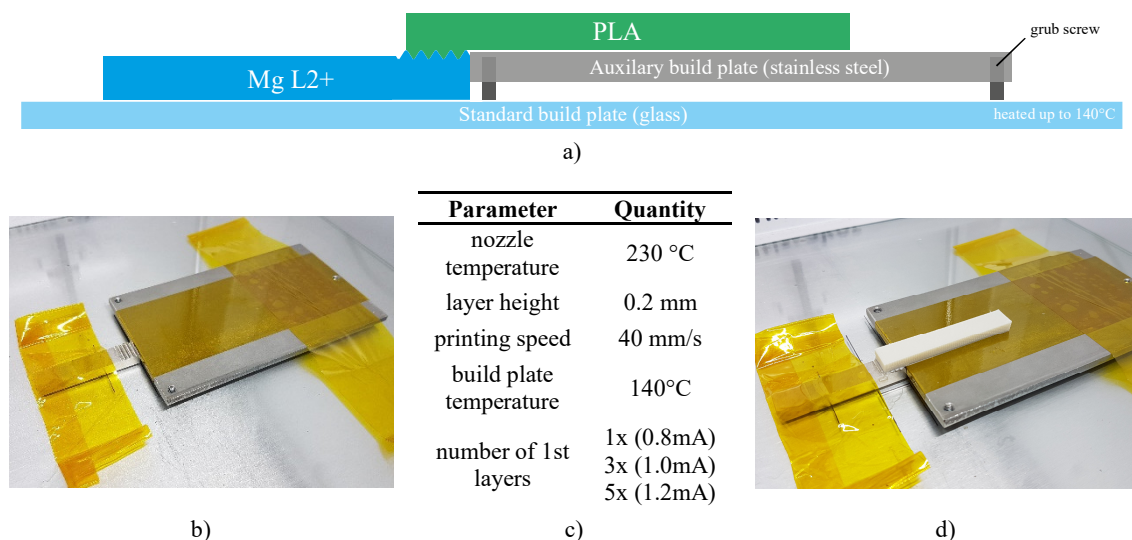
*Figure 20: Single lap shear sample – Add joining setup a) schematic b) before printing c) experimental parameters and d) finished print job*

For each state, at least two samples were re-melted on an external heating plate at 180°C – 20°C above the melting range – for 15 minutes.

### 3.3.3.2. 3-point bending test (derived from DIN EN 1996)

The standard DIN EN 1996 [88] characterizes the adhesion of structural adhesives, molded onto substrate surfaces, by the 3-point bending test. The goal of this test was to measure the stresses where the adhesive delaminates. Additionally, qualitative evidence of the delamination propagation – abrupt or steadily – was deducted. Instead of downsizing, the standard had to be scaled up this time. This was because the testing device was designed for bigger specimens. The support rolls have a diameter making it impossible to decrease the distance between them without a collision with the add joined polymer (Figure 21a-b).
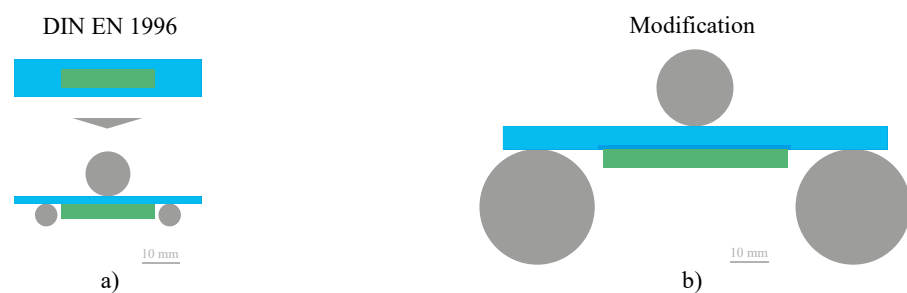


*Figure 21: 3-point-bending test a) DIN EN 1996 vs. b) scaled experiment*

The second type of modification was developed to mitigate the resistance to bending of the metal substrate (Equation 5 and Equation 6), where the metal substrate was cut in half (Figure 22b). The corners were modified to prevent the edges from colliding when the sample bends. The same EB and FDM parameters as for the single lap shear samples were used.

$$W_1 = W_{metal} + W_{polymer} \qquad \text{Equation 5}$$

$$W_2 = W_{polymer} \qquad \text{Equation 6}$$

$W$ … momentum of resistance in the center
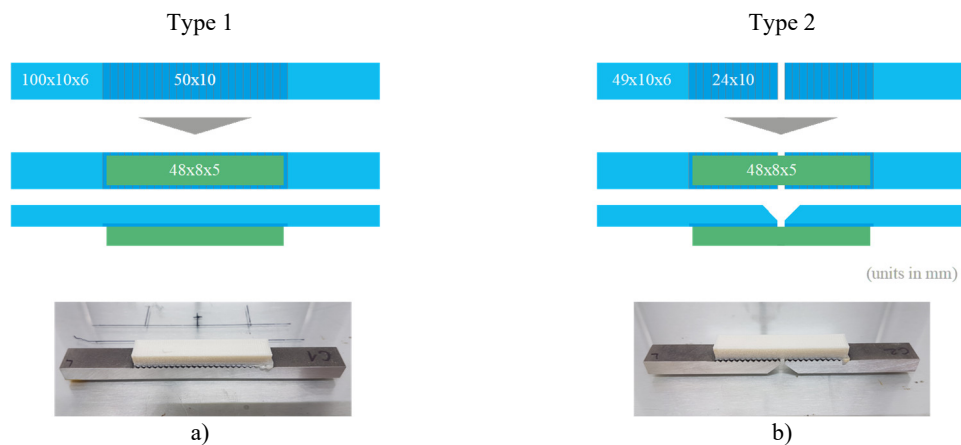


*Figure 22: 3-point bending samples a) type 1 b) type 2*

Figure 23a-c shows the bending test device and the setup for the two different sample types. A time-lapse (5-second interval) was captured to monitor the bending and delamination propagation. For each parameter set, only one sample was printed. The test speed was $0.5\ mm/min$ and preloading force was $50\ N$.



*Figure 23: 3-Point bending testing setup a) bending tool b) type 1 c) type 2*

## 3.4. In vitro corrosion

A publication by ETH Zurich [89] set the pattern for the build-up of the carbon dioxide buffered ($CO_2$-buffered) corrosion setup. In the adapted setup (Figure 24), the samples were wrapped with a flex wire, where both ends were painted with nail polish to encapsulate the copper strand. The wired samples were mounted underneath a glass funnel attached to a burette to measure the hydrogen gas evolution ($H_2$ evolution). A beaker filled with 1.5l of Hanks' Balanced Salt Solution (HBSS) (Table 8) was slowly heated up to 36-37°C on a hot plate stirrer connected to a sheath resistance thermometer (Pt 1000) for temperature feedback. Then the burettes were put in place and filled up by the use of a Peleus ball. The sealing between the funnel and the burette was custom-made out of the collar of nitrile gloves. A disadvantage of the open system – besides the eventual contaminations from the environment – is that the HBSS can evaporate during the experiment. The surface was covered with hollow polypropylene (PP) spheres to diminish this evaporation. The coverage resulted in a decreased surface area exposed to the atmosphere. Despite everything, approximately 150ml had to be added every two days because evaporation still occurred.

*Table 8: Chemical composition of Hanks' Balanced Salt solution [78]*

| Electrolyte | NaCl | KCl | KH$_2$PO$_4$ | Na$_2$HPO$_4$ + 12 H$_2$O | MgSO$_4$ + 7 H$_2$O | CaCl$_2$ | NaHCO$_3$ | MgCl$_2$ + 6 H$_2$O | C$_6$H$_{12}$O$_6$ |
|---|---|---|---|---|---|---|---|---|---|
| HBSS [g/l] | 8.0 | 0.4 | 0.06 | 0.06 | 0.06 | 0.14 | 0.35 | 0.1 | 1.0 |

The height changes over time of the fluid column in the burettes represent the evolved hydrogen gas and were documented by hand four times a day – optimally early in the morning, midday, afternoon, and evening. A reference burette without a sample was placed in the beaker to exclude errors due to other gas accumulation under the burette and the column's thermal expansion.

CO$_2$-buffering was performed with a gas diffusor to mimic the physiological pH conditions over time. The buffering system was connected to an automatic valve (*JBL CO2-magnetic valve ProFlora v002 2+ JBL ProFlora SafeStop*), which was triggered by a pH control unit (*JBL PROFLORA pH-Control Touch*). This control unit measured the pH and temperature continuously. If the pH exceeded the upper limit ($pH \geq 7.53$), the CO$_2$ valve opened to counteract and decrease the pH again until it reached 7.33. At this point, the valve closed, but the pH further decreased for three main reasons: Firstly, there was residual gas in the pipe system that caused the bubbling of the gas diffusor to continue for a few seconds. Secondly, since it took some time for the fluid to mix thoroughly, the measured pH was only a local value and did not represent the overall pH-value. Lastly, any pH electrode has an inherent response time.



a)                                                    b)
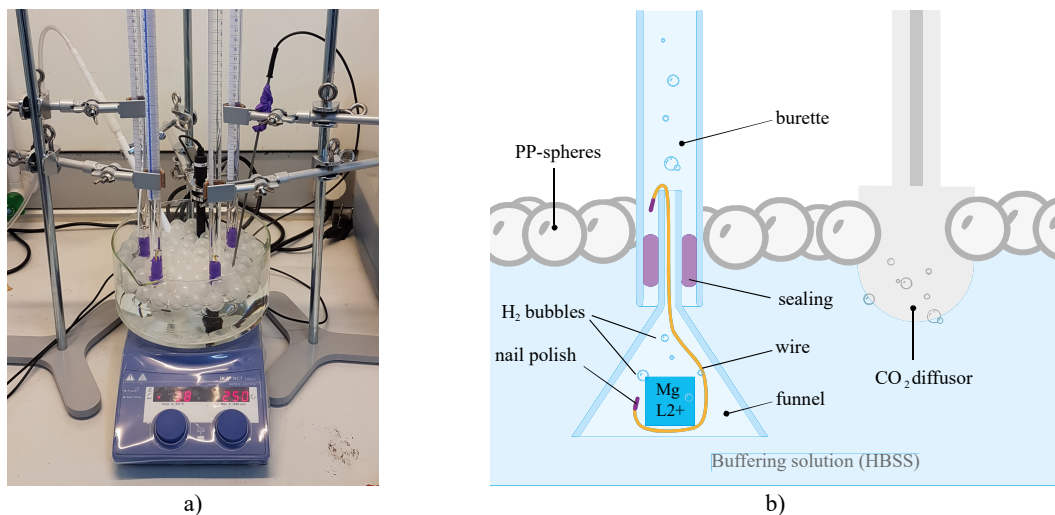
*Figure 24: In vitro corrosion test a) setup with CO$_2$-buffering system b) scheme of the setup, modified from [89]*

A time-lapse (5-minute interval) of the pH and the temperature, measured by the pH control unit, was recorded and evaluated. In Figure 25, two representative graphs of the pH and temperature evolution during the experiments are illustrated.
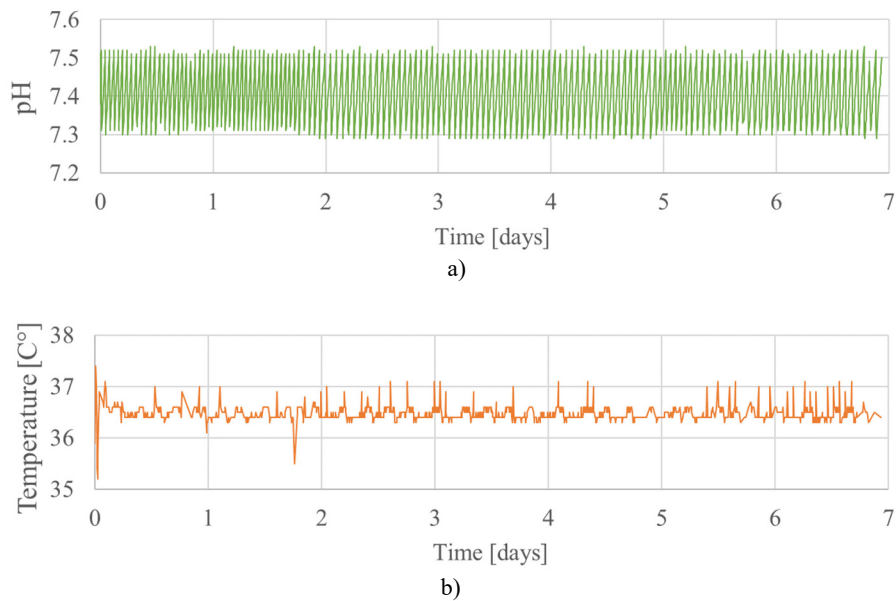
*Figure 25: In-vitro corrosion a) pH evolution and b) temperature evolution Mg L2+ (as-cast) over seven days*

## 3.4.1. Sample preparation

For all the corrosion experiments, three samples were tested to get statistically significant results. The following chapters elaborate on the steps before and after the corrosion experiment for materials with different starting conditions.

### 3.4.1.1. Mg L2+

For this Mg-Zn-Yb-Ca-Zr-alloy different conditions were investigated for seven days. First, the base material was examined to gain fundamental insights into the as-cast corrosion behavior. Subsequently, the corrosion progression of the EB-structured surface was monitored. Additionally, the corrosion in the interface between PLA and Mg L2+ was explored. For each condition, the sample preparation was different and the surface area exposed to corrosion varied significantly.

### As-cast condition

The samples were cut on a *STRUERS Accutom-10* with a *STRUERS SiC 10S15* cutting disc into thin plates (8x8x2mm). The samples were then stored in a desiccator. Before the corrosion experiments, the samples were ground by hand (#800/1200/2000/4000 SiC grinding paper + ethanol) to remove the oxide layer. The dimensions were not uniform due to preparation flaws. For this reason, the dimensions were measured at four randomly distributed spots and the arithmetic average was calculated. The samples were then cleaned in an ultrasonic bath with ethanol for three minutes and then dried in a desiccator. To enable the hanging of the samples,

0.6mm thick coated copper wires (*HSB Elektro Y – Draht 2x0.6mm*) were used to shape a framework around the sample with a small hook on the one end (Figure 26a). Both copper wire ends were coated with nail polish to prevent them from corroding. The wired samples were then mounted beneath a glass funnel (Figure 26b).



| a) | b) |

*Figure 26: Mg L2+ sample (as-cast) a) ground and wire-wrapped sample b) glass funnel with sealing and placed sample*

## EB-structured surface

For this condition, the preparation was quite different than for the as-cast. After the EB-structuring (see chapter 3.2.2), the patterns (0.8 mA beam current; 3s welding time) were painted with nail polish right after the extraction from the EBP machine. The nail polish layer inhibited the oxidation layer formation during the sample preparation for the upcoming corrosion experiments. Shortly before the corrosion experiment started, the nail polish was carefully removed with ethanol-soaked cotton swabs. The patterns were then cut into 10x10x6 mm blocks and the sides were ground (#800/1200/2000 SiC grinding paper + ethanol). After three minutes in the ultrasonic bath, five sides of the block were carefully dip-coated with cold embedding *Struers LecoCit (Powder + Liquid)* so that the embedding covered almost all the unchanged cast material and let cure (Figure 27a-c). The sides of the sample were grooved with a file to ease the wire wrapping.



| a) | b) | c) |
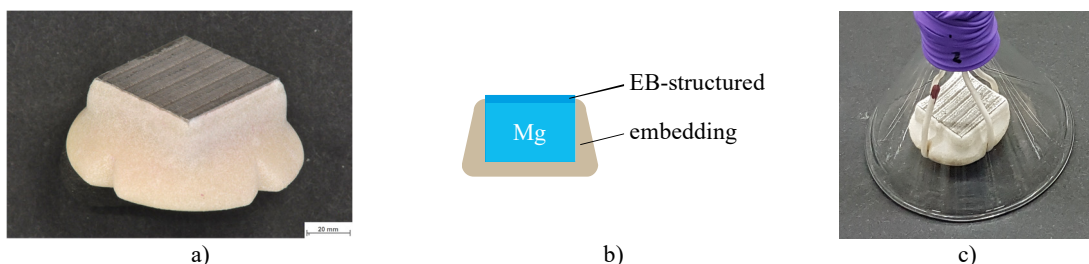
*Figure 27: EB-structured sample a) embedded sample b) cross-section c) final sample before immersion test*

It should be noted that instead of the application of nail polish to prevent oxidation, *Nital* (ethanol + nitric acid) can be used to remove the formed oxidation layer.

## Interface corrosion of add joined Mg L2+ / PLA

This experiment's focus was to evaluate the corrosion behavior of the interface region. The PLA was printed on an EB-pattern with relatively smooth topography (0.8 mA beam current; 3s welding time) and with the same FDM parameters as for the 0.8mA lap shear and bending samples (Figure 28a-b).



| Parameter | Quantity |
|---|---|
| nozzle temperature | 230 °C |
| layer height | 0.2 mm |
| printing speed | 40 mm/s |
| build plate temperature | 140 °C |
| number of bottom layers | 1x (0.8mA) |

a)                                                                      b)
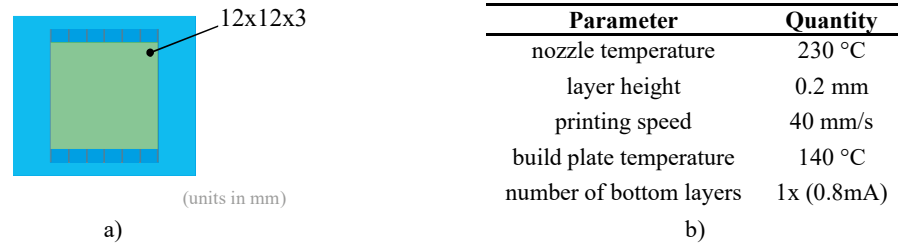
*Figure 28: Interface corrosion samples a) pre-form of add joined corrosion sample b) experimental FDM-parameters*

The small add joined metal-polymer-hybrids were carefully cut (0.05 mm/s) along the red dashed path highlighted in Figure 29a on a *STRUERS Accutom-10*. After manual grinding (#800/1200/2000 SiC grinding paper + ethanol), the interface region was pasted with tape while the rest of the bulk Mg L2+ was painted with liquid rubber (*OBI Zementbodenbeschichtung*) (Figure 29b-c). Before the corrosion experiment started the following day, the coating cured overnight (~24h) in the desiccator.



a)                                          b)                                          c)
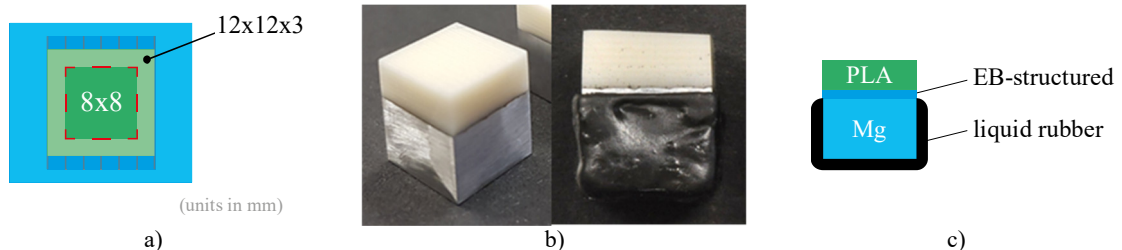
*Figure 29: Interface corrosion a) top-view of add joined sample b) before and after painting c) cross-section of painted sample*

## 3.4.1.2. Sample preparation of corroded samples

The corroded samples were retrieved from the funnels, and the flex wire was removed, rinsed with ethanol, and put into a sealed bag in the desiccator to prevent corrosion from propagating. The corrosion products had to be removed to acquire the net weight loss. This was done by immersion in chromic acid. The etched samples were neatly cleaned from the toxic chromic acid in four steps (1st water-, 2nd water-, ethanol- & ultrasonic ethanol-bath). Afterward, the samples were dried to measure the weight at the microbalance and the net weight loss was attained. Both, the corroded and cleaned surfaces were characterized by DiMi and SEM.

## Calculation of the corrosion rates from mass loss (standard G31-72)

A common standard used for immersion corrosion of metals is the G31-72 standard [90]. Despite some differences in the procedures – e.g. closed vs. open system, pH-buffering vs. unbuffered – the G31-72 standard was the means of choice to determine the corrosion rates (CR). Equation 7 describes the calculation of the corrosion rate from mass loss:

$$CR = \frac{K * W}{A * T * D}$$

Equation 7

Where:

| | |
|---|---|
| CR | corrosion rate [mm/y] |
| T | time of immersion in fluid [h] |
| A | total surface area [cm2] |
| W | net mass loss [g] |
| D | density [g/cm³] |
| K | constant to express different units |
| | = 8.76 * 104  ($\rightarrow$ mm/y) |

The samples were weighted with a *SARTORIUS microbalance* (resolution up to 0.00001g) at the chemistry institute.

# 4. Results and interpretation

This section illustrates the results of the experiments. An interpretation attempt follows each finding. After an evaluation of the materials, an analysis of the EB structured patterns and the corresponding topographies follows. Subsequently, the preliminary add joining experiments (print parameter tests and polymer intrusion) are elaborated, followed by the results from the composite samples' mechanical tests (single lap shear and 3-point bending test). Finally, the corrosion behaviors for the three conditions (bulk, EB-structured & add joined) are presented.

## 4.1. Materials

Before discussing the quantitative results, the metallographic texture and the occurring intermetallic phases (IMPs) of the Mg-alloy will be covered. Additionally, the cross-section of a PLA print will also be characterized.

### 4.1.1. Mg-Zn-Yb-Ca-Zr-alloy (Mg L2+)

The polished and embedded Mg L2+ samples were examined by LOM to get a first idea of the crystallographic structure (Figure 30a-b). The arrows highlight the mechanical twinning produced during the sample preparation. A decreasing force for the grinding and polishing steps decreases this unintentional preparation error. Additionally, after etching a few defects were observed on the surface, which might be related to etchant residuals after the surface was cleaned with ethanol.

An EDX-analysis has shown the composition illustrated in Table 9. Figure 30c-d illustrates the occurring IMPs. Literature suggests that $MgZn$, $MgZn_2$, $Mg_7Zn_3$, $Mg_xZn_5Yb$, $Zn_2Zr$, $Mg_2Ca$, and $Ca_2Mg_6Zn_3$ are present in related alloys [28, 31, 34, 35, 38]. EDX-analysis showed that Zn, Yb, and Ca are mainly found in the IMPs, while small amounts of Zr are distributed throughout the whole matrix and the IMPs (Figure 30e)

Spot 1, 2, and 4 show high amounts of Yb, which might indicate the $Mg_xZn_5Yb$ phase (Table 10). The atomic ratio of Mg and Zn in spot 3 is close to $MgZn_2$ and in spot 4 the ratio is approximately $Mg_7Zn_3$. Spot 5 shows α-Mg with small amounts of Zr (0.19wt%) and Zn (0.3wt%). These Zn/Zr-ratios suggest the occurrence of $Zn_2Zr$-nanoparticles [35]. The presents of a eutectic phase with

high Ca-contents ($\alpha$-Mg + $Mg_2Ca$ + $Ca_2Mg_6Zn_3$) could not be confirmed [9, 31]. Further investigations are required.
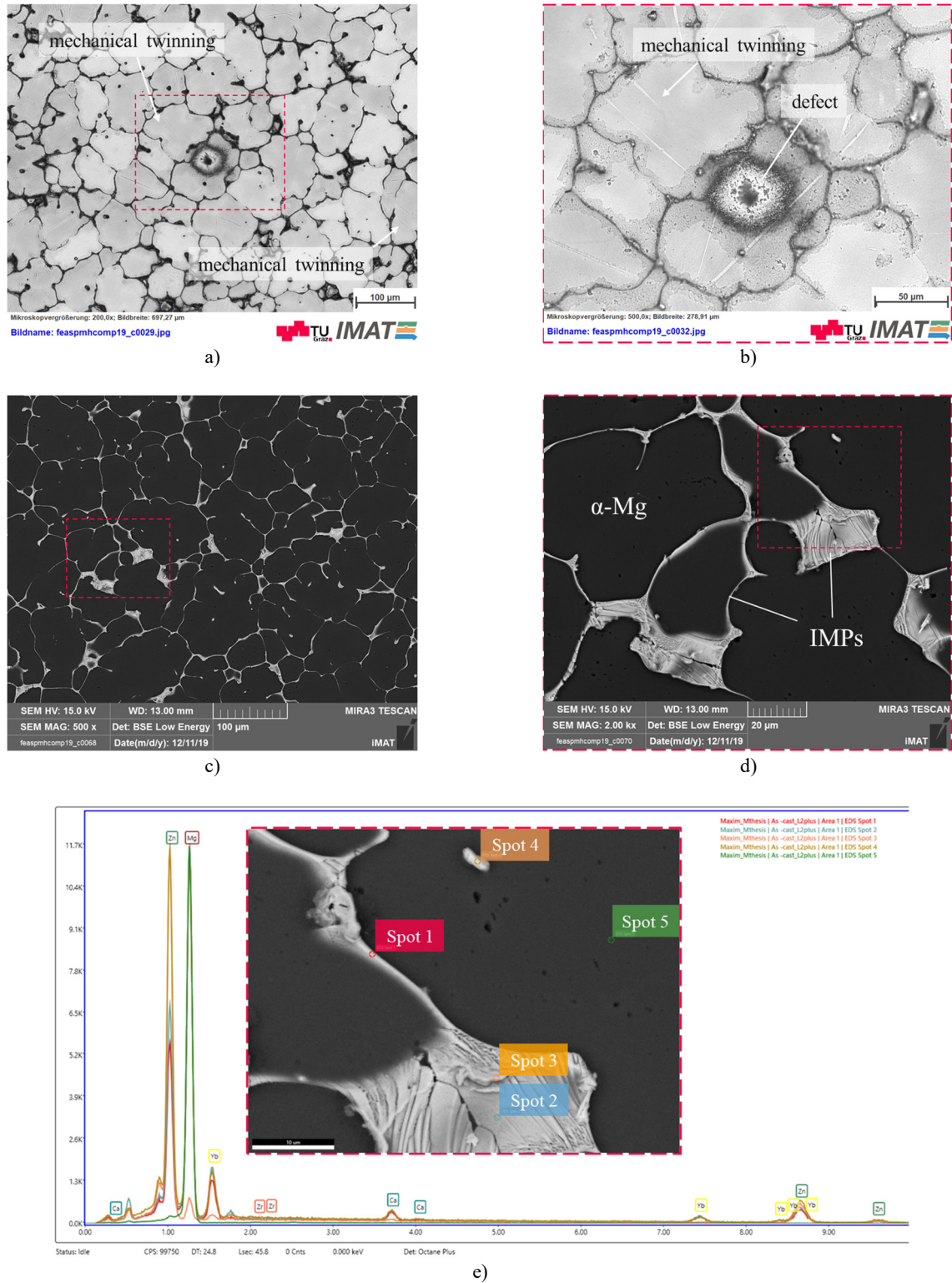


*Figure 30: a-b) Defects and mechanical twinning in Mg-L2+ (as-cast) (LOM) c-d) IMPs in Mg-L2+ (as-cast) (SEM) e) EDX-spot measurements and corresponding intensity spectrum of IMPs*

*Table 9: Chemical composition of Mg L2+ (as-cast) according to EDX-analysis*

| Element | Mg | Zn | Yb | Ca | Zr |
|---|---|---|---|---|---|
| **wt.%** | 92.02 | 5.22 | 2.14 | 0.43 | 0.18 |

*Table 10: Chemical composition (at.%) of IMPs (as-cast) according to EDX-spot measurements*

| Spot | Mg | Zn | Yb | Ca | Zr |
|---|---|---|---|---|---|
| 1 | 78.64 | 16.05 | 3.4 | 1.88 | 0.04 |
| 2 | 77.25 | 17.46 | 3.29 | 1.95 | 0.05 |
| 3 | 32.46 | 65.49 | 0.67 | 1.13 | 0.24 |
| 4 | 73.65 | 22.18 | 2.31 | 1.71 | 0.15 |
| 5 | 99.36 | 0.3 | 0.07 | 0.08 | 0.19 |

### 4.1.2. Printed polylactic acid (PLA)

The printed PLA bulk cubes exhibited many cavities. The triangular-shaped air gaps had a regular spacing between each other. Those indicate the thickness of the FDM roads ($w_L$) in the y-direction (Figure 31a-c) and the layer height ($h_L$) in the z-direction. The layers were arranged orthogonal, which is why only every second layer of those triangular cavities are observable. One can also perceive a deformation of the printed line paths in the x-direction of the 0°-layer printed on top of them. The bright particles are the flakes that are responsible for the pearl-like appearance of the PLA.
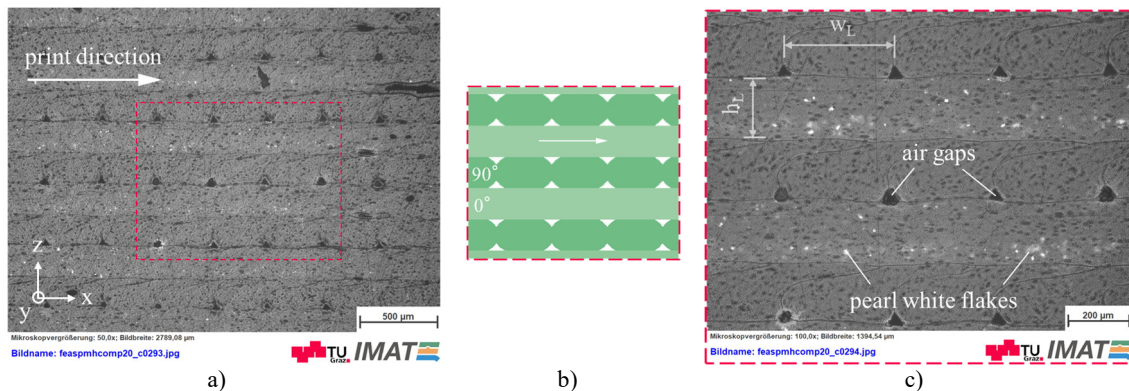


*Figure 31: PLA print cross-section a) overview b) detail schematic c) detail*

## 4.2. Surface structuring by EBP

The samples for add joining (intrusion, single lap shear, and 3-point bending tests) and in vitro corrosion experiments were equipped with line-shaped welds (grooves). An SEM image of the cross-section of a single line-weld (Figure 32a) illustrates the pile-up of the molten metal in the center of each weld, which is a result of the utilization of the protrusion and intrusion effect (see chapter 2.3.2). Also, in some of the weld cross-sections, pores were observed. These pores may

be related to the dynamic process of melt pool displacement. The different zones can be identified by looking at different grain structures (Figure 32b-c). The bulk material is unaffected, while the welded zone exhibits a significant decrease in grain sizes due to the molten material's high cooling rates. In the heat-affected zone (HAZ), partially dissipated IMPs can be observed.
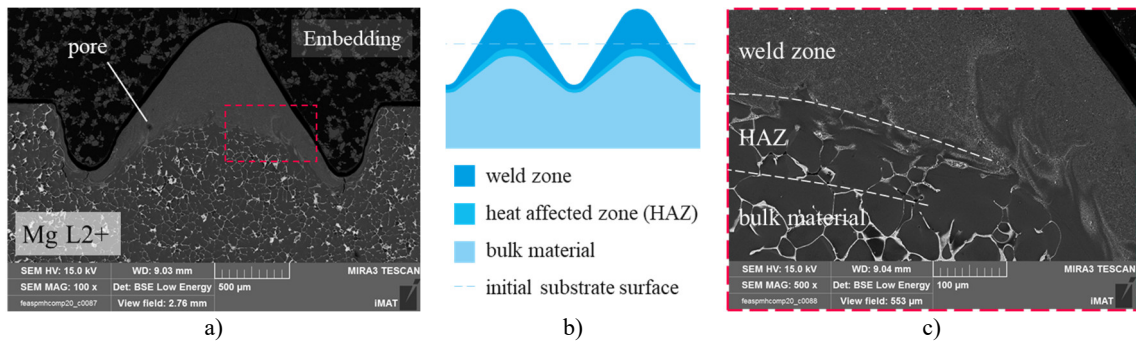


*Figure 32: Cross-section of EB-groove: a) SEM image of a single weld from the parameter study (1.3mA) b) schematic illustration of a groove-shaped EB-structure (1.2 mA) c) Detail of HAZ*

Figure 33a-c illustrates cracks in the surface regions of the line-welds. Those cracks result from the residual stresses introduced by the high cooling rates and appeared in all grooves, independent of the parameters (current or welding cycles). Such surface defects can negatively influence corrosion resistance in corrosive environments since they facilitate crevice corrosion (see chapter 2.4). A measure to counteract the cracking would be to perform the surface structuring followed by a gradually controlled cooldown of the substrates. However, this would lead to a thermal treatment, resulting in changed mechanical properties and corrosion behavior of the bulk material. It has to be evaluated separately if these changes are favorable for the desired application or not.
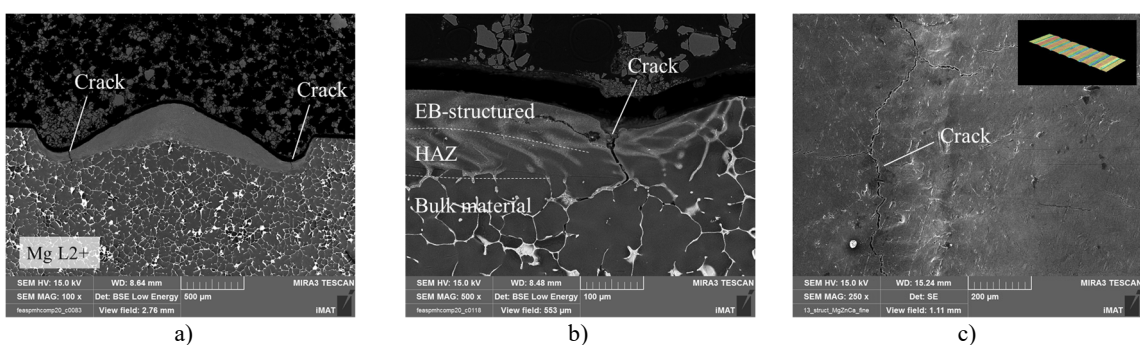


*Figure 33: Cracks in EB-grooves a) cross-section (1.1mA) b) cross-section (0.8mA) c) top view (0.8mA)*

After a qualitative evaluation of the welding behavior with different parameters, three parameter sets were selected for detailed investigations. An idle time was set between each weld to cool down the metal plate and create a weld pattern with homogenous heights. Figure 34a-c shows

exemplary weld topographies with the selected parameters, measured and analyzed at the *KEYENCE VHX-6000* digital microscope.
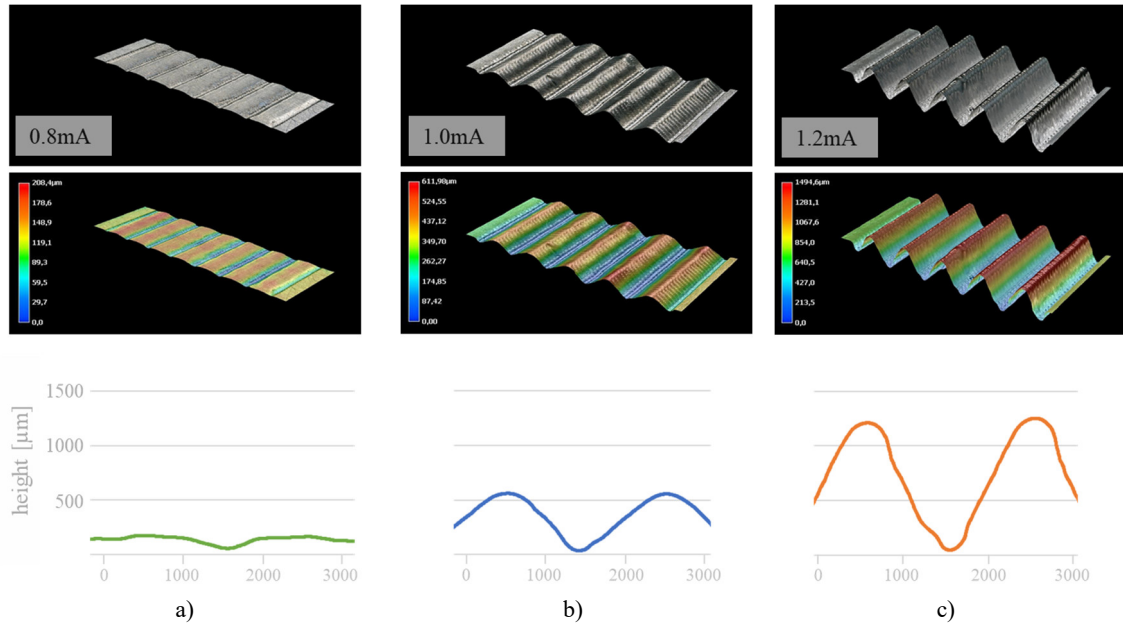


*Figure 34: Topography of EB-structured welds dependent on beam current: a) 0.8 mA b) 1.0 mA and c) 1.2 mA*

A topography mapping of patterns showed that the groove heights varied within a pattern. Figure 35a illustrates the slight increase in the height of the follow-up grooves within a pattern (e.g. LapSh-1.2-2: $h = 1272 \pm 51.4\ \mu m$). The average groove heights of six weld patterns (Figure 35b-c) structured in a row with two minutes of idle time in-between each of them also rose. These variations go back to the fact that the substrate plates heat up during the process, and therefore the absolute energy input increases as the EB-structuring proceeds. The total average height of all the 1.2mA welds of the lap shear samples is shown in Figure 35d.
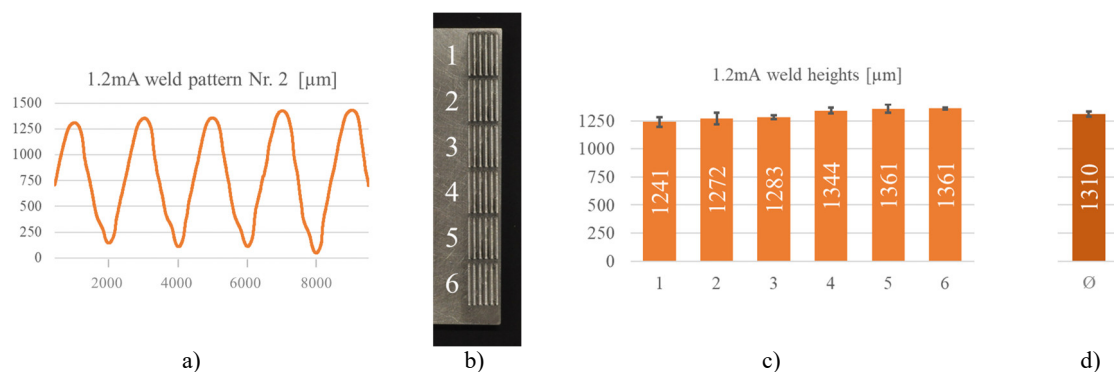


*Figure 35: Topography of line-welds a) weld height increase of 1.2mA (sample Nr.2) b) average weld heights of sample Nr.1-6 c) EB-pattern Nr.1-6 d) total average weld heights*

For the other parameters (0.8 & 1.0 mA), the results were analogous. An increased idle time between the welds or preparing separate substrate pieces can lead to more homogeneous weld heights.

# 4.3. Add joining of hybrid structures

For the add joined samples, different investigations were carried out. The intrusion with varying process parameters was looked at to understand the polymers' behavior and some influencing factors during the add joining. Subsequently, the joints' mechanical properties with different weld heights were evaluated and the corrosion behavior was monitored.

## 4.3.1. Printing parameter tests

For determining the ideal slicing parameters for PLA filament, a statistical model (Box-Behnken design) with three input variables (printing speed, layer height, and nozzle temperature) was applied. In total, 17 tensile samples (13 lattice points + 4 replicants) were printed and tested. The goal was to achieve a maximum in UTS.

The response surfaces (Figure 36a-c), each considering two parameters and the achieved UTS, show these parameter pairs' interdependence. The model suggested parameters (Figure 36d) and calculated the expected UTS (59.654 MPa) according to those computations. An examination of the statistical coefficients displayed that the adjusted coefficient of determination ($R^2(adj.) = 72.80$ %) was sufficiently high and consequently indicated that the model was reliable (Figure 36e). If those values were too low, more replicants for specific parameter sets would have to be tested.

Figure 36f shows the contribution of each parameter to the UTS of printed PLA. This indicates that the layer height has a very significant influence on the resulting UTS. A further decrease in printing speed might also lead to an increase in UTS but only with minor improvements and at the expense of sample production efficiency. An increasing extruding temperature would not only – as the graph indicates – have a positive influence on the UTS but would potentially facilitate the intrusion of the polymer into the voids and gaps of the metal substrate. Nonetheless, a temperature rise must be treated with caution since PLA degrades at higher temperatures [91].

| Parameter | Quantity |
|---|---|
| nozzle temperature ($T_n$) | 230 °C |
| layer height ($h_L$) | 0.08 mm |
| printing speed ($v$) | 40 mm/s |
| → UTS | 59.654 MPa |

d)

| Model summary | |
|---|---|
| S | 1.013 |
| $R^2$ | 88.10 % |
| $R^2$ (adj.) | 72.80 % |
| $R^2$ (pred.) | 37.73 % |

e)

f)
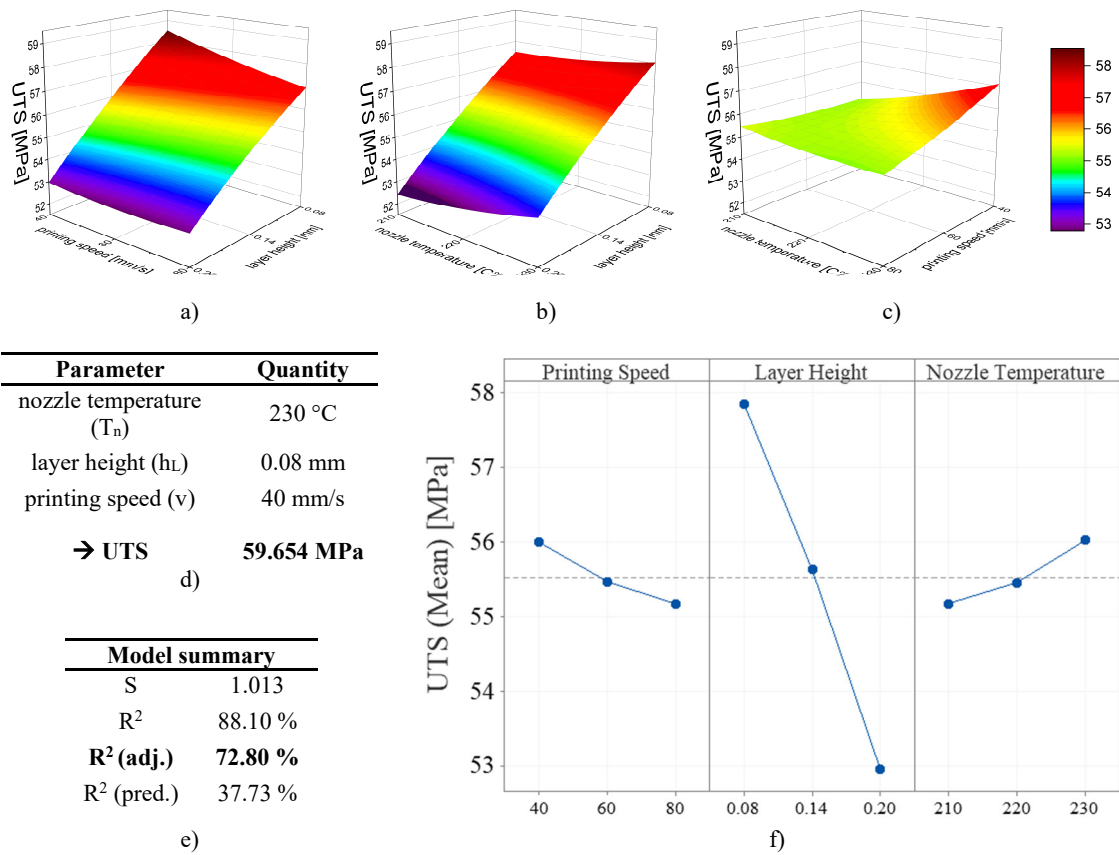
*Figure 36: Printing parameter tests for a maximum in UTS and the corresponding response surfaces a) $v$ vs. $h_L$ ($T_n = 230°C$) b) $T_n$ vs. $h_L$ ($v = 60mm/s$) c) $T_n$ vs. $v$ ($h_L = 0.14mm$) d) suggested parameters and predicted max. UTS e) model summary f) plot of main effects for UTS*

It was expected that the interface adhesion would be lower than the tensile strength of the polymer. For this reason, the layer height for all tests was kept at 0.2mm, even though this led to a lower UTS.

A morphology investigation of the tensile stress induced fracture illustrates the different characteristics of brittle failures (Figure 37a-b). The scraps result from multiple fracture propagations (textured microflow) on different planes that intersected at some point. The formation of ribbons is based on the same principle, except that the fracture planes overlap before those planes meet. [92]
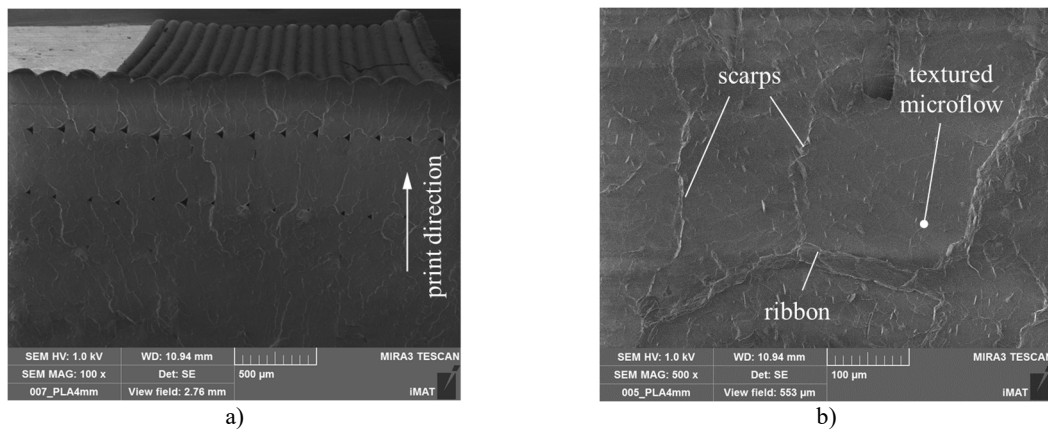
*Figure 37: a) PLA fracture surface b) failure characteristics of PLA tensile test sample*

## 4.3.2. The intrusion of PLA into EB-grooves

The polymer's infilling into the topography's voids and gaps positively influence the interface adhesion. Figure 38a-b shows a 3D-mapping of the removed PLA interface after the printing process with different parameter sets. The PLA was printed on a groove-shaped EB pattern (1.2mA). The experiments indicated that intrusion's main drivers are the polymer's viscosity and the extruded material volume (Figure 38c). This viscosity is firstly determined by the polymer's inherent properties, and secondly, dependent on the working temperatures. Thus the nozzle temperature ($T_n$) was set to 230°C, while the build plate temperature ($T_p$) was varied. Additionally, the extruded material volume varied by multiple bottom layer prints ($n_{bL}$). The results show that the intrusion depths at constant extrusion volume but elevated temperatures ($100°C \rightarrow 140°C$) increases significantly. Moreover, it can be seen that an enhanced extrusion volume ($5x \rightarrow 7x$) essentially increases the polymer infilling into the grooves.

c)
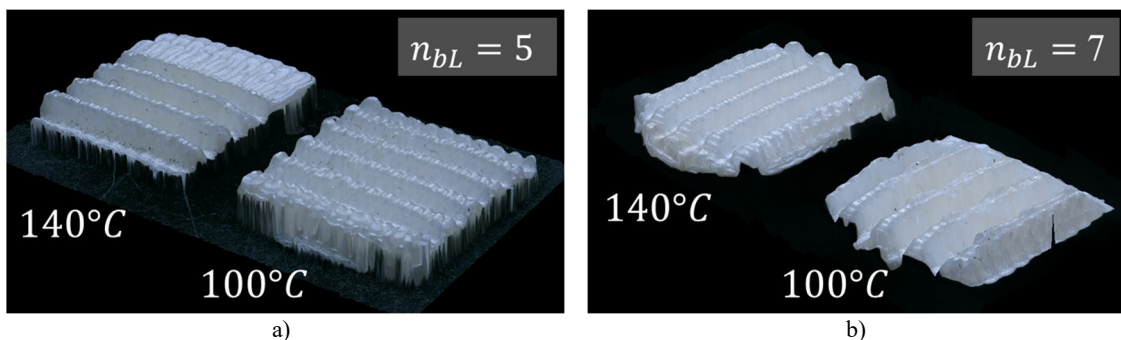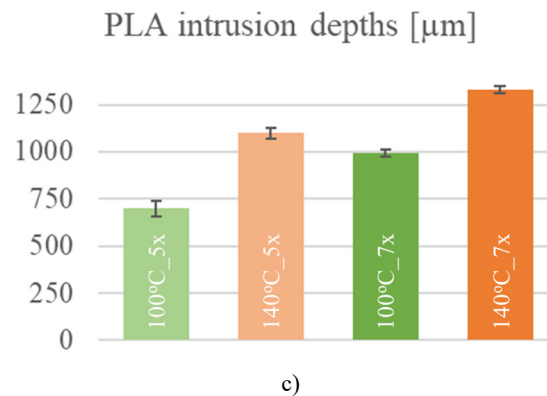
*Figure 38: Intrusion of PLA a) 3D-mapping with five bottom layers b) 3D-mapping with seven bottom layers c) Comparison of PLA intrusion depths for the different $T_p$ and $n_{bL}$*

Further tests with increased temperature parameters ($T_n$ and $T_p$) are recommended. Nevertheless, the degradation of PLA at elevated temperatures has to be considered.

Another measure to foster the intrusion is to heat the add joined sample above the melting range and hold it for some time. Figure 40 shows a filling of the cavities located in the groove valleys with PLA. Also, the triangular voids between the layers diminished. Furthermore, the layers seemed to have fused so that the bulk material appears to be homogeneous. Though re-melting facilitated the welds' infilling, it significantly decreased the interface bond's mechanical properties.
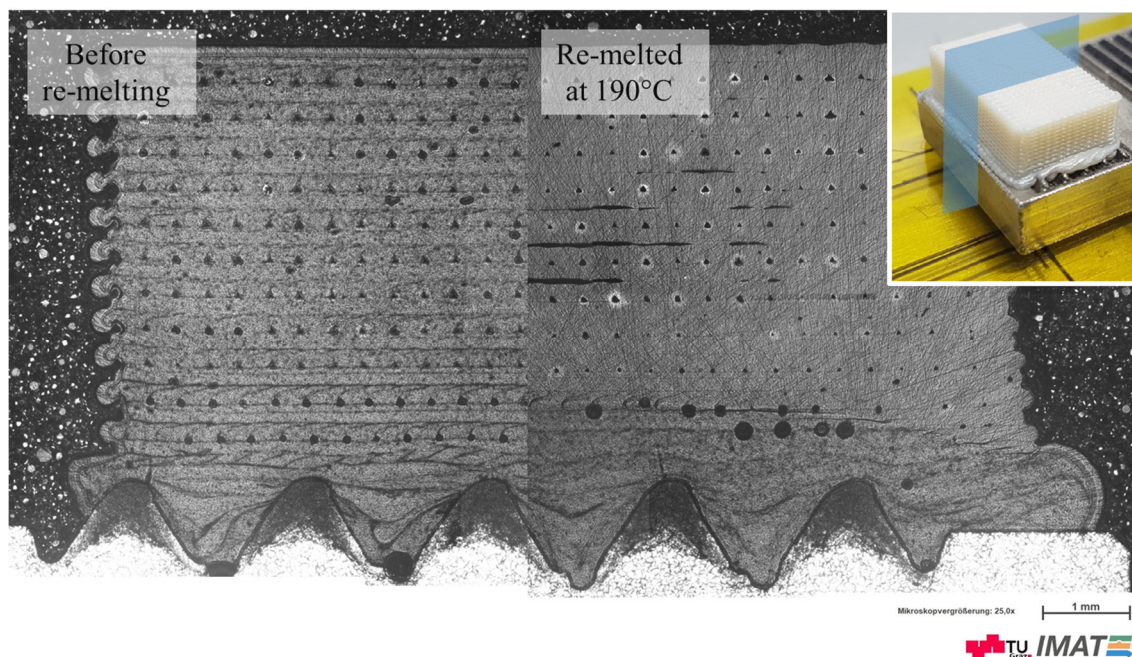


*Figure 39: Intrusion of PLA – Influence of re-melting at 190° for 10min ( $T_p$=140°C; $n_{bL} = 5$)*

### 4.3.3. Mechanical characterization

The following section discusses the mechanical characterization of the hybrid joints (Figure 40a-b), describes the quantitative results (shear and flexural stresses), and some qualitative observations.
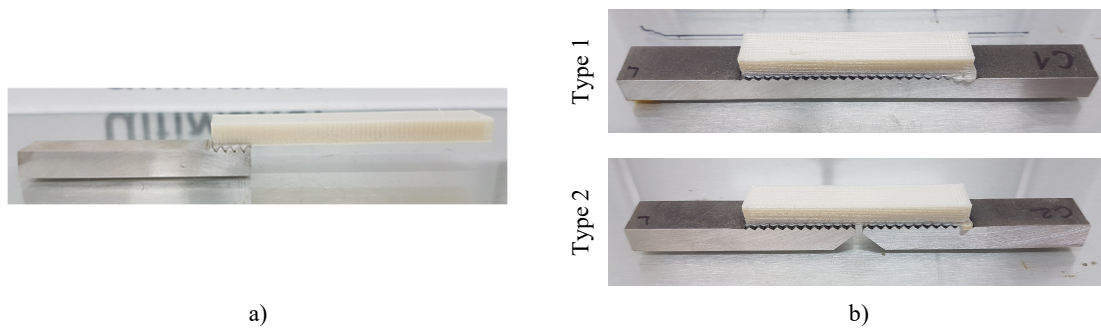


*Figure 40: Mechanical tests a) single lap shear test b) 3-point bending test – type 1 & 2*

### 4.3.3.1. Single lap shear tests

The interface regions of the printed samples were examined and measured (Figure 41a). Due to inaccuracies during substrate preparation (cutting and grinding) and the substrate's placement on the build plate, the final interface area slightly deviated from the desired area (8x10mm). Since the effective area was consulted for the strain calculations, these size variances were uncritical. Figure 41b shows the clamping setup.

The results highlighted that higher grooves lead to higher shear stresses (Figure 41c). The samples structured with a 1.2mA beam current ($h_\emptyset = 1310.2 \pm 23.8 \ \mu m$) achieved an ultimate lap shear strength (ULSS) of $12.0 \pm 1.1$ MPa. Comparable studies of Falck et al. showed joint strengths of $21.9 \pm 1.1$ MPa for add joining of an aluminum-alloy with carbon fiber reinforced polyamide [93].
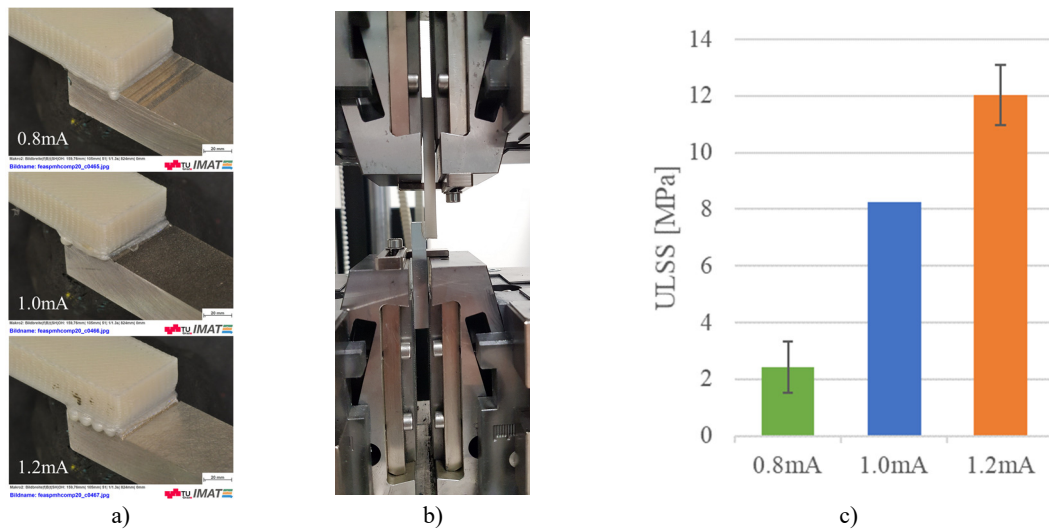
*Figure 41: Single lap shear test a) lap shear samples b) testing setup c) ultimate las shear strength (ULSS) results*

It was challenging to attain results for the re-melted samples because almost all re-melted hybrids detached before the lap shear test. Therefore, only one result from the 1.2mA-sample was retrieved, which reached 7.1 MPa. This value is ~41% lower than the average stress of the untreated samples.

## Fracture area

An examination of the fractured samples showed that significant amounts of PLA remnants were attached to the grooves (Figure 42a-b). This implies that in these regions, the interface adhesion exceeded the material properties of the polymer. The SEM image unveils that there are residues of PLA in little trenches of the weld peaks (Figure 42c). According to the modes of failure from adhesive bonds characterization, this type of fracture can be classified as a mixed failure. In the 0.8 and 1.0mA samples, adhesive failure was dominant since almost no PLA remnants were observed. [94]
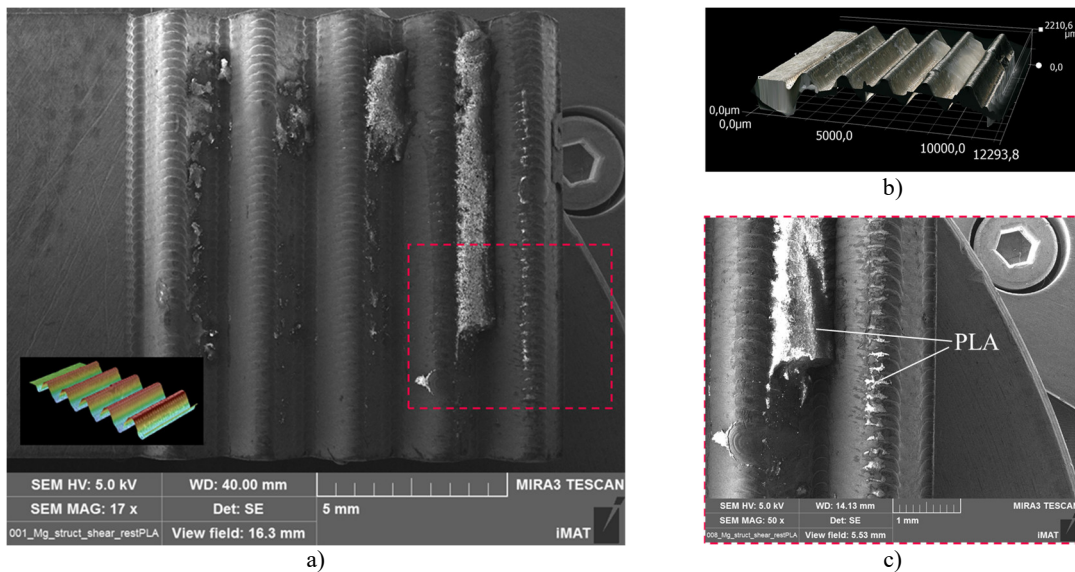
*Figure 42: Single lap shear – fractured sample with PLA residues a) SEM image of metal substrate interface b) topography analysis c) PLA residues in groove valley and peaks*

## Secondary bending

For some samples with high-level grooves (1.2mA), a rupture of the bulk PLA was observed (Figure 43a-b). However, the maximum tensile stress of the polymer (~21 MPa) was below the expected ultimate tensile strength ($UTS_{T230;v40;h0.2} = \sim 53\ MPa$). It is assumed, that this rupture resulted from a momentum (M) respectively, secondary bending, which was induced by the shifted planes (neutral lines) of the applied forces (F) (Figure 43c). Literature suggests that, contrary to the tensile stress, the bending stress induced by the secondary momentum increases in a nonlinear manner [95]. Secondary bending influenced the yield of all the lap shear samples. Thinner samples would decrease the secondary bending and most likely lead to less distorted results.
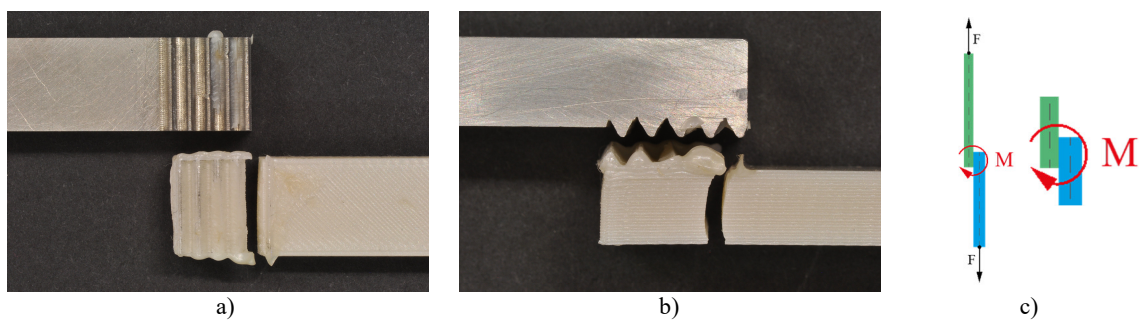


*Figure 43: Secondary bending during lap shear test a)-b) PLA-rupture of 1.2mA sample c) schematic illustration*

## 4.3.3.2. 3-Point bending tests

The 3-point bending tests delivered a better understanding of the delamination behavior and the stresses during the deformation. For each of the two sample types, three different groove heights and reference bulk material samples were tested (Figure 44).
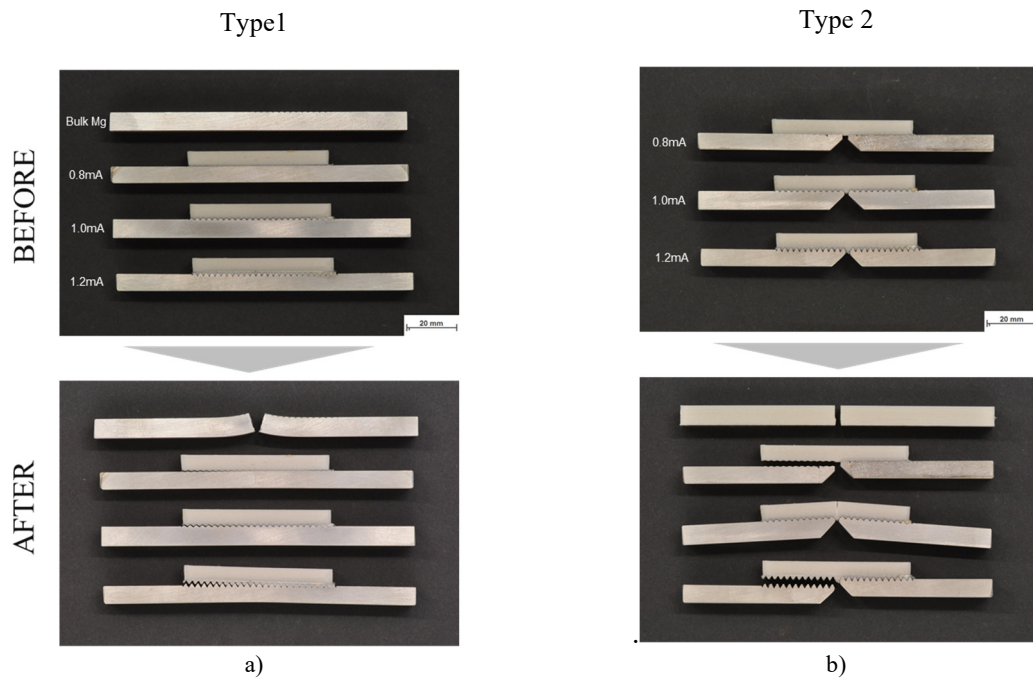


*Figure 44:3-point bending samples before and after the test a) type 1 b) type 2*

For type 1, the joint with the low-level grooves (0.8mA) showed abrupt delamination, while the higher welds presented a significant drop at high stresses followed by stepwise delamination propagation (Figure 45a-b). The results show, the higher the grooves, the higher flexural stress the composite can bear.

The results from the type 2 samples imply a different interpretation (Figure 45c). In the beginning, the composites with the mid-level welds illustrated a similar stress curve compared to the taller grooves, but the PLA started to rupture in the center instead of delaminating (Figure 45d). This might be an anomaly and could be triggered by a material defect in the bulk polymer. It could also be a consequence of the time-displaced sample preparation. The 1.0mA samples were prepared separately from the others and showed a significantly higher degree of oxidation on the surface. Oxidized microtopography might facilitate micro-anchoring and, therefore, the polymer's surface adhesion [56].

51

Type 1                                                    Type 2
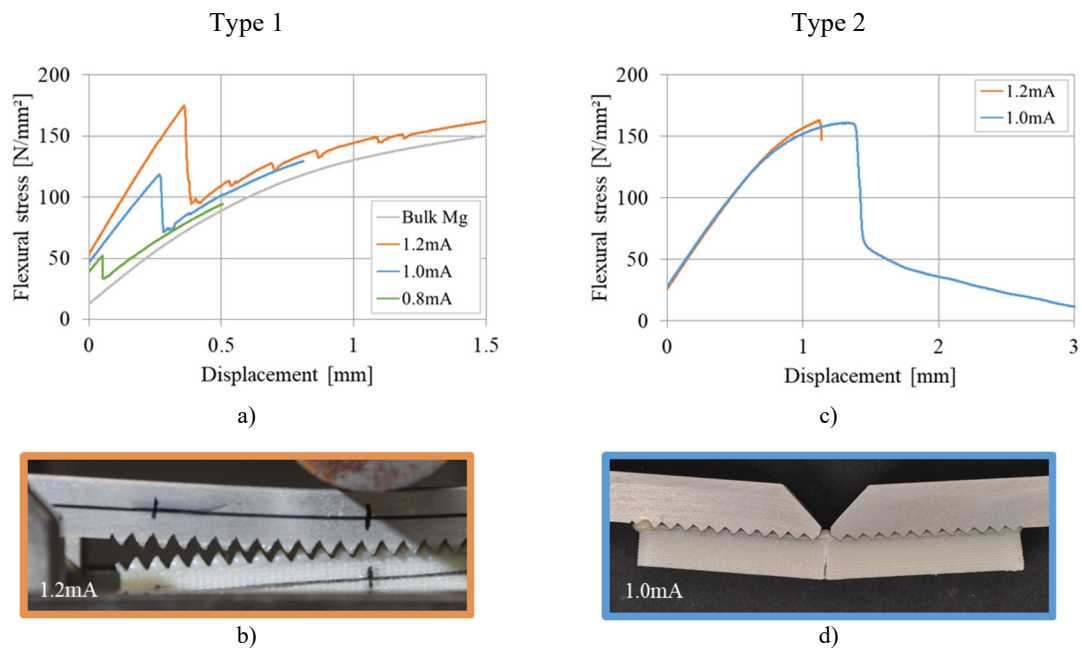


*Figure 45: 3-point bending a) results type 1 b) PLA delamination of 1.2mA sample (type 1) c) results type 2 d) PLA rupture of 1.0mA sample (type 2)*

Interestingly for all the tested samples, the delamination initiated on the same side. This might result from the incremental increase of groove height within one weld pattern caused by the gradual temperature rise of the metal substrate during the EBP (see chapter 4.2).

A fracture surface investigation of the bulk PLA bending displayed *"string-like artifacts"* that spread all over the surface (Figure 46a-b). Literature suggests those artifacts might result from stretched and torn *"amorphous chains of the base monomer"* during the rupture [96]. Only the bending sample showed this phenomenon. In the other fracture surface investigations, the strings might have molten during SEM measurements. Further investigations would be needed.
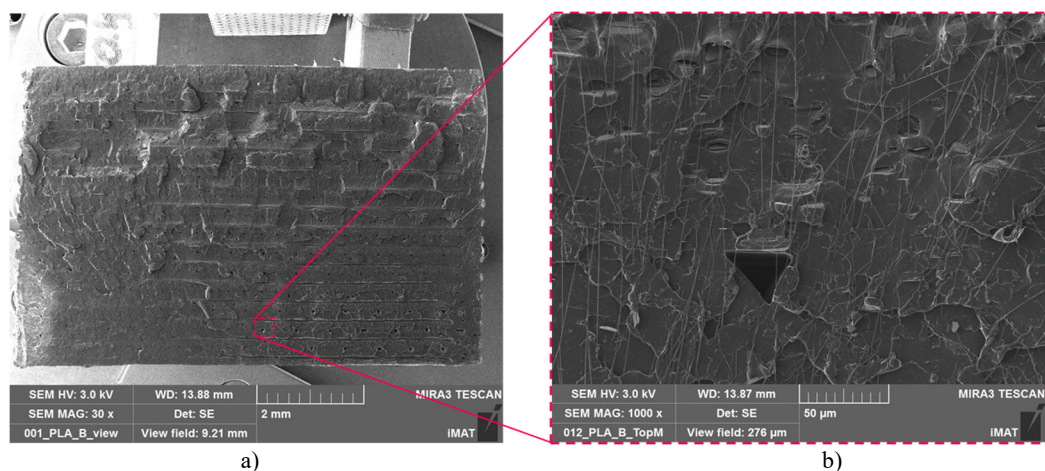


*Figure 46: 3-point bending test of bulk PLA a) PLA fracture surface b) string-like artifacts*

# 4.4. In vitro corrosion tests

The Mg L2+ alloy was tested in three different conditions. Before the actual cast material tests, three test runs with pure magnesium samples were executed to evaluate the system's reliability. During those three runs, the parameters (e.g. $CO_2$ pressure, stirring speed) and the arrangement (e.g. positions and height of the burettes, $CO_2$ diffusor, pH Meter, temperature sensors) were continuously evaluated and optimized. The parameters and arrangements were then maintained for all experiments.

## 4.4.1.  Mg L2+ – as-cast

The in vitro experiments on the as-cast Mg L2+ cuboids (Figure 47a) displayed a slight increase in $H_2$ evolution approximately after day one of immersion (Figure 47b). After the third day, the curve slope gradually decreased until the end of the experiments (7 days). This trend implies a reduced corrosion rate. A long-running corrosion test (>7 days) is recommended to prove this hypothesis. Since the small sample (8x8x2mm) presented significant corrosion (~70% mass loss), it is necessary to prepare bigger samples for longer immersion times (Figure 47c).



a)                                b)                                c)
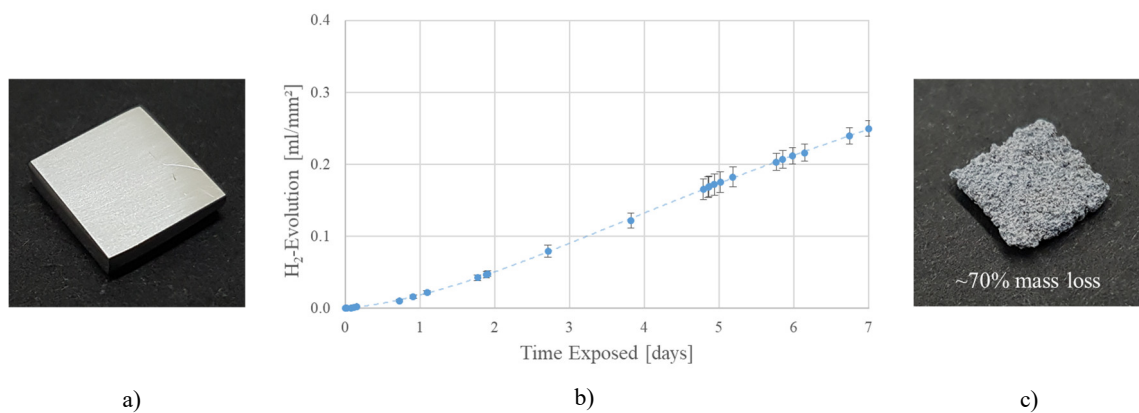
*Figure 47: Mg L2+ (as-cast) a) uncorroded sample b) $H_2$ evolution c) corroded sample after seven days*

## Corrosion products

After seven days, the samples were retrieved from the HBSS and rinsed with ethanol to stop corrosion. Corrosion products covered the whole surface (Figure 48a). XRD findings of Zhang et al. on corroded Mg-6Zn surfaces suggest the presents of magnesium hydroxide [$Mg(OH)_2$] and hydroxyapatite [$Ca_5OH(PO_4)_3$] crystals on the surface [22]. Another study also indicated the precipitation of Mg and Ca containing amorphous phosphates [97]. Figure 48b shows the sample surface after the removal of the corrosion products with chromic acid. The examination of the surface topography showed that severe local and pitted corrosion occurred. The EDX-analysis

(Figure 48c) indicated the presents of the buffering solutions' elements and suggested that hydroxides and hydroxyapatite precipitated at the corroded surface.
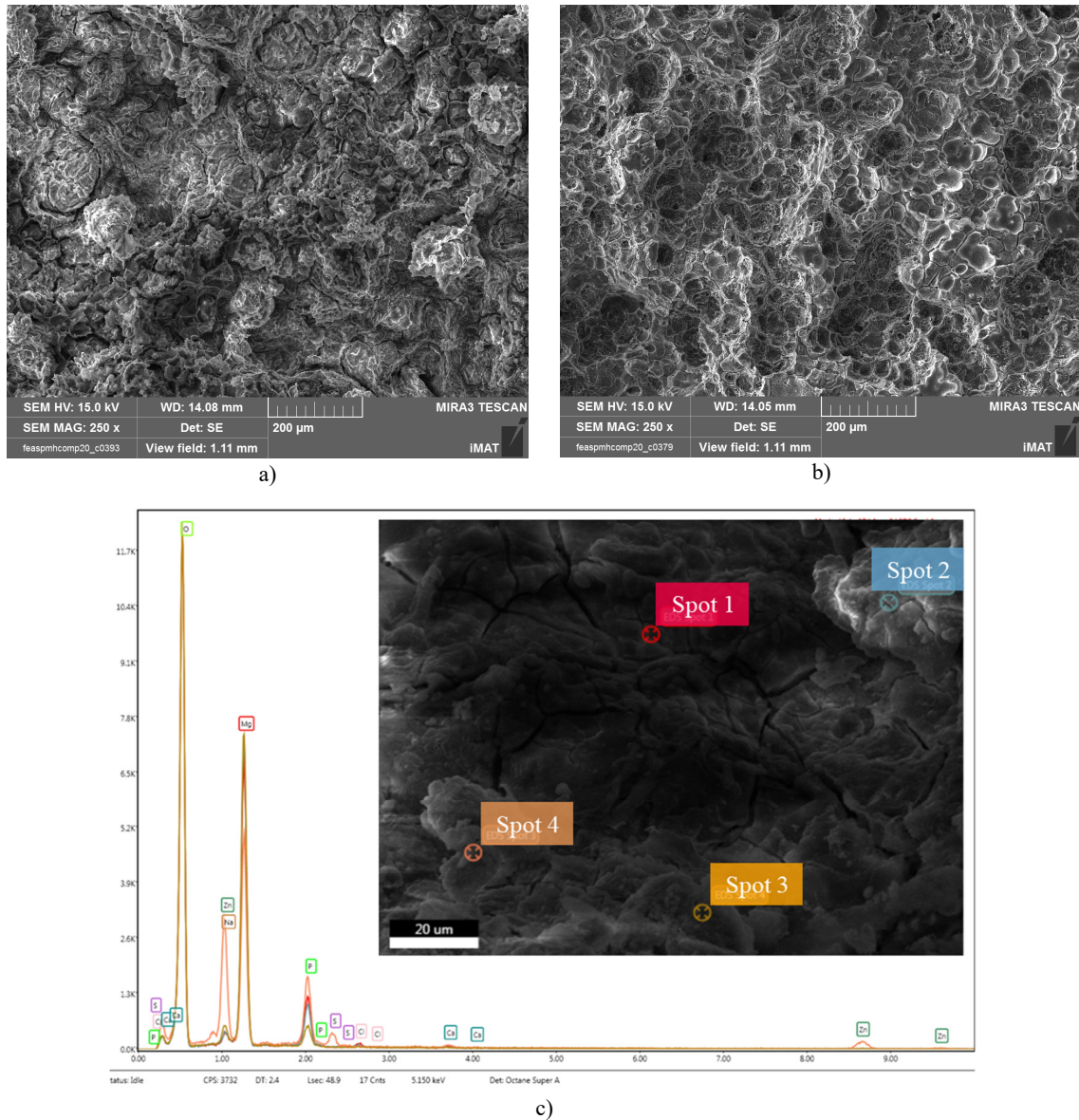


*Figure 48: Corroded Mg L2+ sample a) corrosion products b) sample after cleaning with chromic acid c) EDX-spot measurements and corresponding intensity spectrum*

## Corrosion rates

The corrosion rate calculations from mass loss according to the standard G31-72 illustrated a rate of 22.43 mm/year. This is significantly higher than that of extruded pure Mg rods (~8.02 mm/year) from the previous three test runs. Typically, the addition of alloying elements should inhibit corrosion. However, due to the applied manufacturing techniques, those materials show completely different microstructures, and therefore, the corrosion resistance also differs. Birbilis et al. compared pure Mg (as-cast and extruded) and found that the extruded material exhibits

lower corrosion rates due to the finer grain structure, leading to an increase of the grain boundaries [98]. They concluded that the oxide layers at grain boundaries counteract corrosion. The studies of Ibrahim et al. showed that ageing treatment for Mg-1.2Zn-0.5Ca-alloy causes a reduction of the corrosion rate by approximately 46% ($CR_{cast} = 8.2\ \frac{mm}{year} \rightarrow CR_{ht;2h} = 4.4\ \frac{mm}{year}$) [99].

## 4.4.2. Mg L2+ – EB-structured surface

The heat-treated surface (EB-structured) showed lower corrosion during the first 24h compared to the untreated bulk material. This observation coincides with the findings from the literature [70–72]. Nevertheless, after 24 hours, the bulk material illustrated lower corrosion rates (Figure 49a).

Due to the sample preparation with cold embedding, three possible error sources arose, which influenced the higher absolute values. Firstly, the crevice corrosion in the Mg L2+/embedding interfaces from the start of immersion. Secondly, with ongoing corrosion progress, the embedding started to crack and delaminated progressively, which induced an increasing amount of bulk material exposed to HBSS. Since this cracking and delamination (Figure 49b) went irregularly and varied from sample to sample, this cumulative increase of surface area could not be rationally considered in the calculations. Finally, the cold embedding material might also be an additional gas evolution source to an unknown extent.
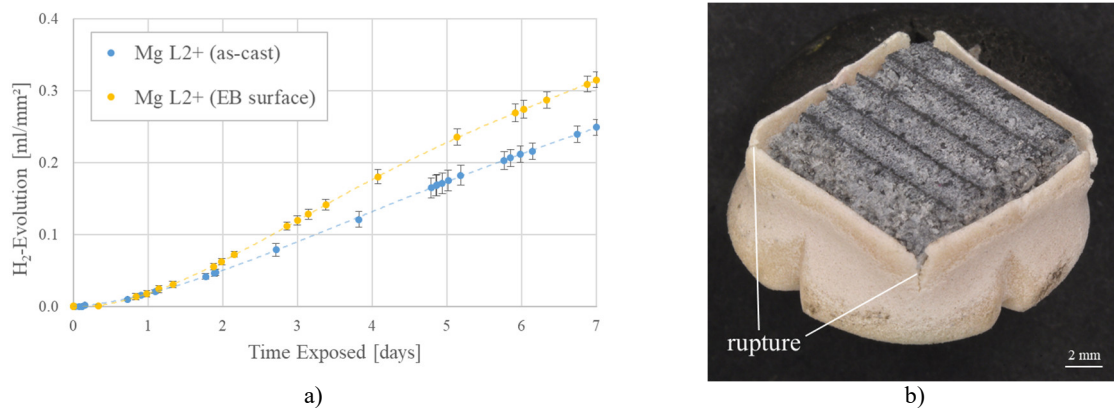


*Figure 49: EB-structured sample a) H₂ evolution - Comparison of as-cast and EB-surface b) ruptured embedding*

The long-term immersion test of seven days with cold embedding did not provide a significant quantitative result. More importantly, a more in-depth qualitative insight into the corrosion behavior in the different weld regions was gained. Figure 50a-c shows the topography of the surface-treated corroded sample from the top, where the corrosion products were removed with chromic acid. The top surface illustrates many areas where local and pitted corrosion (Figure 50c)

took place in the welds' outer regions (groove valleys). In no small part, the groove peaks did not show pitting corrosion.
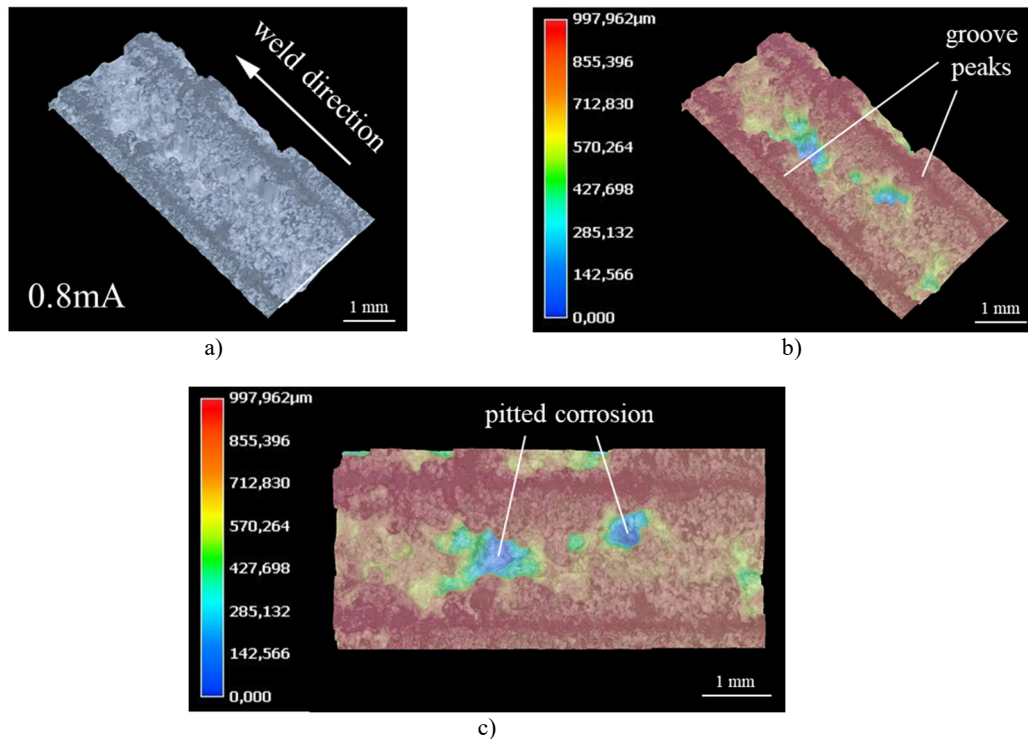


*Figure 50: EB-structured (0.8mA) – Topography of corroded and cleaned sample a) weld direction b) groove peaks c) pitted corrosion (top-view)*

## 4.4.3.  Mg L2+ – add joined with PLA

For the add joined sample, the $H_2$ evolution results (Figure 51a) also did not deliver reasonable quantitative results due to the potential error sources (crevice corrosion, embedding delamination, and gas evolution) mentioned above. Additionally, only the smallest topography, and therefore the weakest hybrid bond, was tested, which detached after approximately three days of immersion. This lead to a significant increase in the total surface area exposed to the electrolyte by a factor of five ($12 \ mm^2 \rightarrow 60 \ mm^2$). The gas evolution from the PLA cubes was neglected because during the hydrolysis of PLA (see chapter 2.4.2), no hydrogen gas is released. Further, the PLA cubes did not show any observable surface degradation.

| a) | b) |
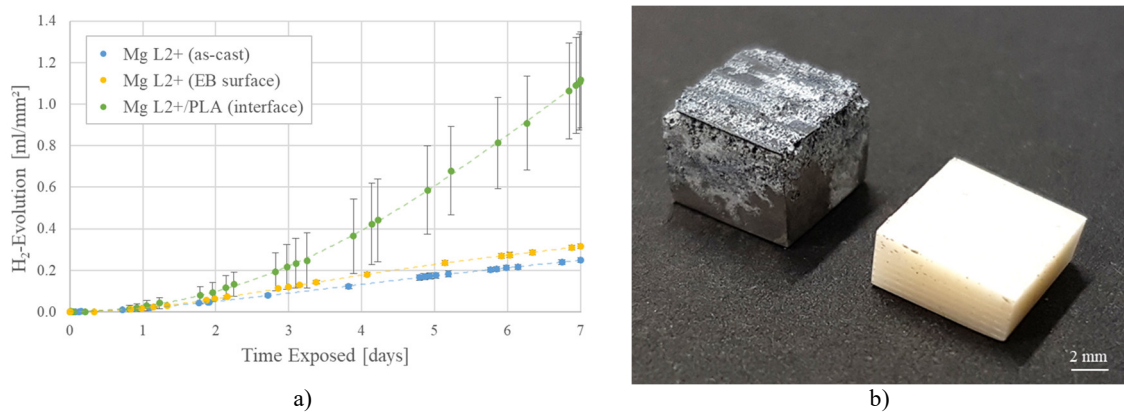
*Figure 51: a) H$_2$ evolution - Comparison of as-cast and EB surface & Mg L2+/PLA interface corrosion b) add joined sample after seven days of immersion*

The corroded samples' qualitative observations gave an interesting insight into the interface corrosion behavior of PLA and Mg L2+. Figure 52a-c illustrates a side view of the detached Mg L2+ substrate. The corrosion products were removed with chromic acid. The topography shows that the finer-grained structure (EB-surface) was corroding at a lower degree. This observation confirmed the properties suggested by the literature [70–72].



| a) | b) | c) |
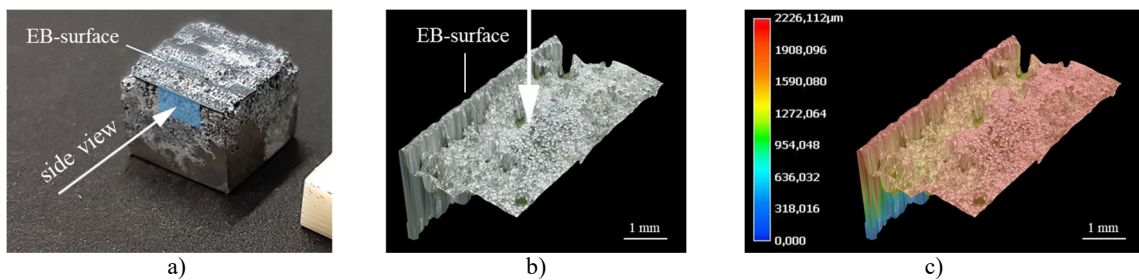
*Figure 52: Interface corrosion Mg/PLA a) corroded sample b)-c) topography (side-view)*

# 5. Summary

The experiments showed that the production of metal-polymer hybrid structures by applying the FDM process is feasible. Groove-shaped topographies with different heights were generated by EBP of the surface to facilitate the bond adhesion. The qualitative investigation of the EB structure showed cracks on the surface due to the fast cooling rates of the process. Based on the results, the EBP might be a suitable technique to modify the surface of Mg L2+.

During the add joining process, elevated working temperatures ($T_n$ and $T_p$) and increased polymer extrusion volume (multiple bottom layer prints) facilitated the polymer's intrusion into the grooves of the modified Mg-alloy. The re-melting of the add joined samples led to more homogenous infilling of the polymer and fewer cavities in the bulk polymer. However, it decreased the bond adhesion significantly.

The printing parameter tests of the standalone PLA have shown that the layer height has a high impact on the UTS. In the given boundary conditions, the statistical model predicted a maximum UTS of ~59.7Mpa ($T_p = 230\,°C$ ; $h_L = 0.08\,mm$ ; $v = 40\,mm/s$).

The Mg L2+/PLA hybrid joints with the highest grooves ($h = 1310.2 \pm 23.8\,\mu m$) showed a ULSS of $12.0 \pm 1.1$ MPa, observing a mixed failure in the fracture area. The groove valleys contained plenty of PLA remnants and on the groove peaks, small PLA residues stayed attached. The single lap shear sample thickness negatively influenced the ULSS due to the high secondary momentum generated during the testing. The 3-point bending tests displayed that the add joined PLA significantly increased the resistance to bending in comparison to the bulk alloy samples.

$H_2$ evolution corrosion experiments were carried out on a $CO_2$-buffered immersion setup. The physiological conditions (pH and temperature) of the immersion electrolyte (HBSS) were kept constant. The setup worked reliable and the results were consistent. The bulk Mg L2+ as-cast showed corrosion rates (CR) of 22.43 mm/year. Pure magnesium extruded was also tested as a reference (CR = 8.02 mm/year). Due to sample preparation errors, the protective effects of the surface-modified Mg-alloy (0.8mA) could not be validated. Further, the add joined sample (0.8mA) detached after three days of immersion.

The results of add joined metal-polymer hybrids presented in this work are promising in the field of biomedical application.

# 6. Outlook

## Mg L2+/PLA hybrids

**Corrosion tests:** The immersion times should be increased to gain a better insight into the alloys' and hybrids' long-term corrosion behavior. Since the EB surface samples' corrosion experiments delivered vague results, "pure" EB-structure tests by the extraction of segments from bigger weld zones should be carried out. Further, it is recommended to conduct investigations on hybrids with higher bond strengths (e.g. 1.2mA).

**Mechanical tests:** The secondary bending, induced by the high sample thickness, is considered critical. Therefore, substrate thicknesses should be decreased. Additionally, an increase in the working temperatures ($T_n$ and $T_p$) might lead to an increase in bond strength.

**Bioresorbable polymer:** Since PLA exhibits long degradation times (~24 months), it is suggested to carry out the experiments with other bioresorbable polymers. The literature review indicates that PLGA might be a good fit because varying PLA and PGA mixing ratios can easily tune its degradation times.

## 3D-printing of zinc alloys

In the last decades, the use of zinc alloy for biomedical purposes drew much attention. Especially the moderate corrosion rates (CR) of Zn-alloys are considered advantageous over Mg-alloys (high CR) and Fe-alloy (low CR). A Zn-1Mg-0.1Ca ternary alloy was found to be a very promising material composition according to its degradation rates and mechanical properties in the literature review.

For the first printing experiments, Zn-1.45Mg alloy was supplied cost-free by *IMR-Metalle* (Austria). The properties of this powder (Figure 53a) were not ideal (e.g. particle morphology, flow properties, particle size distribution), which in further consequence caused some problems during the printing process.

During the first print attempts, a dense particle mist formed in the print chamber. This mist was attributed to the fact that zinc and magnesium exhibit low melting points and high vapor pressures. Consequently, the mist resulted from an abrupt sublimation, followed by a deposition of the metal particles. The particle mist shields the laser beam and therefore, less energy is introduced in the

workpiece. More critical, particles close to the protection lens made the glass foggy and damaged it sustainably. To diminish the problem from extensive mist formation, the gas flow was increased to a maximum and the new filter was used. By these measures, the carried-out parameter test achieved a relative density of up to ~90% (Figure 53b). The filter should also be changed more often than for other metal powders because the formed mist clogs the filter quite fast. For future projects, powder with better properties should be acquired to increase the density of the printed material.
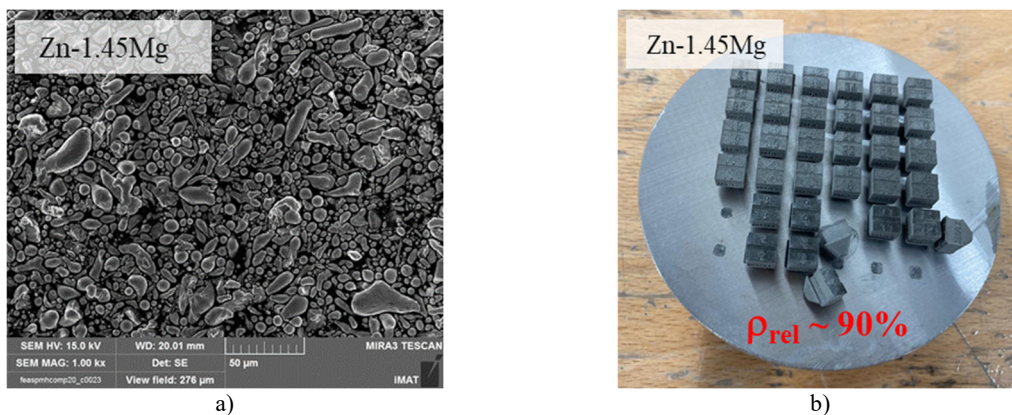


*Figure 53: 3D-printing of Zn-alloy a) powder morphology b) parameter tests*

## Alternative surface structuring patterns for hybrid structures

Besides line-shaped welds, other patterns and parameters were examined briefly. For example, pins were formed via a star-shaped arrangement of the beam paths (Figure 54a-c). The beam path started off-center and traveled outwards at angles of 45° to each other. As a result, this led to the formation of a cave in the center of the pins. One full cycle consisted of eight beam paths. The crater in the center of the figure may contribute to a tighter fit of the metal-polymer interface after the add joining process.
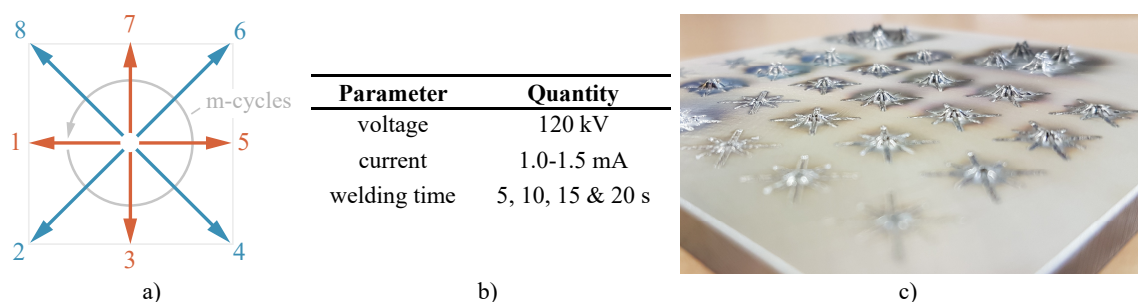


*Figure 54: EBP pins a) star-shaped beam path b) experimental parameters c) parameter tests on Mg L2+*

Another approach would be to prepare a surface with a circular structure that ranges over a wider area. The beam path pattern was similar to the one from the star-shaped parameter study, except that the starting point was in the center without any offset and all path lengths were equal (Figure

55a-b). Additionally, the number of paths per cycle increased stepwise until the pattern appeared perfectly circular (Figure 55c). Circular surface structures were performed to qualitatively evaluate the surfaces, as shown in Figure 55d-f.
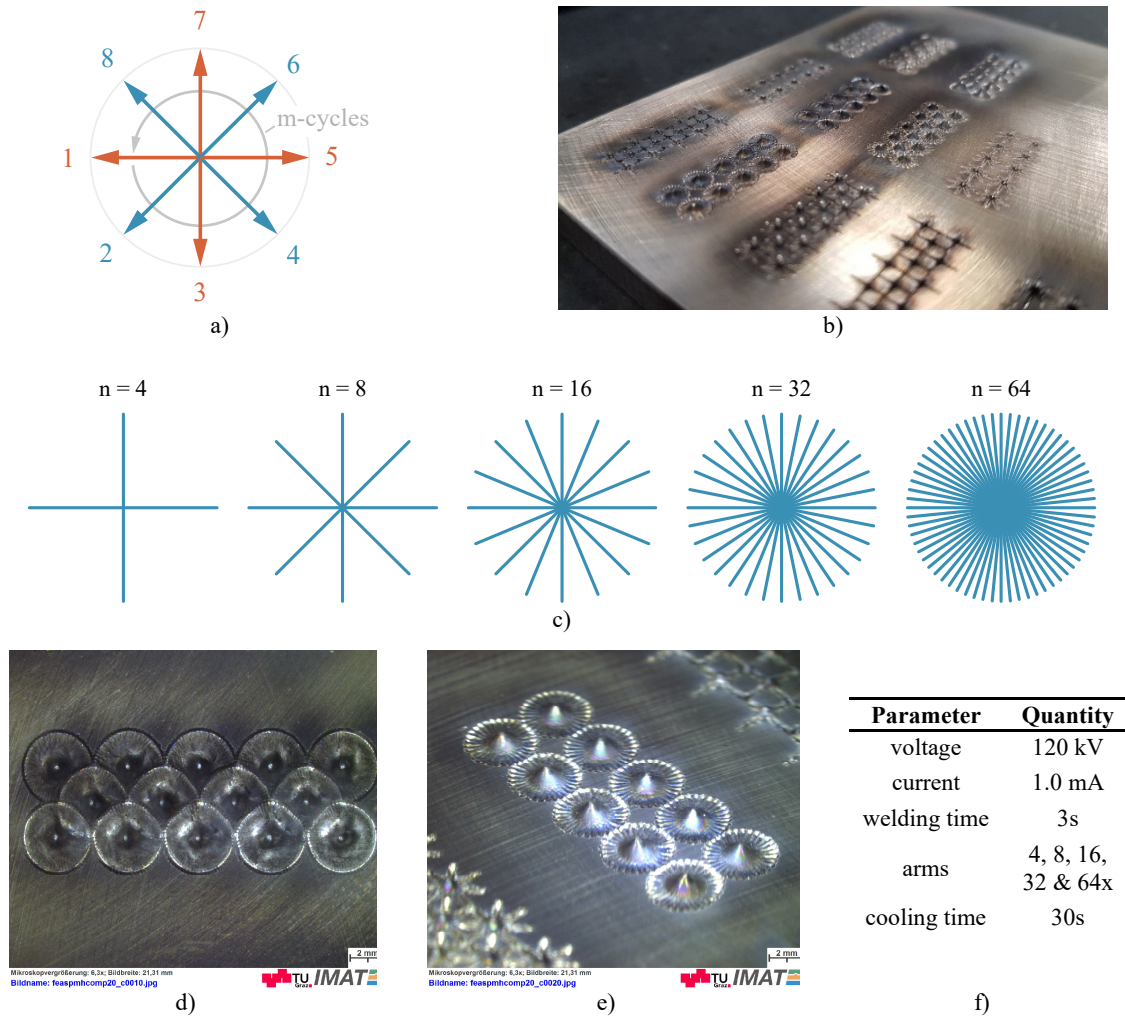


*Figure 55: EBP circular surface structures a) star-shaped beam paths b) parameter tests c) pattern with different amount of arms (n) d) n=64 e) n=32 f) EB parameter*

It is strongly recommended to go further into add joining with pin structured surfaces and different pattern geometries (e.g. triangle, hexagon) for a more comprehensive area-covering.

# References

[1]  B. D. Ratner, "A history of biomaterials," in *Biomaterials Science*: Elsevier, 2013, pp. xli–liii.

[2]  Dorland, *Dorland's Illustrated Medical Dictionary E-Book,* 32nd ed.: Saunders, 2011.

[3]  D. Williams, *The Williams dictionary of biomaterials*. Liverpool: Liverpool University Press, 1999.

[4]  B. D. Ratner, A. S. Hoffman, F. J. Schoen, and J. E. Lemons, "Biomaterials Science: An Evolving, Multidisciplinary Endeavor," in *Biomaterials Science*: Elsevier, 2013, pp. xxv–xxxix.

[5]  M. Saini, Y. Singh, P. Arora, V. Arora, and K. Jain, "Implant biomaterials: A comprehensive review," *World journal of clinical cases*, vol. 3, no. 1, pp. 52–57, 2015, doi: 10.12998/wjcc.v3.i1.52.

[6]  D. Zhao, F. Witte, F. Lu, J. Wang, J. Li, and L. Qin, "Current status on clinical applications of magnesium-based orthopaedic implants: A review from clinical translational perspective," *Biomaterials*, vol. 112, pp. 287–302, 2017, doi: 10.1016/j.biomaterials.2016.10.017.

[7]  M. Treiser, S. Abramson, R. Langer, and J. Kohn, "Degradable and resorbable biomaterials," in *Biomaterials Science*: Elsevier, 2013, 179-.

[8]  H. Hermawan, "Updates on the research and development of absorbable metals for biomedical applications," *Progress in biomaterials*, vol. 7, no. 2, pp. 93–110, 2018, doi: 10.1007/s40204-018-0091-4.

[9]  Y. F. Zheng, X. N. Gu, and F. Witte, "Biodegradable metals," *Materials Science and Engineering: R: Reports*, vol. 77, pp. 1–34, 2014, doi: 10.1016/j.mser.2014.01.001.

[10] H. E. Friedrich and B. L. Mordike, *Magnesium technology: Metallurgy, design data, applications*. Berlin, New York: Springer, 2006.

[11] F. Witte, "The history of biodegradable magnesium implants: a review," *Acta biomaterialia*, vol. 6, no. 5, pp. 1680–1692, 2010, doi: 10.1016/j.actbio.2010.02.028.

[12] R. Radha and D. Sreekanth, "Insight of magnesium alloys and composites for orthopedic implant applications – a review," *Journal of Magnesium and Alloys*, vol. 5, no. 3, pp. 286–312, 2017, doi: 10.1016/j.jma.2017.08.003.

[13] C. K. Seal, K. Vince, and M. A. Hodgson, "Biodegradable surgical implants based on magnesium alloys – A review of current research," *IOP Conf. Ser.: Mater. Sci. Eng.*, vol. 4, p. 12011, 2009, doi: 10.1088/1757-899X/4/1/012011.

[14] F. Witte *et al.,* "In vivo corrosion of four magnesium alloys and the associated bone response," *Biomaterials*, vol. 26, no. 17, pp. 3557–3563, 2005, doi: 10.1016/j.biomaterials.2004.09.049.

[15] F. Witte *et al.,* "Degradable biomaterials based on magnesium corrosion," *Current Opinion in Solid State and Materials Science*, vol. 12, 5-6, pp. 63–72, 2008, doi: 10.1016/j.cossms.2009.04.001.

[16] Y. Zheng, *Magnesium alloys as degradable biomaterials*. [S.l.]: CRC PRESS, 2020.

[17] W. F. Forbes, J. F. Gentleman, and C. J. Maxwell, "Concerning the role of aluminum in causing dementia," *Experimental Gerontology*, vol. 30, no. 1, pp. 23–32, 1995, doi: 10.1016/0531-5565(94)00050-D.

[18] C.-H. Ku, D. P. Pioletti, M. Browne, and P. J. Gregson, "Effect of different Ti–6Al–4V surface treatments on osteoblasts behaviour," *Biomaterials*, vol. 23, no. 6, pp. 1447–1454, 2002, doi: 10.1016/S0142-9612(01)00266-6.

[19] S. El-Rahman, "Neuropathology of aluminum toxicity in rats (glutamate and GABA impairment)," *Pharmacological Research*, vol. 47, no. 3, pp. 189–194, 2003, doi: 10.1016/S1043-6618(02)00336-5.

[20] G. Pagano, M. Guida, F. Tommasi, and R. Oral, "Health effects and toxicity mechanisms of rare earth elements-Knowledge gaps and research prospects," *Ecotoxicology and environmental safety*, vol. 115, pp. 40–48, 2015, doi: 10.1016/j.ecoenv.2015.01.030.

[21] H. Tapiero and K. D. Tew, "Trace elements in human physiology and pathology: zinc and metallothioneins," *Biomedicine & Pharmacotherapy*, vol. 57, no. 9, pp. 399–411, 2003, doi: 10.1016/S0753-3322(03)00081-7.

[22] S. Zhang *et al.,* "Research on an Mg-Zn alloy as a degradable biomaterial," *Acta biomaterialia*, vol. 6, no. 2, pp. 626–640, 2010, doi: 10.1016/j.actbio.2009.06.028.

[23] X. Gu, Y. Zheng, Y. Cheng, S. Zhong, and T. Xi, "In vitro corrosion and biocompatibility of binary magnesium alloys," *Biomaterials*, vol. 30, no. 4, pp. 484–498, 2009, doi: 10.1016/j.biomaterials.2008.10.021.

[24] L. Liu *et al.,* "Degradation Rates of Pure Zinc, Magnesium, and Magnesium Alloys Measured by Volume Loss, Mass Loss, and Hydrogen Evolution," *Applied Sciences*, vol. 8, no. 9, p. 1459, 2018, doi: 10.3390/app8091459.

[25] D. Chen *et al.,* "Biocompatibility of magnesium-zinc alloy in biodegradable orthopedic implants," *International journal of molecular medicine*, vol. 28, no. 3, pp. 343–348, 2011, doi: 10.3892/ijmm.2011.707.

[26] G. He *et al.,* "Addition of Zn to the ternary Mg-Ca-Sr alloys significantly improves their antibacterial property," *Journal of materials chemistry. B*, vol. 3, no. 32, pp. 6676–6689, 2015, doi: 10.1039/C5TB01319D.

[27] Y. He *et al.,* "Biocompatibility of bio-Mg-Zn alloy within bone with heart, liver, kidney and spleen," *Sci. Bull.*, vol. 54, no. 3, pp. 484–491, 2009, doi: 10.1007/s11434-009-0080-z.

[28] W. Yu, Z. Liu, H. He, N. Cheng, and X. Li, "Microstructure and mechanical properties of ZK60–Yb magnesium alloys," *Materials Science and Engineering: A*, vol. 478, 1-2, pp. 101–107, 2008, doi: 10.1016/j.msea.2007.09.027.

[29] M. Yamasaki, N. Hayashi, S. Izumi, and Y. Kawamura, "Corrosion behavior of rapidly solidified Mg–Zn–rare earth element alloys in NaCl solution," *Corrosion Science*, vol. 49, no. 1, pp. 255–262, 2007, doi: 10.1016/j.corsci.2006.05.017.

[30] L. Li *et al.,* "Effects of ytterbium addition and heat treatment on the mechanical properties and biocorrosion behaviors of Mg–Zn–Zr alloy," *Journal of Magnesium and Alloys*, vol. 8, no. 2, pp. 499–509, 2020, doi: 10.1016/j.jma.2019.11.013.

[31] E. Zhang and L. Yang, "Microstructure, mechanical properties and bio-corrosion properties of Mg–Zn–Mn–Ca alloy for biomedical application," *Materials Science and Engineering: A*, vol. 497, 1-2, pp. 111–118, 2008, doi: 10.1016/j.msea.2008.06.019.

[32] Z. Li, X. Gu, S. Lou, and Y. Zheng, "The development of binary Mg-Ca alloys for use as biodegradable materials within bone," *Biomaterials*, vol. 29, no. 10, pp. 1329–1344, 2008, doi: 10.1016/j.biomaterials.2007.12.021.

[33] M. Qian and A. Das, "Grain refinement of magnesium alloys by zirconium: Formation of equiaxed grains," *Scripta Materialia*, vol. 54, no. 5, pp. 881–886, 2006, doi: 10.1016/j.scriptamat.2005.11.002.

[34] B. Wang, F. Wang, Z. Wang, Le Zhou, Z. Liu, and P. Mao, "Microstructure and mechanical properties of Mg-Zn-Ca-Zr alloy fabricated by hot extrusion-shearing process," *Materials Science and Engineering: A*, vol. 795, p. 139937, 2020, doi: 10.1016/j.msea.2020.139937.

[35] A. Hadadzadeh, F. Mokdad, B. S. Amirkhiz, M. A. Wells, B. W. Williams, and D. L. Chen, "Bimodal grain microstructure development during hot compression of a cast-homogenized Mg-Zn-Zr alloy," *Materials Science and Engineering: A*, vol. 724, pp. 421–430, 2018, doi: 10.1016/j.msea.2018.03.112.

[36] T. Homma, C. L. Mendis, K. Hono, and S. Kamado, "Effect of Zr addition on the mechanical properties of as-extruded Mg–Zn–Ca–Zr alloys," *Materials Science and Engineering: A*, vol. 527, no. 9, pp. 2356–2362, 2010, doi: 10.1016/j.msea.2009.12.024.

[37] P. Ding, Y. Liu, X. He, D. Liu, and M. Chen, "In vitro and in vivo biocompatibility of Mg-Zn-Ca alloy operative clip," *Bioactive materials*, vol. 4, pp. 236–244, 2019, doi: 10.1016/j.bioactmat.2019.07.002.

[38] L. Li, W. Jiang, P. Guo, W. Yu, F. Wang, and Z. Pan, "Microstructure Evolution of the Mg-5.8 Zn-0.5 Zr-1.0 Yb Alloy During Homogenization," *Mat. Res.*, vol. 20, no. 4, pp. 1063–1071, 2017, doi: 10.1590/1980-5373-mr-2016-1103.

[39] W. Yu *et al.,* "High-strength wrought magnesium alloy with dense nano-scale spherical precipitate," *CHINESE SCI BULL*, vol. 52, no. 13, pp. 1867–1871, 2007, doi: 10.1007/s11434-007-0250-9.

[40] R. Agarwal, J. J. Lee, H. L. Lukas, and F. Sommer, "Calorimetric measurements and thermodynamic optimization of the Ca - Mg system," *Zeitschrift fuer Metallkunde/Materials Research and Advanced Techniques*, vol. 86, pp. 103–108, 1995.

[41] A. A. Nayeb-Hashemi and J. B. Clark, *Phase diagrams of binary magnesium alloys*. Metals Park, Ohio: ASM International, 1988.

[42] M. I. Sabir, X. Xu, and Li Li, "A review on biodegradable polymeric materials for bone tissue engineering applications," *J Mater Sci*, vol. 44, no. 21, pp. 5713–5724, 2009, doi: 10.1007/s10853-009-3770-7.

[43] N. Shimpi, Ed., *Biodegradable and biocompatible polymer composites: Processing, properties and applications*: Elsevier Science & Technology, 2017.

[44] G. Perale and J. G. Hilborn, Eds., *Bioresorbable polymers for biomedical applications: From fundamentals to translational medicine*. Duxford, UK: Woodhead Publishing is an imprint of Elsevier, 2017.

[45] R. Dwivedi *et al.,* "Polycaprolactone as biomaterial for bone scaffolds: Review of literature," *Journal of oral biology and craniofacial research*, vol. 10, no. 1, pp. 381–388, 2020, doi: 10.1016/j.jobcr.2019.10.003.

[46] B. Joseph, A. George, S. Gopi, N. Kalarikkal, and S. Thomas, "Polymer sutures for simultaneous wound healing and drug delivery - A review," *International journal of pharmaceutics*, vol. 524, 1-2, pp. 454–466, 2017, doi: 10.1016/j.ijpharm.2017.03.041.

[47] B. D. Gogas, V. Farooq, Y. Onuma, and P. W. Serruys, "The ABSORB bioresorbable vascular scaffold: an evolution or revolution in interventional cardiology?," *Hellenic journal of cardiology : HJC = Hellenike kardiologike epitheorese*, vol. 53, no. 4, pp. 301–309, 2012.

[48] J. C. Middleton and A. J. Tipton, "Synthetic biodegradable polymers as orthopedic devices," *Biomaterials*, vol. 21, no. 23, pp. 2335–2346, 2000, doi: 10.1016/S0142-9612(00)00101-0.

[49] S. Li, "Hydrolytic degradation characteristics of aliphatic polyesters derived from lactic and glycolic acids," *J. Biomed. Mater. Res.*, vol. 48, no. 3, pp. 342–353, 1999, doi: 10.1002/(sici)1097-4636(1999)48:3<342::aid-jbm20>3.0.co;2-7.

[50] M. S. Singhvi, S. S. Zinjarde, and D. V. Gokhale, "Polylactic acid: synthesis and biomedical applications," *Journal of applied microbiology*, vol. 127, no. 6, pp. 1612–1626, 2019, doi: 10.1111/jam.14290.

[51] L.-Y. Li *et al.,* "Advances in functionalized polymer coatings on biodegradable magnesium alloys – A review," *Acta biomaterialia*, vol. 79, pp. 23–36, 2018, doi: 10.1016/j.actbio.2018.08.030.

[52] B. Gupta, N. Revagade, and J. Hilborn, "Poly(lactic acid) fiber: An overview," *Progress in Polymer Science*, vol. 32, no. 4, pp. 455–482, 2007, doi: 10.1016/j.progpolymsci.2007.01.005.

[53] T. Iwata and Y. Doi, "Morphology and Enzymatic Degradation of Poly( l -lactic acid) Single Crystals," *Macromolecules*, vol. 31, no. 8, pp. 2461–2467, 1998, doi: 10.1021/ma980008h.

[54] K. Hamad, M. Kaseem, M. Ayyoob, J. Joo, and F. Deri, "Polylactic acid blends: The future of green, light and tough," *Progress in Polymer Science*, vol. 85, pp. 83–127, 2018, doi: 10.1016/j.progpolymsci.2018.07.001.

[55] M. Grujicic, "Injection Overmolding of Polymer–Metal Hybrid Structures," in *Joining of polymer-metal hybrid structures: Principles and applications*, S. T. Amancio Filho and J. F. d. Santos, Eds., Hoboken, NJ: Wiley, 2018, 277-306.

[56] J. Friedrich, *Metal-Polymer Systems: Interface Design and Chemical Bonding*. Newark: John Wiley & Sons, Incorporated, 2017.

[57] X. Li *et al.,* "In vitro degradation kinetics of pure PLA and Mg/PLA composite: Effects of immersion temperature and compression stress," *Acta biomaterialia*, vol. 48, pp. 468–478, 2017, doi: 10.1016/j.actbio.2016.11.001.

[58] C. Zhao, H. Wu, J. Ni, S. Zhang, and X. Zhang, "Development of PLA/Mg composite for orthopedic implant: Tunable degradation and enhanced mineralization," *Composites Science and Technology*, vol. 147, pp. 8–15, 2017, doi: 10.1016/j.compscitech.2017.04.037.

[59] Y. Shi *et al.,* "Enhanced corrosion resistance and cytocompatibility of biodegradable Mg alloys by introduction of Mg(OH)2 particles into poly (L-lactic acid) coating," *Sci Rep*, vol. 7, no. 1, 2017, doi: 10.1038/srep41796.

[60] M. S. Butt *et al.,* "Mg alloy rod reinforced biodegradable poly-lactic acid composite for load bearing bone replacement," *Surface and Coatings Technology*, vol. 309, pp. 471–479, 2017, doi: 10.1016/j.surfcoat.2016.12.005.

[61] D. M. Devine, Ed., *Polymer-Based Additive Manufacturing: Biomedical Applications,* 1st ed. Cham: Springer International Publishing, 2019.

[62] L. Yang *et al., Additive Manufacturing of Metals: The Technology, Materials, Design and Production,* 1st ed. Cham: Springer International Publishing, 2017.

[63] H. Schultz, *Electron beam welding*. Cambridge: Abington Pub, 2004.

[64] D. L. Olson, *Welding, brazing and soldering*. Materials Park, Ohio: ASM International, 1993.

[65] S. Kou, *Welding metallurgy,* 2nd ed. Hoboken, N.J: Wiley-Interscience, 2010.

[66] M. Węglowski, S. Błacha, and A. Phillips, "Electron beam welding – Techniques and trends – Review," *Vacuum*, vol. 130, pp. 72–92, 2016, doi: 10.1016/j.vacuum.2016.05.004.

[67] J. K. Lawrence and L. O. David, *ASM Handbook - Volume 13 - Corrosion*. Ohio: American Society for Metals, 1987.

[68] Y. Lu, A. R. Bradshaw, Y. L. Chiu, and I. P. Jones, "Effects of secondary phase and grain size on the corrosion of biodegradable Mg-Zn-Ca alloys," *Materials science & engineering. C, Materials for biological applications*, vol. 48, pp. 480–486, 2015, doi: 10.1016/j.msec.2014.12.049.

[69] F. Iranshahi, M. B. Nasiri, F. G. Warchomicka, and C. Sommitsch, "Corrosion behavior of electron beam processed AZ91 magnesium alloy," *Journal of Magnesium and Alloys*, vol. 8, no. 4, pp. 1314–1327, 2020, doi: 10.1016/j.jma.2020.08.012.

[70] J. Park *et al.,* "Corrosion behavior of biodegradable Mg-based alloys via femtosecond laser surface melting," *Applied Surface Science*, vol. 448, pp. 424–434, 2018, doi: 10.1016/j.apsusc.2018.04.088.

[71] J. Z. Lu, S. S. Joshi, M. V. Pantawane, Y.-H. Ho, T.-C. Wu, and N. B. Dahotre, "Optimization of biocompatibility in a laser surface treated Mg-AZ31B alloy," *Materials science & engineering. C, Materials for biological applications*, vol. 105, p. 110028, 2019, doi: 10.1016/j.msec.2019.110028.

[72] X. Yao *et al.,* "Surface modification of biomedical Mg-Ca and Mg-Zn-Ca alloys using selective laser melting: Corrosion behaviour, microhardness and biocompatibility," *Journal of Magnesium and Alloys*, 2020, doi: 10.1016/j.jma.2020.08.011.

[73] C.-C. Lin and K. S. Anseth, "The Biodegradation of biodegradable polymeric biomaterials," in *Biomaterials Science*: Elsevier, 2013, pp. 716–728.

[74] D. Henton, P. Gruber, J. Lunt, and J. Randall, "Polylactic Acid Technology," in *Natural Fibers, Biopolymers, and Biocomposites*, A. Mohanty, M. Misra, and L. Drzal, Eds.: CRC PRESS, 2005.

[75] G. J. Tortora and B. Derrickson, *Principles of anatomy and physiology,* 12th ed. Hoboken, N.J.: Wiley, 2009.

[76] J. A. Pryor and A. S. Prasad, *Physiotherapy for Respiratory and Cardiac Problems: Adults and Paediatrics,* 4th ed. London: Elsevier Health Sciences UK, 2014.

[77] Y. Xin, T. Hu, and P. K. Chu, "Influence of Test Solutions on In Vitro Studies of Biomedical Magnesium Alloys," *J. Electrochem. Soc.*, vol. 157, no. 7, C238, 2010, doi: 10.1149/1.3421651.

[78] C. Wang *et al.,* "Electrochemical noise analysis on the pit corrosion susceptibility of biodegradable AZ31 magnesium alloy in four types of simulated body solutions," *Journal of Materials Science & Technology*, vol. 34, no. 10, pp. 1876–1884, 2018, doi: 10.1016/j.jmst.2018.01.015.

[79] N. T. Kirkland, N. Birbilis, and M. P. Staiger, "Assessing the corrosion of biodegradable magnesium implants: a critical review of current methodologies and their limitations," *Acta biomaterialia*, vol. 8, no. 3, pp. 925–936, 2012, doi: 10.1016/j.actbio.2011.11.014.

[80] J. Buha, "Reduced temperature (22–100°C) ageing of an Mg–Zn alloy," *Materials Science and Engineering: A*, vol. 492, 1-2, pp. 11–19, 2008, doi: 10.1016/j.msea.2008.02.038.

[81] K. Holzleiter, "Friction Stir Processing of a Microalloyed Magnesium for Biomedical Application," M.S. thesis, Technical University of Graz, Austria, 2017.

[82] B. Lageder, "Functionalization of the surface of titanium by addition of magnesium," M.S. thesis, Institute of Materials Science, Joining and Forming, Technical University of Graz, Austria, 2017.

[83] B. Dance, I. Guy, E. Kellar, C. James, and et al., "Workpiece Structure Modification Method," EP 1551590 B1.

[84] M. Dobner, *Untersuchungen zum Elektronenstrahlschweissen dickwandiger Bauteile*. Aachen: Shaker, 1997.

[85] *Plastics - Determination of tensile properties - Part 2: Test conditions for moulding and extrusion plastics, EN ISO 527-2*, Vienna.

[86] *Test Method for Apparent Shear Strength of Single-Lap-Joint Adhesively Bonded Metal Specimens by Tension Loading (Metal-to-Metal), ASTM D1002 - 10*, West Conshohocken, PA.

[87] R. L. Powell and W. A. Blanpied, *Thermal Conductivity of Metals and Alloys at Low Temperatures: A Review of Literature,* 556th ed.: National Bureau of Standards, 1954.

[88] *Strukturklebstoffe - Charakterisierung einer Oberfläche durch Messung der Adhäsion nach dem Dreipunkt-Biegeverfahren, DIN EN 1966*, Berlin.

[89] J. Hofstetter *et al.,* "Assessing the degradation performance of ultrahigh-purity magnesium in vitro and in vivo," *Corrosion Science*, vol. 91, pp. 29–36, 2015, doi: 10.1016/j.corsci.2014.09.008.

[90] *Guide for Laboratory Immersion Corrosion Testing of Metals, ASTM G31 - 72*, West Conshohocken, PA.

[91] F.-D. Kopinke, M. Remmler, K. Mackenzie, M. Möder, and O. Wachsen, "Thermal decomposition of biodegradable polyesters—II. Poly(lactic acid)," *Polymer Degradation and Stability*, vol. 53, no. 3, pp. 329–342, 1996, doi: 10.1016/0141-3910(96)00102-4.

[92] E. S. Greenhalgh, *Failure analysis and fractography of polymer composites*. Cambridge: Woodhead, 2009.

[93] R. Falck, J. F. Dos Santos, and S. T. Amancio-Filho, "Microstructure and Mechanical Performance of Additively Manufactured Aluminum 2024-T3/Acrylonitrile Butadiene Styrene Hybrid Joints Using an AddJoining Technique," *Materials (Basel, Switzerland)*, vol. 12, no. 6, 2019, doi: 10.3390/ma12060864.

[94] M. D. Banea, L. F. M. Da Silva, and Campilho, Raul D. S. G., "Principles of Adhesive Bonding," in *Joining of polymer-metal hybrid structures: Principles and applications*, S. T. Amancio Filho and J. F. d. Santos, Eds., Hoboken, NJ: Wiley, 2018, pp. 3–28.

[95] C. E. Chaves, D. J. Inforzato, and F. F. Fernandez, "Principles of Mechanical Fastening in Structural Applications," in *Joining of polymer-metal hybrid structures: Principles and applications*, S. T. Amancio Filho and J. F. d. Santos, Eds., Hoboken, NJ: Wiley, 2018, 147–186.

[96] B. Wittbrodt and J. M. Pearce, "The effects of PLA color on material properties of 3-D printed components," *Additive Manufacturing*, vol. 8, pp. 110–116, 2015, doi: 10.1016/j.addma.2015.09.006.

[97] H. Kuwahara, Y. Al-Abdullat, N. Mazaki, S. Tsutsumi, and T. Aizawa, "Precipitation of Magnesium Apatite on Pure Magnesium Surface during Immersing in Hank's Solution," *Mater. Trans.*, vol. 42, no. 7, pp. 1317–1321, 2001, doi: 10.2320/matertrans.42.1317.

[98] N. Birbilis, K. D. Ralston, S. Virtanen, H. L. Fraser, and C. H. J. Davies, "Grain character influences on corrosion of ECAPed pure magnesium," *Corrosion Engineering, Science and Technology*, vol. 45, no. 3, pp. 224–230, 2010, doi: 10.1179/147842209X12559428167805.

[99] H. Ibrahim, A. D. Klarner, B. Poorganji, D. Dean, A. A. Luo, and M. Elahinia, "Microstructural, mechanical and corrosion characteristics of heat-treated Mg-1.2Zn-0.5Ca (wt%) alloy for use as resorbable bone fixation material," *Journal of the mechanical behavior of biomedical materials*, vol. 69, pp. 203–212, 2017, doi: 10.1016/j.jmbbm.2017.01.005.

# List of figures

# Appendix

## G-Code

Before some g-code examples are shown, a few fundamental g-code expressions will be listed in the following table:

| G-code | Comment |
|--------|---------|
| G0 | Rapid movement |
| G1 | Linear movement |
| G4 | Pause |
| G92 | Set position (X, Y, Z, or E) |

### Setting new z-axis offset

The first adjustment was to reset the z-coordinate to define a new zero position. This was required since each print's starting height varied because of the different topography heights and sample thicknesses.

```
   G-code              Comment
1  G1 F600 Z6.68       ;position on the substrate surface (h=6.68)
2  G92 Z8.25           ;set the new offset of zero at z=8.25
3  G4 P3000            ;PAUSE > give time to overwrite EPROM
4  G1 F300 Z0.2        ;extruder 0.2 above surface
5  G4 P30000           ;PAUSE > check distance of substrate & nozzle
```

Some will ask themself why the second line contains "`G92 Z8.25`" and not "`G92 Z0`". Trials have shown that a "`G92 Z0`"-command followed by e.g. "`G1 Z0.2`"-command led the print head to move to $z = 8.45$. Further investigation and coding did not deliver a reasonable explanation for this arbitrary offset. It might be the case that there is an inherent factory offset of $z = 8.25$ of the *Ultimaker S5*.

### Multiple bottom-layers

The extrusion volume of the 0.2-layer was increased to guarantee a complete infilling of the topography. Depending on the groove height, either one, three, or five bottom layers were printed. The code from the first bottom layer was duplicated and the "filament extrusion"-reset (`G92 E0`) was implemented. The filament had to be withdrawn (`G1 F1500 E-15`), otherwise molten

polymer would have escaped from the nozzle during the movement to the initial position (`G0 F1500 X`$_{start}$ `Y`$_{start}$).

```
   G-code                      Comment
1  ;1st layer
2  [...]
3
4  G92 E0                      ;extruder is set to zero again
5  G1 F1500 E-15               ;filament retraction
6  G1 F600 Z2.2                ;lift printhead
7  G0 F1500 Xstart Ystart      ;move to start position of 1st layer
8  G1 F600 Z0.2                ;move down to start position
9
10 ;2nd bottom layer
11 [...]                       ;copy & paste of 1st layer
```

## Merging of two different 3D models

Since only the interface regions required multiple layer printing, the bulk sample had to be sliced separately. The generated code was then attached after the "multiple bottom layer"-prints. Again, the extruder-reset was necessary.

```
   G-code                      Comment
1  ;n-bottom layers
2  [...]                       ;printing only in the interface region
3
4  G92 E0                      ;extruder is set to zero again
5  G1 F1500 E-15               ;filament retraction
6  G1 F600 Z2.2                ;lift printhead
7
8  ;bulk print
9  [...]                       ;printing bulk sample
```

# Datasheet – BASF PLA

## Technical Data Sheet

### Innofil3D PLA

Filament suitable for all commercially available leading brands 3D FDM/FFF printers

| IDENTIFICATION OF THE MATERIAL | |
|---|---|
| Trade name | Innofil3D PLA |
| Chemical name | Polylactic Acid |
| Chemical family | Thermoplastic Polylactic Acid |
| Use | 3D-Printing |
| Company | Innofil3D BV |

| GUIDELINE FOR PRINT SETTINGS | | Test Method |
|---|---|---|
| Nozzle temperature | 220 ± 10 °C | Innofil3D |
| Bed temperature | Approx. 60 °C | Innofil3D |
| Bed modification | Tape or glue below 60 °C | Innofil3D |
| Active cooling fan | YES | Innofil3D |
| Layer height | 0.08 – 0.2 mm | Innofil3D |
| Shell thickness | 0.4 – 0.8 mm | Innofil3D |
| Print speed | 40 – 80 mm/s | Innofil3D |

| MATERIAL PROPERTIES | | Test Method |
|---|---|---|
| Melt temperature | 145 – 160 °C | ASTM D3418 |
| Glass transition temperature Tg | ~ 60 °C | ASTM D3418 |
| MFR | 6.09 g/10min | T=210°C; m=2.16kg |
| MVR | 6.73 $cm^3$/10min | T=210°C; m=2.16kg |
| Density | 1.2560 g/$cm^3$ | ASTM D1505 |
| Odor | Odorless | / |
| Solubility | Insoluble in water | / |

Innofil³ᴰ make anything!

| MECHANICAL PROPERTIES | | | Test Method | ISO 527 |
|---|---|---|---|---|
| All test specimens were printed using an Ultimaker 2 under the following conditions: printing temperature = 210°C, heated bed temperature = 75°C, print speed = 40 mm/s, number of shells = 2, Infill under 45° | | | | |
| | Printed vertical (Z-axis) | | Printed horizontal (X,Y-axis) | |
| Infill | 50% | 100% | 50% | 100% |
| Tensile strength (MPa) | 14.68 ± 3.29 | 28.84 ± 4.20 | 24.12 ± 0.58 | 38.08 ± 0.89 |
| Force at break (MPa) | 14.45 ± 3.19 | 28.64 ± 4.07 | 23.86 ± 0.63 | 36.28 ± 1.14 |
| Elongation at max force (%) | 0.85 ± 0.32 | 1.10 ± 0.23 | 2.16 ± 0,07 | 2.10 ± 0,00 |
| Elongation at break (%) | 0.85 ± 0.32 | 1.10 ± 0.23 | 2.40 ± 0.12 | 2.84 ± 0.19 |
| Relative tensile strength (MPa/g) | 1.59 ± 0,40 | 2.35 ± 0,36 | 2.72 ± 0,06 | 3.25 ± 0,08 |
| Emodulus (MPa) | 2027 ± 44 | 3150 ± 54 | 1760 ± 38 | 2852 ± 88 |

**STRESS – STRAIN CURVES**

| Vertical 100% | Horizontal 100% |
|---|---|

Innofil³ᴰ *make anything!*
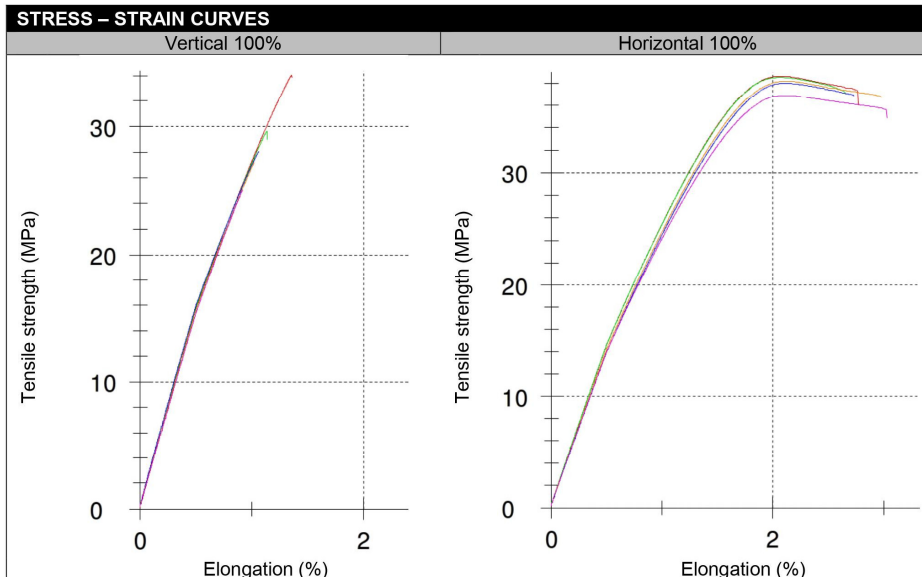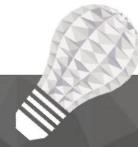
| FILAMENT SPECIFICATIONS | | Test Method |
|---|---|---|
| Diameter 1.75 | 1.75 ± 0.05 mm | Innofil3D |
| Diameter 2.85 | 2.85 ± 0.05 mm | Innofil3D |
| Diameter 3.00 | 3.00 ± 0.05 mm | Innofil3D |
| Max. roundness deviation 1.75 | 0.05 mm | Innofil3D |
| Max. roundness deviation 2.85 | 0.10 mm | Innofil3D |
| Max. roundness deviation 3.00 | 0.10 mm | Innofil3D |
| Net weight on reel | 750 g ± 2% | Innofil3D |

**LIST OF COLORS AND CERTIFICATIONS**[*]

| Colour | Code | RAL nr. | Certifications/approvals | | | | |
|---|---|---|---|---|---|---|---|
| | | | 10/2011[1] | FDA[2] | BfR[3] | 2011/65[4] | EN 71-3[5] |
| Naturel | 0001 | N/A | Yes | Yes | Yes | Yes | Yes |
| Black | 0002 | 9005 | Yes | Yes | Yes | Yes | Yes |
| White | 0003 | 9010 | Yes | Yes | Yes | Yes | Yes |
| Red | 0004 | 3020 | Yes | No | Yes | Yes | Yes |
| Blue | 0005 | 5002 | Yes | Yes | Yes | Yes | Yes |
| Yellow | 0006 | 1003 | Yes | Yes | Yes | Yes | Yes |
| Green | 0007 | 6018 | Yes | Yes | Yes | Yes | Yes |
| Orange | 0009 | 2008 | Yes | No | Yes | Yes | Yes |
| Pearl White | 0011 | 1013 | Yes | Yes | Yes | Yes | Yes |
| Chocolate Brown | 0013 | 8017 | Yes | Yes | Yes | Yes | Yes |
| Gold | 0014 | 1036 | Yes | Yes | Yes | Yes | Yes |
| Light Blue | 0015 | 5012 | Yes | Yes | Yes | Yes | Yes |
| Violet | 0016 | 4008 | Yes | Yes | Yes | Yes | Yes |
| Pink | 0020 | N/A | Yes | No | No | Yes | Yes |
| Silver | 0021 | 9006 | Yes | Yes | Yes | Yes | Yes |
| Magenta | 0022 | 4010 | Yes | No | Yes | Yes | Yes |
| Grey | 0023 | 7045 | Yes | No | Yes | Yes | Yes |
| Bronze | 0032 | 8008 | Yes | Yes | Yes | Yes | Yes |
| Sky Blue | 0035 | N/A | Yes | Yes | Yes | Yes | Yes |
| Orange Translucent | 0010 | 1028[**] | Yes | Yes | Yes | Yes | Yes |
| Blue Translucent | 0024 | 5022[**] | Yes | Yes | Yes | Yes | Yes |
| Dark Green Translucent | 0025 | 6005[**] | Yes | Yes | Yes | Yes | Yes |
| Ice Blue Translucent | 0026 | 5024[**] | Yes | Yes | Yes | Yes | Yes |
| Ocean Blue Translucent | 0027 | 5001[**] | Yes | Yes | Yes | Yes | Yes |

[*] This overview is generated using information obtained from the raw material suppliers.
[**] RAL number used to manufacture the transparent colour.

| Certifications/approvals | Description |
|---|---|
| [1] Regulation EU No 10/2011: | Union Guidelines on Regulation (EU) No 10/2011 on plastic materials and articles intended to come into contact with food (Europe) |
| [2] FDA: | Food and Drug administration approval (U.S.A.) |
| [3] BfR-empfehlung: | No migration of substances with a health risk occurs from the contact materials to the foods (Germany) |
| [4] Directive 2011/65/EU: | The restriction of the use of certain hazardous substances in electrical and electronic equipment (Europe) |
| [5] Directive 2009/48/EC; EN 71-3: | Safety of toys – Part 3: Migration of certain elements (Europe) |

# EDAX report – Mg L2+ (as-cast)

**EDAX TEAM**

| Maxim |
|---|

| Author: | administrator |
|---|---|
| Creation: | 11/20/2020 11:40:06 AM |
| Sample Name: | ACast_SampleD |

### eZAF Smart Quant Results with Carbon Coat

| Element | Weight % | Atomic % | Net Int. |
|---|---|---|---|
| EDS Spectrum: Maxim | ACast_SampleD | Added Spectra | Name_2 | | | |
| MgK | 92.02 | 97.3 | 11099.83 |
| ZrL | 0.18 | 0.05 | 5.06 |
| CaK | 0.43 | 0.28 | 32.59 |
| YbL | 2.14 | 0.32 | 47.63 |
| ZnK | 5.22 | 2.05 | 187.57 |
| EDS Spectrum: Maxim | ACast_SampleD | Added Spectra | Name_3 | | | |
| MgK | 91.56 | 97.12 | 10754.67 |
| ZrL | 0.18 | 0.05 | 4.84 |
| CaK | 0.45 | 0.29 | 33.86 |
| YbL | 2.22 | 0.33 | 49 |
| ZnK | 5.59 | 2.2 | 198.16 |

**Spectrum Overlay**

| kV: 25 | Mag: 270 | Takeoff: 35 | Live Time(s): 483 | Amp | 0.96 | Resolution:(eV) | 130.6 |
|---|---|---|---|---|---|---|---|



Status: Idle   CPS: 3507998  DT: 0.0   Lsec: 483.0   1.370K Cnts   1.900 keV   Det: Octane Super A

# EDAX report – Mg L2+ (intermetallic phases)

**Maxim_Mthesis**

| | |
|---|---|
| Author: | administrator |
| Creation: | 12/11/2019 2:14:37 PM |
| Sample Name: | As -cast_L2plus |

**Area 1**
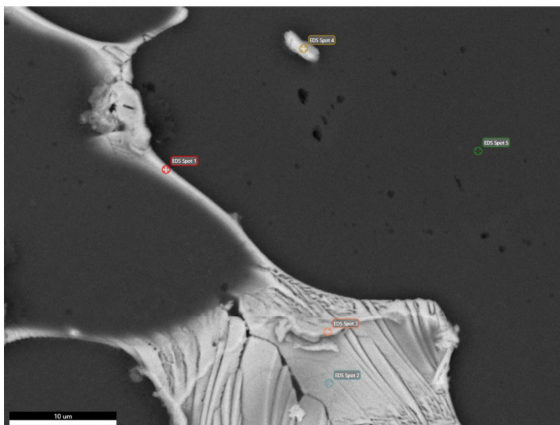


**Spectrum Overlay**

| kV: 15 | Mag: 4894 | Takeoff: 22.2 | Live Time(s): 45.8 | Amp | 7.68 | Resolution:(eV) | 129.6 |
|---|---|---|---|---|---|---|---|



Maxim_Mthesis | As -cast_L2plus | Area 1 | EDS Spot 1
Maxim_Mthesis | As -cast_L2plus | Area 1 | EDS Spot 2
Maxim_Mthesis | As -cast_L2plus | Area 1 | EDS Spot 3
Maxim_Mthesis | As -cast_L2plus | Area 1 | EDS Spot 4
Maxim_Mthesis | As -cast_L2plus | Area 1 | EDS Spot 5

Status: Idle          CPS: 99750          DT: 24.8          Lsec: 45.8          0 Cnts          0.000 keV          Det: Octane Plus
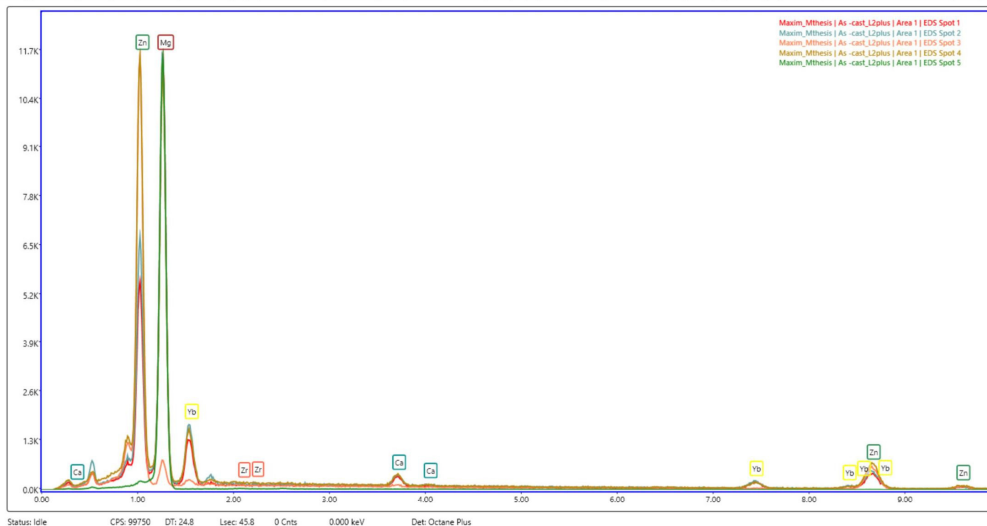
**EDAX APEX**

### eZAF Smart Quant Results

| Element | Weight % | Atomic % | Net Int. |
|---|---|---|---|
| Maxim_Mthesis \| As -cast_L2plus \| Area 1 \| EDS Spot 1 | | | |
| MgK | 52.69 | 78.64 | 2007.83 |
| ZrL | 0.11 | 0.04 | 1.77 |
| CaK | 2.07 | 1.88 | 65.45 |
| YbL | 16.22 | 3.4 | 61.06 |
| ZnK | 28.91 | 16.05 | 136.9 |
| Maxim_Mthesis \| As -cast_L2plus \| Area 1 \| EDS Spot 2 | | | |
| MgK | 51.15 | 77.25 | 1362.21 |
| ZrL | 0.13 | 0.05 | 1.61 |
| CaK | 2.12 | 1.95 | 48.99 |
| YbL | 15.5 | 3.29 | 42.62 |
| ZnK | 31.09 | 17.46 | 107.34 |
| Maxim_Mthesis \| As -cast_L2plus \| Area 1 \| EDS Spot 3 | | | |
| MgK | 15.02 | 32.46 | 219.22 |
| ZrL | 0.42 | 0.24 | 5.99 |
| CaK | 0.86 | 1.13 | 23.47 |
| YbL | 2.22 | 0.67 | 7.28 |
| ZnK | 81.48 | 65.49 | 325.11 |
| Maxim_Mthesis \| As -cast_L2plus \| Area 1 \| EDS Spot 4 | | | |
| MgK | 48.11 | 73.65 | 1691.05 |
| ZrL | 0.36 | 0.15 | 6.71 |
| CaK | 1.84 | 1.71 | 64.71 |
| YbL | 10.74 | 2.31 | 44.74 |
| ZnK | 38.96 | 22.18 | 202.7 |
| Maxim_Mthesis \| As -cast_L2plus \| Area 1 \| EDS Spot 5 | | | |
| MgK | 97.85 | 99.36 | 6322.49 |
| ZrL | 0.71 | 0.19 | 10 |
| CaK | 0.13 | 0.08 | 3.06 |
| YbL | 0.52 | 0.07 | 1.42 |
| ZnK | 0.79 | 0.3 | 3.1 |

# EDAX report – corrosion products on Mg L2+

**Maxim**

| | |
|---|---|
| Author: | administrator |
| Creation: | 8/31/2020 9:32:17 AM |
| Sample Name: | Inter17 |

### Area 2
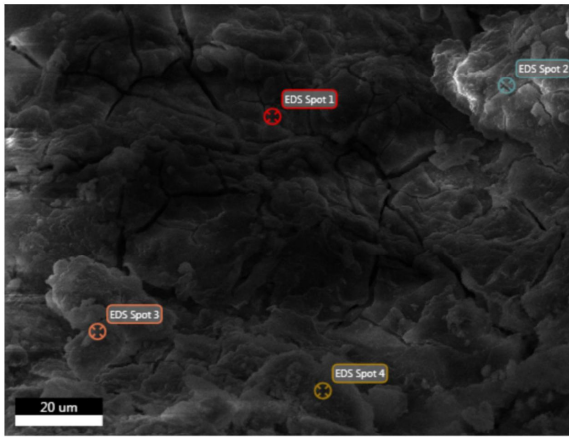


**Spectrum Overlay**

| kV: 15 | Mag: 1958 | Takeoff: 34.9 | Live Time(s): 48.9 | Amp 1.92 | Resolution:(eV) 127.3 |
|---|---|---|---|---|---|
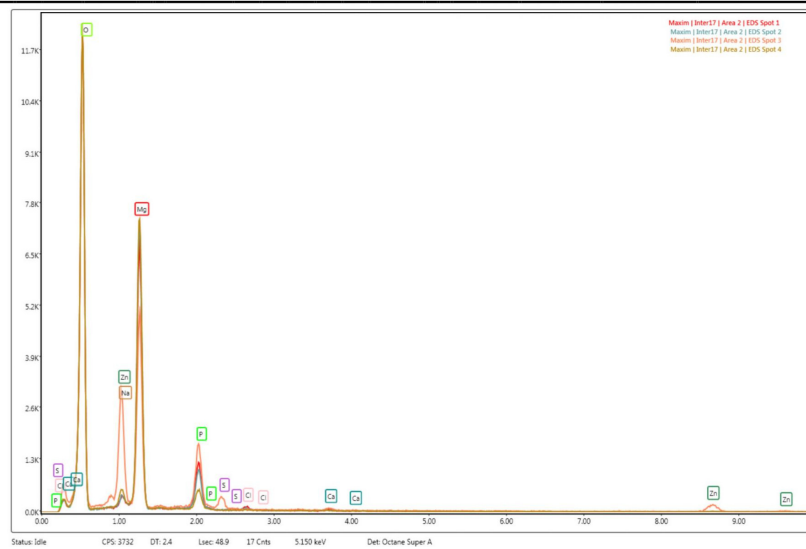
## eZAF Smart Quant Results

| Element | Weight % | Atomic % | Net Int. |
|---------|----------|----------|----------|
| Maxim \| Inter17 \| Area 2 \| EDS Spot 1 | | | |
| O K | 57.84 | 69.02 | 1682.26 |
| NaK | 0.44 | 0.37 | 9.9 |
| MgK | 31.31 | 24.59 | 1085.79 |
| P K | 8.31 | 5.12 | 233.57 |
| S K | 0.07 | 0.04 | 1.85 |
| ClK | 0.72 | 0.39 | 18.41 |
| CaK | 0.5 | 0.24 | 8.98 |
| ZnK | 0.82 | 0.24 | 2.75 |
| Maxim \| Inter17 \| Area 2 \| EDS Spot 2 | | | |
| O K | 57.18 | 68.28 | 1504.65 |
| NaK | 0.51 | 0.43 | 10.22 |
| MgK | 33.38 | 26.23 | 1023.79 |
| P K | 7.02 | 4.33 | 172.46 |
| S K | 0.06 | 0.03 | 1.45 |
| ClK | 0.38 | 0.2 | 8.53 |
| CaK | 0.33 | 0.16 | 5.29 |
| ZnK | 1.15 | 0.34 | 3.37 |
| Maxim \| Inter17 \| Area 2 \| EDS Spot 3 | | | |
| O K | 50.83 | 67.2 | 1532.37 |
| NaK | 1.6 | 1.47 | 37.48 |
| MgK | 21.92 | 19.07 | 710.9 |
| P K | 9.15 | 6.25 | 291.18 |
| S K | 1.56 | 1.03 | 49.84 |
| ClK | 0.08 | 0.05 | 2.44 |
| CaK | 0.62 | 0.33 | 12.99 |
| ZnK | 14.25 | 4.61 | 48.12 |
| Maxim \| Inter17 \| Area 2 \| EDS Spot 4 | | | |
| O K | 57.58 | 68.34 | 1807.91 |
| NaK | 0.11 | 0.09 | 2.57 |
| MgK | 36.33 | 28.37 | 1285.42 |
| P K | 4.07 | 2.5 | 113.54 |
| S K | 0.13 | 0.08 | 3.8 |
| ClK | 0.18 | 0.1 | 4.77 |
| CaK | 0.34 | 0.16 | 6.36 |
| ZnK | 1.25 | 0.36 | 4.24 |